Topics in Current Chemistry (2022) 380:40
https://doi.org/10.1007/s41061-022-00390-w

REVIEW

Plasmonic Hybrid Nanostructures in Photocatalysis: Structures, Mechanisms, and Applications

Rajeshreddy Ninakanti[1,2] · Fons Dingenen[1,2] · Rituraj Borah[1,2] · Hannelore Peeters[1,2] · Sammy W. Verbruggen[1,2]

Received: 17 January 2022 / Accepted: 27 May 2022 / Published online: 11 August 2022
© The Author(s), under exclusive licence to Springer Nature Switzerland AG 2022

Abstract

(Sun)Light is an abundantly available sustainable source of energy that has been used in catalyzing chemical reactions for several decades now. In particular, studies related to the interaction of light with plasmonic nanostructures have been receiving increased attention. These structures display the unique property of localized surface plasmon resonance, which converts light of a specific wavelength range into hot charge carriers, along with strong local electromagnetic fields, and/or heat, which may all enhance the reaction efficiency in their own way. These unique properties of plasmonic nanoparticles can be conveniently tuned by varying the metal type, size, shape, and dielectric environment, thus prompting a research focus on rationally designed plasmonic hybrid nanostructures. In this review, the term "hybrid" implies nanomaterials that consist of multiple plasmonic or non-plasmonic materials, forming complex configurations in the geometry and/or at the atomic level. We discuss the synthetic techniques and evolution of such hybrid plasmonic nanostructures giving rise to a wide variety of material and geometric configurations. Bimetallic alloys, which result in a new set of opto-physical parameters, are compared with core–shell configurations. For the latter, the use of metal, semiconductor, and polymer shells is reviewed. Also, more complex structures such as Janus and antenna reactor composites are discussed. This review further summarizes the studies exploiting plasmonic hybrids to elucidate the plasmonic-photocatalytic mechanism. Finally, we review the implementation of these plasmonic hybrids in different photocatalytic application domains such as H_2 generation, CO_2 reduction, water purification, air purification, and disinfection.

Rajeshreddy Ninakanti and Fons Dingenen contributed equally to this work.

This article is part of the Topical Collection "Solar-driven catalysis"; edited by Nicolas Keller, Fernando Fresno, Agnieszka Ruppert and Patricia Garcia-Munoz.

Extended author information available on the last page of the article

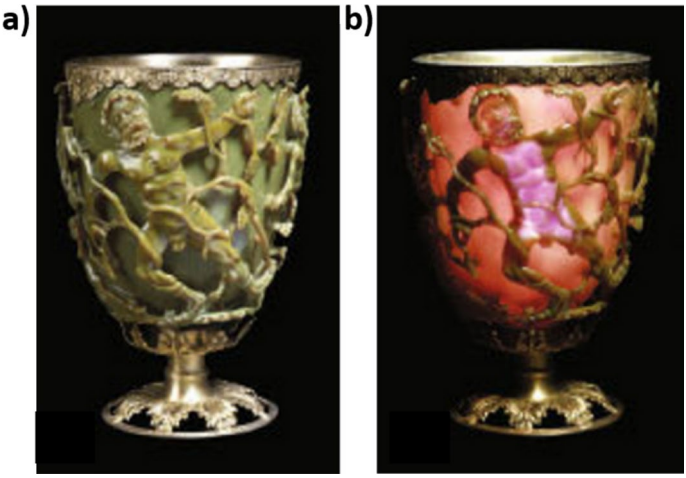

Fig. 1 Lycurgus Cup from the British Museum **a** without and **b** under illumination. Adapted with permission from [3]. CC BY-NC 2.0

Keywords Surface plasmon resonance · Hybrid nanostructures · Photocatalysis · Core–shell · Alloy · Hydrogen · CO_2 reduction · Air purification · Water purification · Antibacterial

1 Introduction

For many hundreds of years, people have been coloring glass [1, 2] and other objects (e.g. the Lycurgus Cup from the fourth century AD (Fig. 1) [3]) with specific metal nanoparticles (NPs), yielding beautiful, bright colors upon illumination. It was not until the twentieth century, however, that scientists elucidated the origin of these colors, attributing the effect to the (localized) surface plasmon resonance [(L)SPR)] of plasmonic NPs [4]. Incident light with a frequency matching the natural frequency of the oscillating conduction band (CB) electrons of a metal NP is strongly absorbed by these NPs. The CB electrons oscillate against the restoring force of the positive nuclei [5]. Because of this unique optical characteristic, plasmonic NPs such as Au, Ag, and Cu have gained enormous interest over the past few decades. Due to their strong interaction with ultraviolet (UV), visible (Vis), and even near-infrared (NIR) light, plasmonic nanoparticles are seen as promising light-harvesting and light-intensification structures in many important light-driven processes such as photovoltaics [6], biosensing [7], surface-enhanced Raman spectroscopy (SERS) [8], and photocatalysis [5, 9]. In view of the growing concerns over climate change, solar light-mediated photocatalysis stands out as a crucial research area for sustainable H_2 generation, CO_2 conversion, and air and water pollutant degradation. In 2019 alone, more than 43 billion tonnes of CO_2 were emitted [10]. Furthermore, it is believed that deep decarbonization (> 80%) is impossible without the wide use of H_2 as fuel [11]. Yet, the large-scale application of photocatalysis, even with widely investigated materials such as TiO_2, is still hindered

by the fact that only a small portion of the solar spectrum is sufficiently energetic to drive the photocatalytic reactions using these pristine materials. Thus, the fairly large band gaps of most semiconductors (SCs) only allow UV light for photoexcitation (< 5% of sunlight), while the remaining energy of the solar spectrum remains unused [4]. In this regard, plasmonic NPs provide a viable solution for more efficient utilization of the solar spectrum. The energetic coupling of their oscillating free electrons to the broad spectral incident light results in strong enhancements in several photocatalytic processes [5].

Over the years, the field of plasmonics has been growing in different directions for improving the light–matter interaction, application-targeted functionality, chemical stability, and so on. One such progressively developing field is that of hybrid plasmonic nanostructures, in which different materials with different functionalities are combined in one hybrid composite. The activity, selectivity, and stability of photo-induced processes may thus be improved by the appropriate design of such nanostructures. In this review, the term "hybrid" implies nanomaterials that consist of multiple plasmonic or non-plasmonic materials, forming complex configurations in the geometry and/or at the atomic level. These can be broadly classified into three main categories, each with its specific structural properties. The first category deals with alloys, where the constituent elements are distributed homogeneously over the nanostructure, leading to a new set of characteristics. The combination of a plasmonic with either another plasmonic or a non-plasmonic metal (with other functionalities) will be discussed in this regard. The second category includes the configurations where a plasmonic core is covered by a shell consisting of another metal, a semiconductor, or a polymer. The third category includes a variety of other structural configurations, such as Janus particles, metal organic frameworks (MOFs), and hybrid two-dimensional (2D) arrays. In contrast to other existing reviews based on the synthesis of a certain class of bimetallic NPs [12, 13] or on the use of single or purely metallic plasmonic NPs for a certain application [5, 9, 14–16], this review covers the synthesis and consequent properties of plasmonic hybrids and their impact on several photocatalytic applications.

In the next sections the synthesis and subsequent properties of multi-metallic alloys, metal@metal, metal@SC, and metal@polymer core–shell configurations, Janus, and other hybrid nanostructures will be discussed. This is followed by an analysis of the use of these materials to enhance photocatalytic activity. Special attention is given here to how plasmonic hybrids are exploited to rigorously study the plasmonic-photocatalytic operation mechanism. Finally, various recent innovative structures are compared towards a selection of important photocatalytic applications, including H_2 production, CO_2 conversion, pollutant degradation, and disinfection.

2 Synthesis and Structural Properties

The abovementioned three main categories of plasmonic hybrid nanostructures will be treated in the following sections. Along with the synthetic techniques to obtain these different configurations, the distinct electronic and optical properties are discussed.

2.1 Alloy

By alloying, new desired intrinsic optical properties or catalytic activity can be obtained, depending on the composition of the alloy. For instance, a second metal can be incorporated into a metal catalyst to control the surface composition, geometry of adsorption sites, selectivity, stability, and electronic properties for catalysis, giving rise to a so-called ensemble effect [17]. Additionally, the incorporation of a plasmonic metal yields a plasmonic effect, with a view to improving photocatalytic reactions. Mixing of two or more plasmonic metals can be useful for tuning the plasmonic response itself, as well as improving the stability of the particles. Advanced synthesis techniques allow for the synthesis not only of mixed bimetallic and multimetallic alloy NPs, but also of ordered alloys with different structuring of crystal facets [18–20].

As one of the best-known examples, the strongly plasmonic Ag is often alloyed with the more stable Au to prevent the oxidation of Ag [21, 22]. The simplest way to synthesize such alloy NPs is by colloidal wet chemical methods. This can be achieved by co-reduction of metal ions in solution, seed-mediated growth or galvanic replacement. Co-reduction relies on two metals having similar reduction potentials and/or similar physical characteristics, which is necessary to form a homogeneous alloy. An example is the modified Turkevich method to synthesize AuAg alloy NPs [23]. There are several similarities between Au and Ag, e.g. a face-centered cubic (fcc) crystal structure, similar lattice parameters (4.065 and 4.079 Å, respectively [24]), and surface energies [25]. However, the different reduction potentials still tend to lead to the formation of a rather "core–shell type alloyed structure" with gold-rich cores and silver-rich shells. This was revealed in one of our previous studies, using 3D energy-dispersive X-ray (EDX) tomography at several stages throughout the synthesis procedure [23]. To obtain a more homogeneous alloy, the use of appropriate molar ratios, reducing agents, and ligands is important for the synchronized reduction of metal ions [26]. Because of their earth abundance and promising plasmonic and catalytic properties, Al and Cu have been deemed the metals of the future. However, the synthesis of these plasmonic NPs with an even higher tendency to oxidize (Al, Mg, and Cu) additionally requires a more specialized oxygen- and water-free setup. The use of Schlenk lines and glove boxes is common for such syntheses [27, 28]. Utmost care should be taken in handling the Grignard compounds produced from such protocols. The use of oxygen-free setups makes the process challenging to bring to scale. Yet, in the presence of chemically inert Au, the synthesis of alloy NPs of AuCu by a simple co-reduction method has been shown to yield stable alloy NPs compared with easily oxidizing Cu NPs [29]. Similarly, alloy NPs of different combinations, including Au, Pt, Pd, Rh, and Ni, have been synthesized by the co-reduction method [30–33]. Seed-mediated procedures can be used for the growth of different metal ions on separate crystal facets of the seed to afford greater control over the shape of the NPs [34], although it does not lead to homogeneous alloys and is more suitable for core–shell type structures [35, 36]. Thus, a subsequent thermal alloying step is important in seed-mediated processes for uniform distribution of the constituent elements. Furthermore, for galvanic replacement, one metal is oxidized, i.e. the sacrificial agent, by ions of another metal with a higher

redox potential. Complex bi- and trimetallic alloyed structures can hence be formed [37–39]. However, this technique is more prevalent for the synthesis of core–shell NPs (see Sect. 2.2) [40, 41].

In order to gain more control over the NP size distribution in colloidal syntheses, microreactor-based approaches are being studied nowadays [42, 43]. Here, reagents are introduced through microchannels at predetermined flow conditions. Uniform mixing in the microliter regime results in the production of a highly monodisperse colloidal solution of NPs with increased control over the size and shape [42]. By simply varying the flow conditions, different structures can be formed in a continuous flow. This offers an important time advantage over time-consuming trial-and-error syntheses using a batch setup. Nonetheless, understanding and controlling the flow and mixing conditions with high precision in a microreactor is challenging [43]. On the other hand, innovative colloidal synthesis techniques such as probe-based lithography also give a more controlled and varied geometry of NPs on a support material [44].

Although colloidal wet chemistry synthesis strategies have evolved significantly over recent years, they do not offer the highest degree of alloy structure control [23, 45]. For the formation of a more homogeneous AuAg alloy, sophisticated physical methods such as laser ablation are preferred [45, 46]. As mentioned before, the wet chemical modified Turkevich method leads to the formation of "core–shell type alloys" (Fig. 2a), while laser ablation generates a more homogeneous alloy (Fig. 2b). The latter is partially attributed to having no deviations from Vegard's law, which states that a linear relation exists at a constant temperature between the crystal lattice constant of an alloy and the concentrations of the constituting elements. Compared with laser ablation, colloidal synthesis induces negative deviations to Vegard's law forming a nonhomogeneous alloy [45–49]. In laser ablation, the laser energy is absorbed by a macroscopic target material, generating a plasma. This plasma expands and condenses in the liquid environment, forming nano-size materials due to cavitation. Therefore, it can be considered as a combined top-down (target material) and bottom-up (NPs from generation of plasma) approach. Laser ablation is more eco-friendly as laser irradiation produces species with high energy states without producing by-products and without the need for further high temperature treatment. Furthermore, often ligand-free alloys are produced with no additional chemical agents, apart from the solvent [45]. Very recently, laser ablation has also been used to form alloys by co-reduction of Au and Ag ions. However, it does not form ligand-free alloy NPs [50]. The high initial cost of laser technique is a drawback. Yet, considering operational costs at large scale, a study discussed laser ablation to be cost-effective in the long run. Currently used at an industrial scale, laser ablation can give output of NPs in the range of grams per hour, compared with milligrams per hour for wet chemical synthesis methods [51]. Magnetron sputtering can provide for a homogeneous multi-metal alloy, but is rather limited for use as a film deposited on a substrate. Consequently, it is difficult to hybridize sputtered metal NPs with another metal, semiconductor, or polymer, and as it is a surface-based phenomenon, it cannot be readily used for formation of nanoparticles inside porous materials [52–54]. Similarly, other chemical and physical methods such as chemical vapor deposition, lithographic patterning, thermal decomposition, or plasma synthesis are

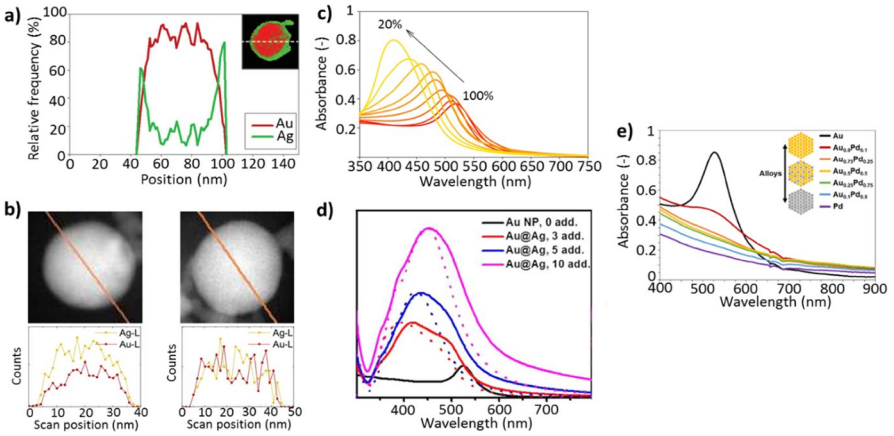

Fig. 2 Schematic representations of an EDX line scan of AuAg alloy NPs synthesized by **a** wet chemical co-reduction and **b** laser ablation. **c** Blue shift of the plasmon absorption band with decreasing Au percentage in AuAg alloy. **d** Absorption spectra of Au@Ag core–shell NPs. **e** Absorption spectra of a AuPd alloy with a sudden decrease of Au LSPR band with minor addition of Pd. Adapted with permission from **a** [23]. Copyright (2019) John Wiley & Sons, **b** [45] CC BY-NC 3.0, **c** [59]. Copyright 2016 Elsevier, **d** [60]. Copyright (2013), American Chemical Society and **e** [61] CC BY 4.0

time-consuming, expensive, or do not afford good control over the structural properties for hybrid systems [55–58].

As mentioned above, the combination of metals as alloys allows the tuning of optical properties. For instance, alloying of Au and Ag leads to an optical response which is the intermediary of those of pure Au and Ag [59]. Classically, the optical constants for different alloy compositions can be conveniently modeled with the Lorentz–Drude oscillator framework. Here, the interband transitions introduced by Au are captured by a suitable number of Lorentzian oscillators [62]. Thus, by increasing the Au fraction, the LSPR of NPs can be red-shifted with respect to pure Ag NPs, towards the LSPR of pure Au NPs, as observed from ultraviolet–visible (UV–Vis) absorption spectra in Fig. 2c, leading to structures with a larger Vis light absorption component. However, the incorporation of Au also leads to interband transitions that suppress the overall plasmonic enhancement [63, 64]. The advantage of alloying over incorporation of Au as a shell, core or a Janus particle, is that the compositional homogeneity provides a proportionate displacement of the LSPR with changing composition [62]. In the case of core–shell structures, however, the hybridization of the individual plasmon modes of the core and shell leads to complex spectral features [60, 65]. The proportionate variation of the extinction spectra of AuAg alloy NPs against the very complex extinction spectra of Au@Ag core–shell can be clearly observed from the examples in Fig. 2c, d. The optical features of core–shell NPs will be further discussed in Sect. 2.2.

Also, other alloy combinations including catalytic elements such as Pd and Pt and earth-abundant plasmonic metals such as Cu, Al, and Mg have gained considerable attention due to their promising application potential [30, 66, 67]. For instance, the incorporation of Cu in AuCu alloy NPs of different shapes such as nanospheres,

nanorods, nanocubes, and nanopentacles further push the LSPR band towards the red end of the visible light spectrum as compared with pure Au [29, 68–70]. For AuPd alloy systems, Pd introduces some specific catalytic activity, although it also progressively suppresses the plasmonic excitation, even by an addition as small as 10% (Fig. 2e) [61]. This is due to the large absolute values of the real part and the comparatively lower values of the imaginary part of the dielectric constants [71]. On the other hand, the sharp gradient of the imaginary dielectric constant enhances the refractive index sensitivity of the nanostructures [72]. For small NPs, < 10 nm, with weaker resonance (due to either size or quantum effects), the addition of a small fraction of a catalytic metal can quench the characteristic plasmonic response [73]. Because of a limited solid-phase solubility, the combination of Au and Pt limits the maximum size to 6 nm for full alloying. Hence, a strong plasmon resonance effect remains difficult for AuPt alloys with these very small sizes [73]. Similarly, such a limit in the solubility of Ag and Pt also leads to the tendency of forming core–shell structures [74].

Still, the addition of catalytically active metals such as Pd and Pt can certainly be beneficial. Several studies have already shown an enhancement in catalytic activity using alloy NPs due to a change in the electronic structure [59, 61, 68, 75, 76]. Alloying causes a shift in *d*-band levels with respect to the Fermi energy levels and therefore affects the overall reactivity. The dielectric constant of an alloy is not just a linear combination of that of the individual metals, partly due to changes in the *d*-band structure. In AuPd alloys, Pd loses *s*- and *p*-band electrons to Au and gains *d*-band electrons from Au and vice versa [75]. Alloying also introduces different interband and intraband transition states relative to their single metallic counterparts [77]. For example, alloying of Ag with Au can lead to suppression of interband excitations and favor intraband excitations which eventually results in higher hot electron energies [76]. The hot electron energy transfer also depends on the work function and the Fermi energy levels and therefore can be different for various materials including different alloys. Typically, it is ideal for the work function to be closer to the Fermi energy levels. These higher hot electron energies are eventually useful for photocatalytic reactions and will be further discussed in Sects. 3 and 4 [78]. It is important to note that to understand the properties of the wide spectrum of available materials, intensive computational studies are required. For example, Keast et al. studied the plasmonic response of alloying Au with various metal to show that only a set of combinations ($AuAl_2$, Au_3Cd, AuMg, AuCd, and AuZn) would have a better plasmonic response [79]. Although most of the computational studies focus on only one aspect, such as optical plasmonic response [65] or hot electron injection to band structure [80, 81], one alloy combination may behave differently for other catalytic reactions for various other reasons such as surface selectivity or surface energy. Therefore, rational design of materials is needed for each specific application (see Sect. 4).

2.2 Core–Shell

When the constituting materials (metal, semiconductors, or polymers) are not homogeneously distributed throughout the nanostructure volume, the intrinsic functionalities of the components remain (largely) intact [82, 83]. It is, however, important to

note that the plasmonic component is influenced extrinsically by the presence of the other components, such as an extra shell. For instance, a major effect present in most plasmonic core-dielectric shell configurations is the red shift of the plasmon band as the refractive index of the dielectric environment, i.e. the shell, increases [21, 84–87]. In the following section, different core–shell configurations are discussed in sub-classes.

2.2.1 Metal@Metal

A metal@metal core–shell configuration can broadly be of two kinds. Firstly, both the core and the shell can be plasmonic metals. Secondly, a plasmonic core or shell can also be combined with a shell or core of catalytic metal(s). In the first system, including combinations of Au, Ag, Cu, and Al, the optical properties are considerably different from their alloy counterparts. In the case of AuAg alloys, the extinction spectra shift linearly from the blue to red spectral region with increasing Au fraction (Au%) (Fig. 2c), whereas in Au@Ag core–shell systems, the spectral characteristics due to the hybridization of the individual plasmon modes of the core and the shell results in band broadening and complicated trends of the LSPR absorption band vs. Au% (Fig. 2d) [60]. The theoretical framework of plasmon hybridization given by Nordlander and co-workers is inspired by the molecular orbital hybridization theory. It explains the optical response of core–shell NPs where the core and the shell are separated by a non-conducting dielectric interlayer [88]. While not much literature is available on the implementation of the hybridization theory on metal@metal core–shell structures with no dielectric interlayer, the rigorous numerical solution of the Maxwell's equations is relatively convenient with established numerical codes to satisfactorily describe the optical properties [65]. Kamimura et al. studied core–shell Au@Ag/$SrTiO_3$ versus alloyed AuAg/$SrTiO_3$ for converting isopropanol to acetone and CO_2. It was shown that Ag in the AuAg alloy oxidizes, while being more stable by forming a shell in a core–shell structure. The authors explained the stability by stating that the chemical stability of the Ag shell can be enhanced by coupling to the Au core due to a charge transfer. This should increase electron density within the Ag shell, yielding a negative Ag oxidation state [89]. With the growing importance towards more abundant, but chemically unstable, plasmonic materials such as Cu, Al, and Mg, incorporation of a thin shell of Au is also seen as a viable stabilization strategy [90]. Use of Au as a shell is less detrimental to the plasmonic effect of the nanostructures as shown for Cu@Au NPs, especially as compared with the use of catalytic shells having a lower plasmonic response with plasmonic cores (e.g. Au@Pt) (Fig. 3a, b) [90, 91].

On the other hand, core–shell systems using a catalytic shell may still be preferred, depending on the application (e.g. Au@Pd systems for Heck coupling) [92]. In this second class, the plasmonic metal acts as an "antenna" and the non-plasmonic material as the adsorbing and reactive surface [93]. The optical and electronic properties of the plasmonic materials are thus utilized to enhance the reactivity of the non-plasmonic material. Whereas in alloys a complete new set of intrinsic properties is formed, in the case of core–shell NPs, the non-plasmonic shell has an extrinsic effect on the plasmonic core [4]. For instance, as mentioned above, a Pt

shell around Au nanorods increasingly dampens the plasmonic absorption intensity of the nanorods with increasing shell thickness due to the non-plasmonic response to light by the Pt shell (Fig. 3b) [91]. Similar to Au@Pt, the extinction spectra of Ag@Pd core–shell NPs are different from the extinction spectra of either Au or Pd. The general trend is that the LSPR in extinction spectra loses intensity along with a blue shift or red shift of the resonance frequency, while the spectral shape is broadened due to the coupling of the two materials. In addition to the optical properties, bimetallic core–shell structures can have starkly different catalytic activity from that of their alloy counterparts. For example, several Au@Pd core–shell configurations, especially with sharp branches, may have a slightly higher yield than AuPd alloys for both the Suzuki–Miyaura and Heck reactions (conversion of ~80 to 90 vs. up to 99%, respectively) [92]. Core–shell systems can furthermore be more easily tuned towards an antenna reactor system within their structure as compared with alloyed systems. An electronic and optical coupling with the plasmonic core hence enables enhanced activity [94]. Therefore, well-considered reaction-specific structures can be synthesized.

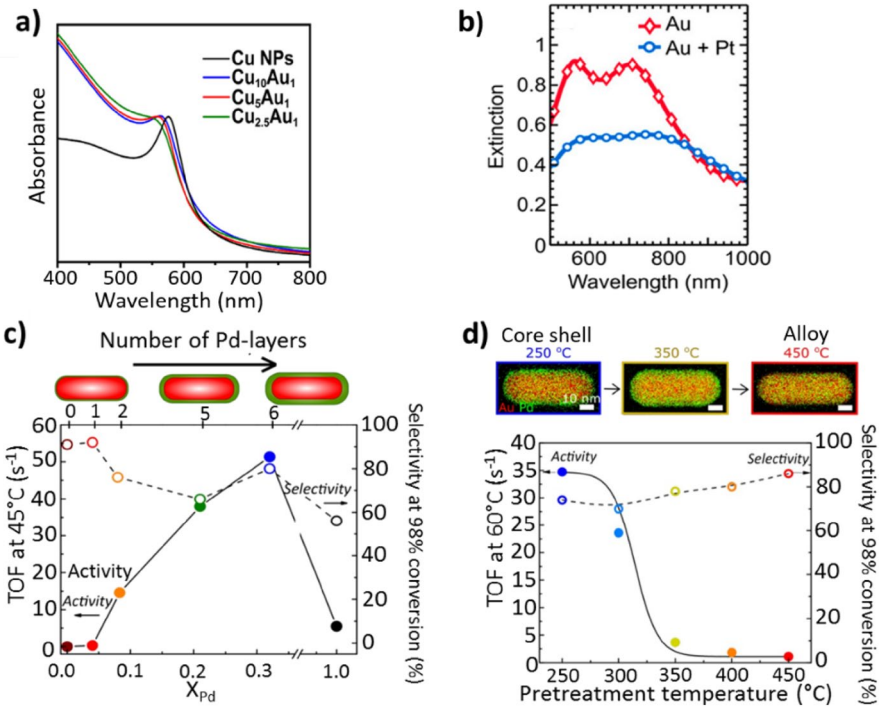

Fig. 3 Schematic representation of **a** the blue shift in UV–Vis absorption spectra of Cu@Au core–shell against **b** a dampened UV–Vis response of Au@Pt core–shell NP. Change in activity (represented by the turnover frequency (TOF)) and selectivity in Au@Pd core–shell NPs with **c** increasing Pd shell thickness and **d** gradually changing from core–shell to alloy. Adapted with permission from **a** [90]. Copyright (2021) American Chemical Society, **b** [91]. Copyright (2017) American Chemical Society, **c**, **d** [83]. Copyright (2021) Springer Nature

Metal@metal core–shell NPs are more commonly synthesized using colloidal synthesis methods with satisfactory control over NP size, shape, and morphology [95]. Co-reduction of metal precursors can yield core–shell structures when the difference between the reduction potentials of the constituent elements is sufficiently large [60]. In such systems, galvanic replacement can also lead to metal@metal core–shell structures with sub-nanometer shell thickness control [90]. During galvanic replacement, one element in a crystal lattice is replaced by another with higher reduction potential. Hence, certain reagent mixtures, such as Ag nanoparticles with Au^{3+} ions, always lead to spontaneous reactions. While the higher electronegativity of Au (1.9) than Ag (1.6) facilitates spontaneous formation of hollow Ag@Au core–shell systems by galvanic replacement, the formation of an Ag shell on Au NPs requires a reducing agent [96, 97].

With the recent advances, the synthesis procedures of core–shell NPs (just as for alloy NPs) have been developing in different directions such as microreactor-based synthesis, lithography, and laser ablation [98–100]. Some techniques are also specifically convenient for the synthesis of bimetallic core–shell NPs. For instance, Forcherio et al. generated a core–shell morphology by the exploiting the plasmonic excitation of the Au NP cores themselves. Sub-5-nm epitaxial growth of Pt ions could be achieved at plasmonic hot spots. The photodeposition of Pt on Au nanorods was activated by the longitudinal surface plasmon excitation of the nanorods [101]. Thus, a thicker shell was formed at the Au nanorod tips relative to the rest of the nanorod (the mean length was extended by 4.7 nm, while the diameter only increased by 0.72 nm). This is due to the fact that the longitudinal plasmon mode is manifold stronger than the transverse mode perpendicular to the axis of the nanorod. Another unique method for obtaining core–shell structures is oxidative etching. Van der Hoeven et al. generated core–shell morphologies by the etching of Au@SiO_2 NPs using H_2O_2 followed by the addition of a shell metal (Ag, Pd, or Pt) precursor. Thermal annealing resulted in better control over the shell morphology, while the shell thickness could be regulated from 3 to 10 nm via the metal overgrowth reaction time and precursor concentration [102]. The importance of the latter parameter should not be underestimated. Huang et al. used transient absorption spectroscopy to show how the shell thickness affects the hot electron decay pathways in Au@Pd NRs. It was shown that with the increase in shell thickness from only 0.4 to 2.8 nm, corresponding to 2–14 monolayers, the interaction of the hot Au electrons with the Pd interface lattice increased. This led to increased heat generation due to an increase in electron–phonon and phonon–phonon scattering of hot electrons from Au with a decrease in the recombination rate of electrons and holes. For a thicker shell of 5.4 nm or 27 monolayers, hot electrons were generated in the Pd shell itself to increase the Pd lattice temperature and reduce the heat capacity of Pd. Therefore, electron–phonon scattering of Au-generated hot electrons is slower when passing through the Pd shell. This also leads to accelerated recombination rates. Consequently, a lower ethylbenzene yield was recorded for the styrene hydrogenation reaction after 1 h of 100 mW cm^{-2} illumination (52% for 27 monolayers vs. 76% for 14 monolayers) [82]. In contrast, van der Hoeven et al. showed an optimal shell thickness of six atomic Pd monolayers around a Au NR core covered with mesoporous SiO_2 (Fig. 3c). They also showed that single-crystalline Au@Pd

core–shell structures performed more than 30 times better than the alloyed equivalents, displaying turnover frequencies (TOFs) of 34.7 and 1.1 s^{-1}, respectively, for the butadiene hydrogenation at 60 °C (Fig. 3d) [83]. Dedicated examples of hybrid metal@metal nanostructures in particular photocatalytic applications are discussed in more detail in Sect. 3.2.

2.2.2 Metal@Semiconductor

Mostly, plasmonic NPs are introduced to SCs to enhance photocatalytic efficiency of the SC, while simultaneously improving the metal stability. In metal@SC systems, the metal and the SC crystals are connected by a Schottky junction that facilitates electron–hole separation at the SC. In general, most of the works on metal@SC structures have been with TiO_2 as the shell covering a plasmonic core, resulting in structures such as Au@TiO_2, Ag@TiO_2, and Cu@TiO_2 [85–87]. Photocatalytic SCs mostly include metal oxides but also metal chalcogenides. The most convenient way to synthesize metal@SC core–shell nanostructures is by growing a shell of metal oxide precursor over plasmonic NPs. For the shell growth, metal oxide precursors are added to colloidal plasmonic NPs, and the precursor molecules bind to the surface ligands on the particle surface [85]. Using the metal oxide precursor itself as the reducing and capping agent for the formation of plasmonic nanoparticles further simplifies the process [103]. Generally, titanium isopropoxide, titanium butoxide, or titanium fluoride is used as Ti precursor, forming crystalline TiO_2 shells from 5 nm to more than 100 nm in thickness [85, 104]. In order to form uniform shells, controlled interaction of the precursor with the capping ligands and controlled hydrolysis and condensation of the precursors are highly important. Anhydrous solvents or slow hydrolyzing precursors such as titanium(IV) (triethanoloaminato) isopropoxide tend to give more uniform shells of thickness down to 2 nm (Fig. 4d) [105]. Since unstable metals like Ag, Cu, and Al may oxidize during the subsequent annealing step required for crystallization of the oxide shell, hydrothermal crystallization procedures are often adopted. Alternatively, the photothermal effect of the plasmonic NPs itself can also be used for controlled TiO_2 shell formation by laser irradiation [106]. Different configurations such as Ag@TiO_2 nanowire arrays can also be formed using templated lithography [107]. The feasibility of core–shell structures by atomic layer deposition of ZnO on Ag nanoparticles was demonstrated as well [108]. The effect of the metal oxide shell comes from the interband excitations as well as elastic scattering. For instance, a dielectric SiO_2 shell around plasmonic nanoparticles contributes to the total scattering, which increasingly dampens the plasmon band with increasing shell thickness [109]. Importantly, it was also shown for Au@Cu_2O core–shell systems that the plasmonic response of the core depends on the crystal facets of the shell, which enable further optical tuning of these hybrid structures [110]. Note furthermore that sometimes M@SC core–shell materials form spontaneously. For instance, Al oxidizes very easily, generating a thin 2–3-nm self-limiting oxidized layer [111]. Better stabilization strategies are required for such chemically unstable metals in order to use them in realistic photocatalytic applications at industrial scale.

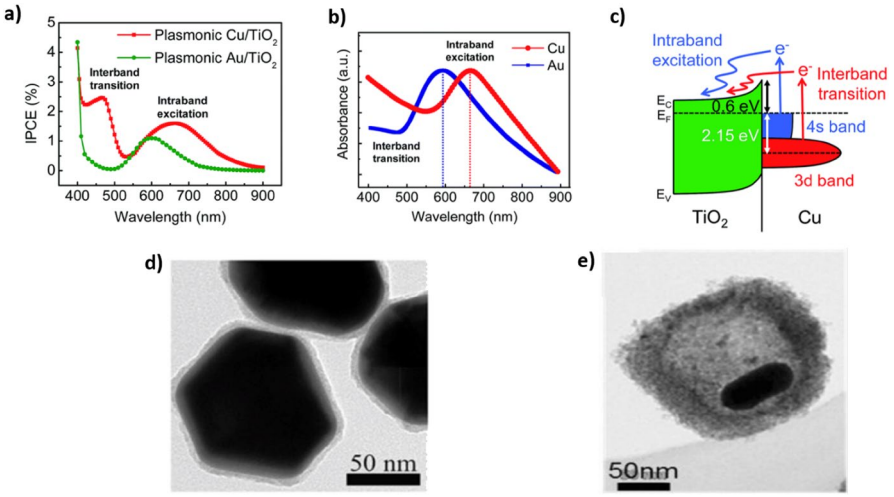

Fig. 4 Schematic representation of the interband transition and intraband excitation in **a** Au@TiO_2 vs. Cu@TiO_2 material system, showing the incident photon to current efficiency (IPCE) as a function of the wavelength, and **b** single Cu and Au NPs. **c** Contribution of both intraband excitation and interband transition in Cu@TiO_2 contact material system. TEM image of **d** Au@TiO_2 core–shell nanoparticle and **e** Au@TiO_2 nanorod yolk shell structure. Adapted with permission from **a–c** [78]. CC BY-NC 3.0, **d** [105]. CC BY-NC-ND 4.0, **e** [123]. Copyright (2015) John Wiley and Sons

Over the past few decades, additional Vis light-active SCs such as Cu_2O, g-C_3N_4, CuS, and CdS have gained considerable attention for constructing plasmonic hybrids [112–115]. Lee et al. developed Ag@Cu_2O nanoparticles with varying shell thickness and observed higher photocatalytic activity with increasing shell thickness. Photocatalytic degradation of methyl orange (MO) under Vis light with 11-nm Ag core@11-nm Cu_2O shell NPs was completed in 1 h compared with only ~5% degradation by Cu_2O NPs. The higher activity was ascribed to the increase in surface area from 14 to 25 $m^2\ g^{-1}$ as well as the stabilization by the increasing shell thickness. Density functional theory (DFT) studies showed that as Cu_2O is in a metastable state, a thin shell of about 5 nm Cu_2O transforms into CuO and detaches from Ag. On the contrary, with thicker shells of about 15 nm, Cu_2O holds Ag and CuO together. This is explained by the large adhesion force between Cu_2O and CuO or Ag as compared with the adhesion forces between CuO and Ag. The long-term stability of Cu_2O is still an issue [114]. Interesting non-oxide semiconductor studies include the work of Ma et al. Four gap-(Au/AgAu)@CdS nanostructures were synthesized using several Ag and Au shell growth and galvanic replacement cycles. The nanoscale Kirkendall effect yielded nanogaps that resulted in efficient plasmonic coupling. Hence, broad absorption from UV to NIR was created, increasing the H_2 production activity under Vis light ($\lambda > 420$ nm) 47-fold relative to Au@CdS without nanogaps (4.71 vs. 0.10 mmol $g^{-1}\ h^{-1}$) [113]. This configuration maintains its activity over 24 h. Nonetheless, CdS is susceptible to photocorrosion, and long-term stability remains an issue. Thus, further modifications may be necessary for true long-term photostability [116].

When selecting a semiconductor shell, an important aspect is the band structure of the material. The characteristics of the metal@SC interface depend on the Fermi level of the metal and the relative position of the band edge potentials of the SC. Also, the induced electronic states at the interface may play a role [117]. For higher visible light activity, a small band gap (1.6–3 eV) is preferred. However, the CB level should be sufficiently high and the valence band (VB) level should be sufficiently low to enable the desired redox reactions. The plasmonic metal should also be carefully chosen, as selection of plasmonic cores with strong plasmonic excitement does not necessarily guarantee effective energy transfer and thus activity enhancement of the SC shell. Interband and intraband energy levels also play a very important role in energy transfer from metal to SC. Studies have revealed that Cu@TiO_2 leads to higher hot electron injection compared with Au@TiO_2. Cu@TiO_2 contributes to both interband and intraband energy, with a lower Schottky barrier height, whereas Au@TiO_2 has greater interband energy but also greater Schottky barrier height, leading to inefficient hot electron extraction (Fig. 4a–c) [78]. Hence, using an alloy NP with an appropriate energy band structure as a core could represent a promising approach [76]. More detailed mechanistic insights are provided in Sect. 3.

Finally, yolk–shell structures can be considered as an extension of core–shell configurations. These consist of a plasmonic core material covered by a hollow shell of, for instance, a SC material (Fig. 4e). Such structures lead to different optical properties, as only a fraction of the plasmonic core material is in physical contact with the shell. The cavity volume leads to total internal reflections which enable the incoming light to be further used for photocatalytic reactions [118]. Au@TiO_2 yolk–shell structures were shown to have a reflectance of less than 15% compared with 63% for commercial P25 TiO_2. This is thus attributed to the internal reflections within the cavity of the yolk–shell structure [119]. For obtaining such structures, one can use a sacrificial material (e.g., organic compounds) to form a temporary shell. The latter will be removed after the real SC shell formation [120]. Apart from sacrificial templating, other mechanisms such as Ostwald ripening and the Kirkendall effect may also lead to a yolk–shell structure [121, 122]. Along with a change in the optical properties, such structures make way for higher specific surface area. Li et al. reported a surface area of 310 $m^2\ g^{-1}$ for yolk–shell Au@TiO_2 NRs relative to 56.9 $m^2\ g^{-1}$ for Au@TiO_2 core–shell nanoparticles [123]. For more details, one can refer to the outstanding review of Li et al. on the complex formation mechanism of yolk–shell nanostructures, along with the photocatalytic mechanisms involved [118].

2.2.3 Metal@Polymer NPs

Introducing an organic layer around metal NPs may be done for several reasons, such as improving stability, ensuring compatibility with organic solvents, influencing the activity, and improving the optical properties. Firstly, a distinction should be made between surface ligands and polymer shells. Surface ligands such as thiols, amines, oleate, and xanthate are often used for the colloidal stabilization of plasmonic NPs [124, 125]. Conventionally, plasmonic NPs are synthesized by wet

chemistry techniques consisting of metal precursor reduction with reductants such as $NaBH_4$ (fast nucleation) or ascorbic acid (slower growth). The ligand may be added along with or after the reductant. When both are added simultaneously, the ligand may act as a shape-directing agent by preferentially binding to a specific crystal facet [126]. Importantly, in some instances, the same reagent can function as both reducing agent and stabilizer, e.g., citrate in the modified Turkevich method for the synthesis of Au_xAg_{1-x} NPs [23, 59, 127, 128]. The longer the alkyl chain, the easier the transfer to organic media, although nonpolar solvents may remain difficult for the suspension of plasmonic NPs [125, 129]. From the perspective of stability, xanthate-capped NPs show relatively high oxidative corrosion resistance compared with thiol or oleate capping. In contrast, these NPs are more temperature-sensitive, due to the thermal decomposition of xanthate [125].

Polymer shells, on the other hand, can be created around the NPs by a separate polymerization step [129] or in a simultaneous process of NP and shell formation [130]. Other synthesis methods such as electrospinning provide geometric confinement from nanofibers and therefore afford control over the optical and electrical properties. Chen et al. [131] prepared Ag@poly(vinyl pyrrolidone) (PVP) nanofibers by coaxial core–shell electrospinning with $Ag(NH_3)_2^+$. The PVP enabled appropriate viscoelastic properties for the nanofiber patterns and protection of Ag, which proved to be more effective than for smaller molecules such as citrate [132]. Kvítek et al. also demonstrated the superiority of a PVP coating for Ag NPs in terms of the aggregation resistance, compared with another neutral polymer, poly(ethylene glycol) (PEG), due to the strong bond between Ag and the N atom in the pyrrolidone group [133].

However, the drawback with most organic linkers and single polymers is the lack of shell thickness control [21]. This is of paramount importance as the near-field enhancement (NFE) generated by the excited plasmonic NPs decreases with distance and the coupling of plasmons is strongly distance dependent as well [5]. Electromagnetic near-field hot spots may be generated by placing plasmonic NPs in close proximity of each other (up to $\times 10^6$ field enhancement for an interparticle distance of ~ 1 to 3 nm depending on the dielectric constant of the surrounding medium [5, 84]). Since the reaction rate of photocatalytic reactions is proportional to the square of the near-field, stronger electromagnetic fields are highly beneficial for photocatalytic reactions (cfr. Sect. 3.1.1) [5]. In order to meet these requirements of accurate control over thin shell thickness, the layer-by-layer (LbL) technique has been applied where different polymer layers are alternatingly deposited around a metal core. Lisunova et al., for example, applied water-soluble PVP and poly(methacrylic acid) (PMAA) layers on Ag nanocubes based on hydrogen bonding. A buffered pH 3.5 environment ensured PMAA acted as an H bond donor and PVP as an H bond acceptor. Excess polymers were removed by careful centrifugation. This enabled nanometer level control over the shell thickness [134]. Schneider and Decher introduced the use of polyelectrolytes to 13.5-nm Au NPs, namely the positively charged poly(allylamine) hydrochloride (PAH) and negatively charged poly(sodium 4-styrenesulfonate) (PSS). Up to at least 20 layers could be applied based on electrostatic attraction, with minimal particle aggregation (> 95% NP recovery), yielding 7.5-nm shells [135]. Furthermore, to prepare eventual scale-up, they determined the range

of practical concentrations to avoid bridging flocculation [136]. Asapu et al. further improved the LbL protocol by replacing PSS by the cheaper polyacrylic acid (PAA), also lowering the deposition time from 12 to 0.5 h. They were able to deposit layers on 20-nm Ag [21, 137] and Au [138] nanospheres with sub-nanometer precision. These LbL-stabilized Ag nanoparticles were shown to be ultra-stable in harsh reactive environments (hot air and NaCl solutions) [22]. A similar LbL approach is also extended to bimetallic AuAg nanoparticles wherein the nanoparticles were proven to be stable after aging the sample for 10 months. Stability of LbL stabilized against bare bimetallic AuAg nanoparticles in hot air can be observed in Fig. 5a, b [139]. Note that due to the centrifugation steps to discard the excess polymers, LbL techniques are mainly suited for larger NPs. It is considered that NPs smaller than 7 nm would lead to disproportionate centrifugation losses.

The aforementioned polymers are however all nonconductive which excludes the potential transfer of hot electrons (see also Sect. 3.1.1). Therefore, the use of conductive polymers such as poly(3,4-ethylene dioxythiophene), poly(pyrole) and poly(aniline) (PANI) have also been studied [130, 140]. Yang et al. assembled Au-TiO_2 using PANI. They proposed that PANI can also act as an electron donor because of the electron excitation from π to π^* orbitals, induced by visible light [141]. Xing et al. designed a kinetically controlled in situ polymerization protocol for aniline with sodium dodecyl sulphate (SDS) on the Au surface. This one-step synthesis enables control over the shell thickness by adjusting the polymerization time. Shells on 22-nm Au nanospheres grew up to 14 nm after 4 h. A further increase (14–92 nm) was achieved after multiple growth cycles by this "mix-and-wait" technique. Furthermore, the formation of nanochains of 2–20 NPs could be

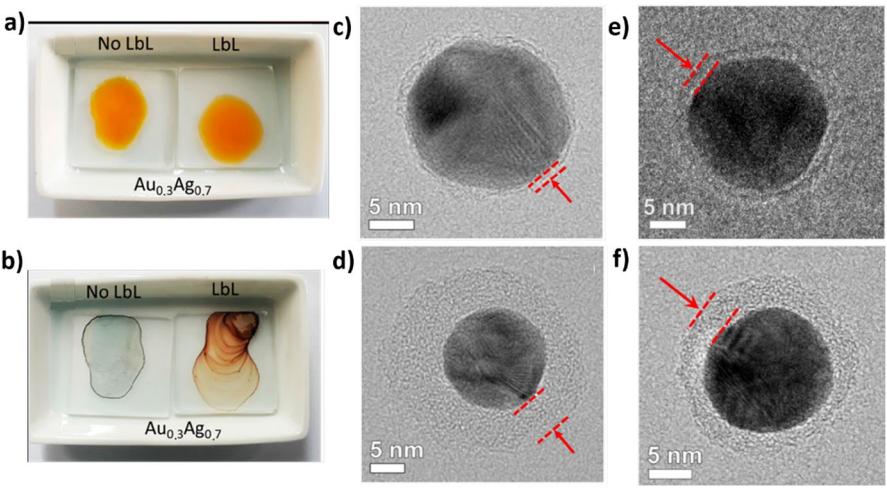

Fig. 5 LbL stabilized and bare bimetallic AuAg NPs **a** before and **b** after treatment at 100 °C. TEM image of varying polymer shell thickness of Au@PANI core–shell NP as a function of time from **c** 30 min to **d** 180 min. TEM image of LbL stabilized Au@polymer core shell nanoparticle with increasing shell thickness by varying number of layers from **e** 4 layers to **f** 12 layers. Adapted with permission from **a**, **b** [139]. CC BY 4.0, **c**–**f** [84]. Copyright (2019) American Chemical Society

controlled by the timing of SDS addition [130]. Asapu et al. compared varying thickness of PANI shells against polymer shells of PAH and poly(styrene sulfonate) sodium (PSS) synthesized using LbL strategy (Fig. 5c–f). Conductivity of PANI shells was effectively proven using conductive tip atomic force microscopy [84]. Later, this synthesis protocol has also been applied for other particles such as Au nanocubes [142] and Ag nanospheres [143].

The addition of a polymer shell also affects the optical properties due to the change in the dielectric environment [144]. As mentioned before, an increasing refractive index yields spectral red shifts, while the opposite leads to spectral blue shifts. Thus, small red shifts (1–3 nm) in the UV–Vis spectra can be observed with the formation of each PAH and PAA polymer layer over AuAg alloy nanospheres in the LbL process [139]. On the other hand, Lisunova et al. demonstrated blue-shifts after the addition of PVP or PMAA. When the fluorescent poly(*p*-phenylene ethynylene) was coated as the final layer on this LbL assembly, the actual shell thickness did not seem to change the fluorescence peak positions [134]. Recently, more research has been done on "plasmonic switching" where shifts are quickly induced for metal@polymer NPs. Hence, Lu et al. [145] showed that when applying small potentials (−0.1 to +0.5 V vs. $V_{AgClIAg}$), large plasmon shifts up to 150 nm can be attained for colloidal Au nanospheres, NRs, and nanobipyramids covered by PANI. The small potential changes enable swift switching in less than 10 ms between the half-oxidized and fully reduced states, without degradation of the PANI shell. This is 20,000 times faster than for proton doping and de-doping by adding acids or bases [145]. Finally, for certain volume phase transitions (VPT) polymers, the optical properties of metal@polymer NPs can be adjusted easily by varying an external parameter [146]. For example, poly(*N*-isopropylacrylamide) (PNIPAM) is a thermo-responsive polymer that undergoes a VPT in aqueous media. The condition for this is a temperature larger than its lower critical solution temperature (~ 32 °C). Hence, the wavelength-dependent dielectric constant peak increases and shifts from 555 nm at 23 °C to 587 nm at 44 °C [146]. These features may be advantageous for, e.g. sensing applications. For more information about sensing, optical data storage, imaging, and photothermal gel applications using plasmonic metal-polymer nanohybrids, the interested reader is referred to the outstanding review of Pastoriza-Santos et al. [147]. Metal@polymer NPs in photocatalytic applications will be further discussed in Sect. 3.2.

2.3 Other Structures

Combination of plasmonic materials with another functional material may also lead to other structures than conventional alloys or core–shell NPs. For instance, Janus nanoparticles are formed when the plasmonic part has a partial interface with another material, either metal or semiconductor, of a comparable size [148]. Partially covering shells are engineered to expose the plasmonic metals to the chemical environment. The interface can be the most reactive part of the plasmonic photocatalyst as the energy transfer from plasmons to the catalyst would be theoretically considered to be the highest directly at the interface. Further, it decreases as the

shell thickness increases [149]. Au-TiO_2 usually dominates the field of metal–metal oxide-based Janus materials in photocatalysis (Fig. 6a). These Janus structures can also be synthesized for various shapes of plasmonic NPs such as NCs and NRs [150]. Figure 6b shows how Janus NPs can create a higher near-field enhancement at the Au-TiO_2 interface as compared with core–shell NPs. Synthesis of these nanoparticles, going from Janus to core–shell, can be controlled by varying the volume of TiO_2 precursor solution [148]. Templated methods have also been used to synthesize Janus nanostructures [151].

Since a conformal shell can cause significant plasmon damping, some studies developed a method to selectively deposit catalytic material at the hot spots of a plasmonic antenna, e.g. the edges of cubes or the tips of a rod [152, 153]. Partial shell formation on the antenna retains the strong plasmonic response, thus leading to higher enhancement in reactions compared with fully shielded particles. Electron energy loss spectroscopy (EELS) maps of Au octopods with AuPd tips show spatially localized resonances around the tips and edges relating to different plasmon modes [154]. Protocols for similar Au-semiconductors heterostructures have been designed as well, e.g. CdSe NRs with Au tips. Introducing the Au tips resulted in a more than 27% increase in the photocatalytic quantum efficiency for hydrogen generation [155]. Lee et al. further showed that the deposition of Cu_2O on hexaoctahedral Au vertices resulted in TOFs for CO oxidation under Vis light illumination that were twice as high as those of their core–shell counterpart [156]. High charge transfer efficiency is also observed for flower-shaped Au-ZnO hybrid Janus type NPs [157]. The fact that only Au has been used as a plasmonic metal in Janus structures

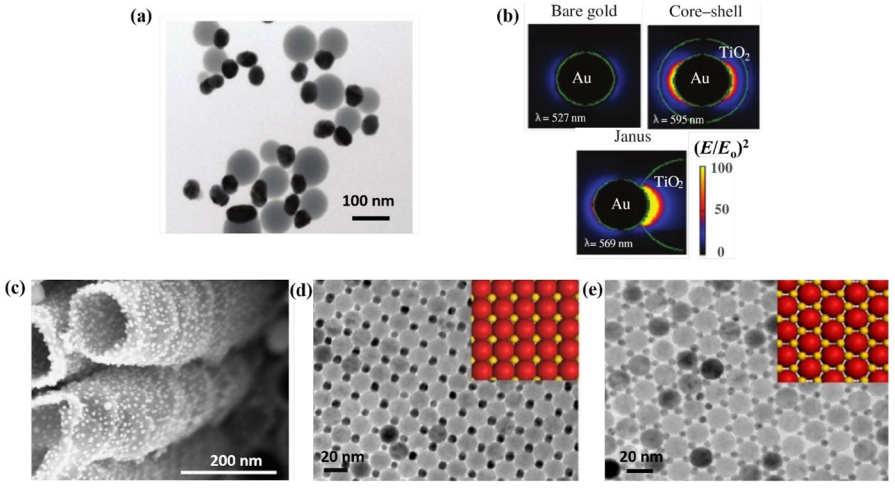

Fig. 6 **a** Transmission electron microscopy (TEM) images of Janus Au-TiO_2 NPs **b** near-field enhancement map showing maximum enhancement for Janus NPs compared with bare Au and Au@TiO_2 core–shell NPs, **c** Scanning electron microscopy (SEM) image of Au NP decorated TiO_2 nanotubes ((T)NTs). **d** TEM image of binary superlattice of Au and Fe_2O_3 NPs in 1:1 and **e** 1:3 Au:Fe_2O_3 ratio for catalytic applications. Adapted with permission from **a**, **b** [148]. Copyright (2012) John Wiley and Sons, **c** Royal Society of Chemistry [162]; permission conveyed through Copyright Clearance Center, Inc., **d**, **e** [178]. Copyright 2013 American Chemical Society

is due to the limitations offered by this structure. Other plasmonic metals such as Ag, Cu, and Al would oxidize too easily in a Janus structure due to the partial exposure of the metal to the (oxidative) environment. More insights on the effect of several configurations on the actual photocatalytic activity are described in Sect. 3.2.

In similar structures, the plasmonic or the non-plasmonic part is much smaller than the other. In those cases, the smaller part can be present in a large number over the surface of the larger core [158–161]. The advantage of such structures is quite similar to that of Janus structures. For instance, when a metal oxide is decorated with Au NPs, such as in Fig. 6c, the plasmonic NPs in large numbers give rise to the plasmonic coupling effect with further enhancement in the plasmonic excitation [162]. Apart from the usual plasmonic enhancement in photocatalysis by such structures [163, 164], the broader spectral bandwidth facilitates solar energy harvesting applications such as solar seawater desalination [165, 166]. When plasmonic NPs are combined with a magnetic core in a similar fashion, an additional magnetic functionality can be exploited in their applications [159, 167]. Similar plasmonic incorporated structures can be made with different materials such as ZnO, WO_3, WS_2, and MoS_2 [168–173]. Simple photo-impregnation and electrodeposition of plasmonic nanoparticles are widely known techniques for the synthesis of such hybrid NPs [128, 174]. Conversely, a plasmonic core can also be decorated with non-plasmonic smaller clusters for different targeted applications. For instance, Au NPs decorated with clusters of Pt [175, 176], Pd [177], etc., are interesting for plasmon-enhanced catalytic applications.

Although they are difficult to hybridize due to their tendency to aggregate, single atoms and atomic clusters (< 2 nm) form another peculiar class of plasmonic materials. Plasmonic atomic clusters have unique properties due to quantum confinement effects that occur at such small sizes [179–184]. Zheng et al. stated that sub-nanometer sized clusters have discrete energy levels. They are too small to contain a continuous density of states which is the basis of plasmonic characteristic of free electron metal NPs [182]. The jellium model was used to predict plasmon width and nanocluster transition energy (E_{gap}) and it was identified that both these properties scale inversely with the cluster radius. As the number of atoms in the cluster increases, the energy gap decreases, quantitatively fit by the following expression for small nanoclusters (< 25 atoms) (Eq. 1):

$$E_{gap} = E_{Fermi}/N^{1/3} \tag{1}$$

With E_{gap} the nanocluster transition energy, E_F the Fermi energy of the metal and N the number of atoms.

Because of these quantum effects, plasmonic metal clusters show a different photocatalytic behavior. The high ratio of surface atoms in such metallic clusters allows for a better interaction with the reactants. However, the high availability of active surface sites does not always lead to a suitable catalyst for a specific product. The number of atoms within the atomic cluster plays an important role because of the changing physical properties at the discrete energy levels, in turn having an effect on the kinetics of the reaction under consideration [185–187]. Metal clusters have a strong tendency to migrate and aggregate into NPs of larger size. Thus the synthesis

of such atomic clusters and more hybridized derivatives is also far from easy, as it is difficult to stabilize a precise number of atoms without coalescence [188]. Cluster beam deposition (CBD) is one such solvent-free technique used to synthesize alloyed and core–shell atomic or nanoclusters. Here, aggregates formed in the gas phase are processed in a molecular beam source. Hence, a collimated beam of particles is generated which can then be intercepted by a substrate to form thin films [189]. To characterize such atomic clusters in detail, one would need state-of-the-art synchrotron facilities [188, 190]. Liao et al. have applied the CBD method for depositing 2–8 monolayer equivalents of Au nanoclusters on a TiO_2 surface for self-cleaning applications under pure visible light [180].

Plasmonic nanoclusters can also be incorporated in zeolites, covalent organic frameworks (COFs), and metal organic frameworks (MOFs) due to the high porosity and surface areas of the latter (up to 10^3–10^4 m^2 g^{-1}) [191–193]. By combining zeolites, COFs, and MOFs with plasmonic materials, another class of plasmonic hybrids is created. In a recent study by El Roz et al., ZX-Bi zeolites played the role of support material to grow Ag clusters. The < 1 nm clusters, being in close proximity inside the zeolite cages, tend to exhibit unique optical properties. Here, the zeolites do not show any methanol photooxidation but the photocatalysis tends to occur directly on the surface of the Ag clusters with a methanol photooxidation rate of 49.60 mmol g^{-1} cm^{-2} [192]. However, next to their role as support materials, zeolites, COFs, and MOFs may also act as photocatalysts, similar to metal@SC systems [192, 194, 195]. In addition, these highly porous structures can have selective functional groups. For example, in the case of aluminum crystals enclosed with MIL-53 as a core–shell structure, MIL-53 enhances CO_2 adsorption by five times due to the hydroxyl groups present in the MOF structure. It also enhances CO_2 reduction by a factor of 2 [196].

Apart from these inherently hybrid nanostructures, plasmonic enhancement can also be achieved extrinsically by ordered hybrid systems. For instance, binary superlattices of a plasmonic and another functional NP are hybrid plasmonic systems extending over large areas [178, 197, 198]. Figure 6d, e shows two conformations of a binary Au and Fe_2O_3 superlattice. Ordered 2D layers of such hybrid structures possess tremendous potential for different applications such as catalysis and sensing. Chemical reactions can be locally enhanced in a nanogap between plasmonic and catalytic antenna reactor systems. These systems consist of (at least) two separated NPs: a plasmonic antenna which collects light, and a catalytic reactor which facilitates the reaction [199]. Each NP retains its individual electronic structure as long as there is no electron tunneling (true only for a separation of greater than 1 nm) [200].

3 Hybrid Plasmonic Nanostructures in Photocatalysis

Later in this review article, the potential of the aforementioned classes of plasmonic hybrids will be discussed for several major photocatalytic applications such as H_2 generation, pollution abatement, and CO_2 conversion. But first we briefly take a closer look into the underlying mechanisms of hybrid plasmonic enhanced photocatalysis. Since this review aims at plasmonic hybrids and their role in photocatalysis,

the interested reader is referred to the excellent review of Ma et al. for a more detailed discussion of the underlying plasmonic physics [201]. Here, also, special attention is given to how these hybrids are helpful in the elucidation of the right mechanism.

3.1 Plasmon-Enhanced Photocatalytic Mechanism

3.1.1 General Aspects of Photocatalysis and the Role of Plasmonics

Over the past four to five decades, a large variety of semiconductor photocatalysts have been studied that generate electron–hole pairs upon the absorption of light with an energy content large enough to overcome the SC band gap (Fig. 7a). These photogenerated charge carriers (i.e. holes in the valence band and electrons in the conduction band) migrate to the surface of the photocatalyst, where they initiate (a cascade of) redox reactions forming reactive oxygen species (ROS). Among all SCs studied, TiO_2 has been investigated more extensively than any other material due to its high chemical and thermal stability, appropriate conduction band and valence band positions, low cost, and non-toxicity [202]. However, as mentioned before, the photoactivity of TiO_2 is hampered by a large band gap value (ca. 3.2 eV) which restricts its use to applications involving UV light only [201]. In that context, plasmonic nanostructures have emerged as a promising solution for a more optimal utilization of the solar spectrum due to the presence of the LSPR phenomenon. Unlike conventional light absorption processes by molecular sensitizers or interband excitation of metals, LSPR involves a *multi*-electron excitation that concentrates the absorbed light energy at the NP surface in the form of intense electric fields [203]. Thus, plasmonic nanostructures can work as nano-antennas in light-driven processes to capture electromagnetic energy. Direct potential applications of this phenomenon (other than photocatalysis), are several orders of magnitude enhancement of IR and Raman signals, enabling highly sensitive surface-enhanced infrared absorption (SEIRA) [204] and SERS [205].

Once a plasmon is excited, it can decay in two competitive ways: through re-emission of photons, or by non-radiative relaxation through electron–electron, electron–phonon, electron–surface, or electron–adsorbate scattering [206–208]. The re-emission phenomenon is captured by the classical electromagnetic framework as the elastic scattering of an electromagnetic wave. Hot electrons that are not in thermodynamic equilibrium with the atoms in the material, are generated during the non-radiative relaxation process, primarily through electron–electron scattering [201]. The intense LSPR energy generated near the surface of the plasmonic NPs can then be transferred to a SC photocatalyst in contact with the plasmonic NPs. In this way, the photocatalytic activity of the SC is improved by the plasmonic NPs "indirectly," as will be further discussed. On the other hand, the LSPR energy can also be transferred "directly" to molecules adsorbed at the surface of the plasmonic NPs [209]. In that case, the plasmonic NPs thus simultaneously act as the light absorber and as the catalytic active site. An increased photoactivity, as well as selectivity, have been demonstrated for reactions based on this direct plasmonic reaction concept [210].

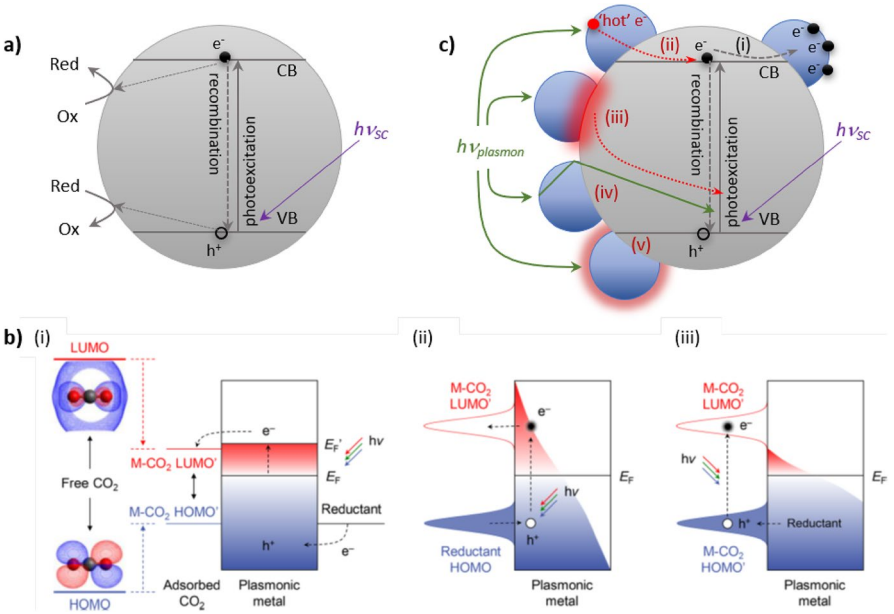

Fig. 7 Schematic representations of **a** the activation of a SC photocatalyst, **b** the potential mechanisms driving direct plasmonic catalysis illustrated for CO_2 activation: (i) charging/discharging of the plasmonic NP, (ii) chemical interface damping, (iii) direct photoexcitation of the metal-CO_2 complex, **c** the potential mechanisms driving plasmon-mediated SC photocatalysis: (i) the electron sink effect, (ii) hot electron transfer, (iii) near-field enhancement, (iv) resonant scattering, (v) local heating. Adapted with permission from **b** [224]. Copyright 2017 American Chemical Society

Three different main mechanisms have been proposed to explain this direct activation of adsorbed molecules by plasmonic excitation under visible light, as illustrated in Fig. 7b for the specific case of CO_2 activation:

(i) *NP charging/discharging* ((i) in Fig. 7b): plasmonic NPs are charged by steady-state excitation in the presence of a hole scavenger, and subsequently discharged by transferring photoexcited electrons to the lowest unoccupied molecular orbital (LUMO) of the metal (M)–CO_2 complex, thus forming $CO_2^{\cdot-}$ or a related species.

(ii) *Chemical interface damping* ((ii) in Fig. 7b): a fraction of the hot electrons can coherently scatter into the unoccupied states of the adsorbed CO_2 molecule [211], leading to vibrational activation of CO_2 for further reaction [212].

(iii) *Direct photoexcitation of the* M–CO_2 *complex* ((iii) in Fig. 7b): CO_2 molecules adsorbed onto a plasmonic metal surface are activated through direct excitation of the hybridized electronic states of the M–CO_2 complex [213].

As mentioned earlier, the activity of a semiconductor photocatalyst can also be improved "indirectly" by coupling it to a plasmonic NP. This is the most common and widely encountered type of plasmonic photocatalysis, and has been demonstrated for various metal/SC composites such as metal/TiO_2, metal/

ZnO, metal/Fe_2O_3, and metal/CdS, with photocatalytic applications in organic pollutant degradation, hydrogen production and CO_2 conversion, amongst others [214–217]. The main mechanisms that have been proposed to determine this plasmon-enhanced SC photocatalytic activity include:

(i) *Promoting charge separation in the SC* ((i) in Fig. 7c). When a junction between an *n*-type SC such as TiO_2 and a metal NP is formed, a Schottky barrier is created at the equilibrated interface, which limits the reverse metal to SC transfer [218]. This is also known as the electron sink effect. Although this is not a plasmonic effect as such, it may still contribute significantly to the overall efficiency enhancement.
(ii) *Hot electron injection from plasmonic metal NPs to the SC conduction band* ((ii) in Fig. 7c). LSPR-mediated hot electrons and holes produced and separated at the interface between the plasmonic metal NP and the SC, diffuse to the SC surface to participate in the further photocatalytic reaction. It is important to understand that this mechanism absolutely requires that the SC is in electrochemical contact with the plasmonic metal [219–221].
(iii) *Near-field enhancement in the SC* ((iii) in Fig. 7c). The strong plasmon-induced electric field near the plasmonic metal surface can significantly enhance the rate of photoexcitation in the nearby SC. In this case, it is crucial that the SC absorption spectrum and the LSPR spectrum overlap [222].
(iv) *Increase of the optical path through resonant scattering* ((iv) in Fig. 7c). Especially for large metal NPs (sizes comparable to the light wavelength [4]), the contribution of scattering to the total extinction becomes important. The more efficient scattering of incident light creates the effect of a mirror that prolongs the optical path length of incident photons throughout the SC. Hence, the probability of successful photo-excitations increases [5].
(v) *Local heating* ((v) in Fig. 7c). The non-radiative damping of the excited plasmons eventually leads to energy dissipation to the surrounding environment as heat. Depending upon the intensity of radiation and the thermal properties of the surrounding, this can result in temperature rise in the vicinity of the NPs. This effect is mainly important for ordered NP assemblies that can exhibit enhanced absorption by plasmonic coupling and high particle density per unit area with the additional condition that the incident irradiance is sufficiently strong. Thus, the heating effect is less dominant for single NPs and under ambient conditions [223].

In what follows we will mainly focus on plasmon-enhanced SC photocatalysis as this also offers high-impact real-life applications under ambient conditions. Indeed, while several excellent reports are available on direct plasmon-catalyzed reactions, these systems typically rely on more stringent reaction conditions, such as high irradiance levels (e.g. up to 20 sun equivalents or lasers), dedicated optical hardware (parabolic reflectors, lenses, etc.) or involve the interplay with heat [209].

3.1.2 Mechanistic Studies Using Hybrid Plasmonic Nanostructures

Unraveling the precise plasmonic-SC interaction mechanism driving the photocatalytic reactions is quite challenging. The relative importance of the various potential pathways (cfr. Fig. 7c) is still a matter of ongoing debate. The radiative damping of the plasmons results in scattering, i.e. energy loss to the surrounding, while non-radiative damping leads to generation of energetic hot electrons which can enhance photocatalytic reactions. In most cases, however, the loss by scattering can be safely neglected, as the scattering component contributing to the total extinction of a plasmonic metal NP only becomes important for particle sizes well over 50 nm [225], while in the majority of studies much smaller nanostructures are involved. In addition, for the local heating effect to occur effectively, high incident irradiance levels are required, as provided by lasers, powerful solar simulators or light concentrators [226, 227]. Using a standard solar simulator with a maximal output of 1–2 sun(s), or generic 300–500 W Xe sources with optical filters, the temperature rise around plasmonic NPs in aqueous or gaseous media is usually insignificant [228]. Hence, in the majority of cases, this leaves hot electron transfer, near-field enhancement, or an interplay of both as the most likely mechanisms.

The existence of the hot electron transfer mechanisms has been demonstrated by the Beller group [229], as well as our team [230], by means of electron paramagnetic resonance (EPR) studies on traditional noble metal-TiO_2 composite materials. Excitation of the plasmonic composite by a visible light laser resulted in the detection of unpaired electrons associated with the TiO_2 phase, which was not the case when exciting the pristine SC alone. This indicates that the electrons originate from the plasmonic noble metal NP and are transferred to the TiO_2 conduction band.

The existence and influence of the near-field enhancement effect, on the other hand, has been convincingly demonstrated by the pioneering work of Awazu et al., who also introduced the term "plasmonic photocatalysis" for the first time. They used a hybrid plasmonic composite in which Ag@SiO_2 core–shell NPs are deposited on a SiO_2 substrate and subsequently covered by a photocatalytic TiO_2 layer (Fig. 8a) [231]. In this structure, the SiO_2 shell acts as a spacer layer between the plasmonic metal and the SC, which was varied in thickness between 5 and 100 nm. While the insulating nature of the SiO_2 shell inhibits the transfer of (hot) electrons, it was shown that for thin shells, a strong near-field enhancement was achieved, which resulted in the greatest enhancement of the photocatalytic activity, while for SiO_2 shells as thick as 100 nm, the near-field was completely suppressed, and the resulting activity was similar to that of the pristine TiO_2 photocatalyst. The presence of a thin shell may even intensify the near-field relative to bare plasmonic NPs, due to the polarizability of the shell electrons. This polarizability increases with the dielectric constant, favoring most shell materials over air or liquid environments for strong metal-dielectric coupling [232]. The ability of a nanoshell to gradually suppress the near-field enhancement brought about by plasmonic NPs has also been demonstrated both experimentally and theoretically for the case of Ag@polymer core–shell NPs of varying shell thickness [21, 233]. It is shown that for a polymer shell of 3 nm, the near-field enhancement protruding beyond the

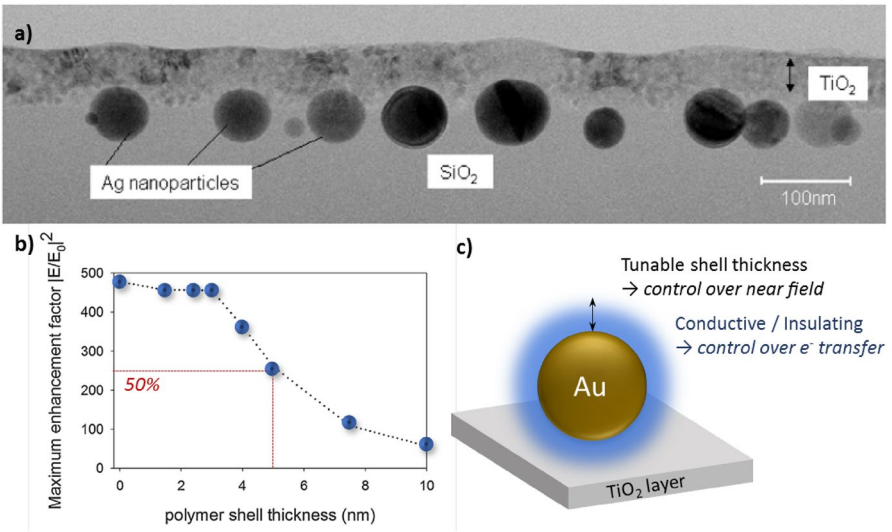

Fig. 8 **a** the plasmonic hybrid TiO_2/Ag@SiO_2/SiO_2 structure used by Awazu et al. **b** Simulated near-field enhancement of Ag@polymer NPs as a function of shell thickness. Adapted with permission **c** schematic representation of the experimental strategy used by Asapu et al. for disentangling hot electron transfer and near-field enhancement effects. Adapted with permission from **a** [231]. Copyright 2008 American Chemical Society, **b** [21]. Copyright 2017 Elsevier

shell is well retained when compared with a bare Ag 18-nm nanosphere, while it is already reduced by 50% for a shell as thin as 5 nm (Fig. 8b).

Inspired by the properties of the core–shell concept described above, Asapu et al. proposed a versatile experimental strategy to disentangle the relative contributions of hot electron transfer and near-field enhancement based on metal@polymer core–shell NPs of which the shell thickness as well as the shell's conductive nature can be tuned (Fig. 8c) [84]. Au@polymer NPs with electrically insulating shells of varying thicknesses were prepared using a controlled layer-by-layer approach, while Au@polymer NPs with electrically conductive shells of varying thickness were prepared using time-dependent in situ polymerization of PANI. Hence, by altering the conductive nature of the shells, the existence of hot electron transfer could be regulated, while the tunability of the shell thickness enabled the extent of near-field enhancement to be controlled. This way, both phenomena could be selectively suppressed or evoked. By corroborating SERS measurements, theoretical field simulations, and photocatalytic activity measurements, it was concluded that for the tested photocatalytic reaction (stearic acid degradation), the near-field enhancement mechanism clearly played a dominant role [84]. However, the strategy has not yet been applied to other photochemical reactions, which may yield a different outcome.

3.2 Applications

3.2.1 H_2 Evolution

An important photocatalytic application of plasmonic NPs is the evolution of green H_2 from water through the hydrogen evolution reaction (HER) (Eqs. 2–3) [234].

$$2H_2O + 4h^+{}_{VB} \rightarrow O_2 + 4H^+ \left(E^0{}_{redox} = 0.82V_{NHE}(\text{vs Normal Hydrogen Electrode})\right) \quad (2)$$

$$2H^+ + 2e^-{}_{CB} \rightarrow H_2 \left(E^0{}_{redox} = -0.41V_{NHE}\right) \quad (3)$$

where E^0 is the standard redox potential.

For this, core–shell structures containing SCs are the most studied class of hybrid plasmonic materials [148]. A comprehensive overview of selected pioneering and recent studies of hybrid HER photocatalysts is given in Table 1, reporting on the reaction conditions, activity, and stability. Unfortunately, an accurate comparison among different studies is hampered, since the experimental conditions (e.g. the light intensity) are often not mentioned in sufficient detail, nor standardized.

Earlier, mostly Au@CdS chalcogenides were investigated due to the small band gap and favorable band edge positions of CdS (Fig. 9). The CB level allows H^+ reduction ($-0.7 < -0.41$ V_{NHE}), while the small band gap (2.4 eV) results in broad overlap with LSPR of Au, leading to efficient use of the near field mechanism, next to hot electron transfer [235]. The H_2 production activity is often further boosted using co-catalysts (e.g. large Ag@SiO_2 antennas [236]) and morphological optimization (e.g. introduction of nanogaps in (AuAg/Ag)@CdS [113], see Sect. 2.2.2).

However, Cd species are notorious for being toxic and susceptible to photocorrosion [116]. Even though it is shown that the Au core may partially prevent the latter by hole scavenging [112], more sustainable alternatives are highly requested. Ha et al. introduced the less toxic Au@Cu_2FeSnS_4, even though these Cu_2FeSnS_4 species still remain relatively unknown [239]. On the contrary, a vast amount of literature exists on more sustainable, stable SCs such as g-C_3N_4 [115, 240] and especially TiO_2 [148, 241, 242]. These are often combined with plasmonic NPs to overcome their low light absorption capabilities due to relatively large band gaps (2.7 and 3.2 eV, respectively). Pioneers for the synthesis of metal@C_3N_4 were Zhu and coworkers [115]. Via their facile reflux treatment of C_3N_4 nanosheets, they produced 10 wt% Ag@C_3N_4 photocatalysts which yielded 30 times higher H_2 evolution rates (~25 µmol g^{-1} h^{-1}) than pure C_3N_4 under Vis light ($\lambda > 420$ nm). Metal@TiO_2 core–shell nanostructures for H_2 evolution are studied even more extensively. They also proved to be superior to catalysts consisting of metal particles simply deposited on the TiO_2 surface [243, 244]. Further morphological optimization within the core–shell structure may enhance the H_2 production rate even more. For example, Au@mesoporous TiO_2 hollow nanosphere core–shell (yolk–shell) structures outperform Au deposited on TiO_2 spheres (69.77 vs. 37.80 mmol g^{-1} h^{-1}). The mesoporous hollow nanospheres facilitate internal multiple light scattering, greatly enhancing the light absorption by Au [244].

Table 1 Recent H_2 evolution studies using plasmonic hybrid nanostructures, given with their reaction conditions, activity, and reaction time, of which at least 90% of its mentioned activity is retained ($t_{>90\%}$)

Photocatalyst	Light (intensity)[a]	Reaction medium (temperature, pressure)[a]	Activity (mmol g^{-1} h^{-1})	$t_{>90\%}$ (h)	References
Nanogap engineered (Au/AgAu)@CdS	Vis (>420 nm, NA)[b]	0.25 M Na_2SO_3 and 0.35 M Na_2S in H_2O (RT)[b]	4.71	24	[113]
Au@CdS	Vis (>420 nm, NA)	0.1 M Na_2SO_3 and 0.1 M Na_2S in H_2O	0.3836	16	[112]
Half-cut Au@CdS	Red light (640 nm, 3.4 mW cm^{-2})	H_2O (25 °C)	~0.08	>200	[255]
$Au_{0.4}Cu_{0.1}/CaIn_2S_4$	450–750 nm (NA)	0.25 M Na_2SO_3 and 0.25 M Na_2S in H_2O; N_2	45.28	8	[253]
$Cu_{0.1}@Au_{0.4}/CaIn_2S_4$	450–750 nm (NA)	0.25 M Na_2SO_3 and 0.25 M Na_2S in H_2O; N_2	20.57	8	[253]
$Au@Cu_2FeSnS_4$	Solar (100 mW cm^{-2})	0.25 M Na_2SO_3 and 0.35 M Na_2S in H_2O	0.090	19	[239]
Au@mesoporous TiO_2 hollow nanospheres	>420 nm (200 mW cm^{-2})	0.1 M ascorbic acid in methanol:H_2O (1:1 v/v)); N_2	69.77	12	[244]
Au NRs @TiO_2 nanodumbbells	Solar (NA)	10 mM $NaHCO_3$ in methanol:H_2O (1:4 v/v); Ar (28–35 °C)	0.0116	NA	[256]
SiO_2@1wt% Au@TiO_2	UV–Vis (NA)	Methanol:H_2O (1:3 v/v)	12	5	[243]
Janus Au-TiO_2	>400 nm (NA)	Isopropanol:H_2O (1:2 v/v); Ar (1 atm)	56	3	[148]
10 wt% Ag@C_3N_4	>420 nm (NA)	20 vol% triethanolamine in H_2O; 2.7 kPa Ar (RT)	~0.025	10	[115]
SiO_2/Ag@TiO_2	Solar (100 mW cm^{-2})	20 vol% glycerol in artificial seawater	0.857	2	[246]
Pt-edged Au triangular nanoprisms	Vis–NIR (>420 nm, NA)	Methanol:H_2O (1:2 v/v); Ar	~1	NA	[245]
Pt-tipped Au NRs	Vis–NIR (460–820 nm, NA)	Methanol:H_2O (1:4 v/v)	~1.96	6	[257]
TiO_2 NTs-Au@Pt	Solar (100 mW cm^{-2})	0.5 M $NaSO_4$ in methanol:H_2O (1:4 v/v); Ar	2.971	15	[247]
TiO_2 NTs-AuPt	Solar (100 mW cm^{-2})	0.5 M $NaSO_4$ in methanol:H_2O (1:4 v/v); Ar	2.18	15	[247]
Homogeneously alloyed AuPt-TiO_2 NTs	Solar (100 mW cm^{-2})	Ethanol:H_2O (1:4 v/v); N_2	12.04 μL h^{-1}[c]	5	[241]

Table 1 (continued)

Photocatalyst	Light (intensity)[a]	Reaction medium (temperature, pressure)[a]	Activity (mmol g^{-1} h^{-1})	$t_{>90\%}$ (h)	References
PtAu/g-C_3N_4	UV–Vis (NA)	0.25 M $NaSO_3$ and 0.25 M Na_2S in H_2O; N_2 (43–45 °C)	1.009	20	[240]
AuPt/Ti^{3+} inverse opal TiO_2	Solar (150 mW cm^{-2})	10% ethanol in H_2O (35 °C)	181.77	6	[242]
0.5 wt% AuPd/g-C_3N_4	>400 nm (35 mW cm^{-2})	10 vol% triethanolamine in H_2O	0.326	6	[258]
Cu_7Co_3 bimetal	Solar (NA)	H_2O, no sacrificial agent	0.0771	24	[254]

[a]If known

[b]NA = not available, RT = room temperature

[c]No catalyst mass mentioned

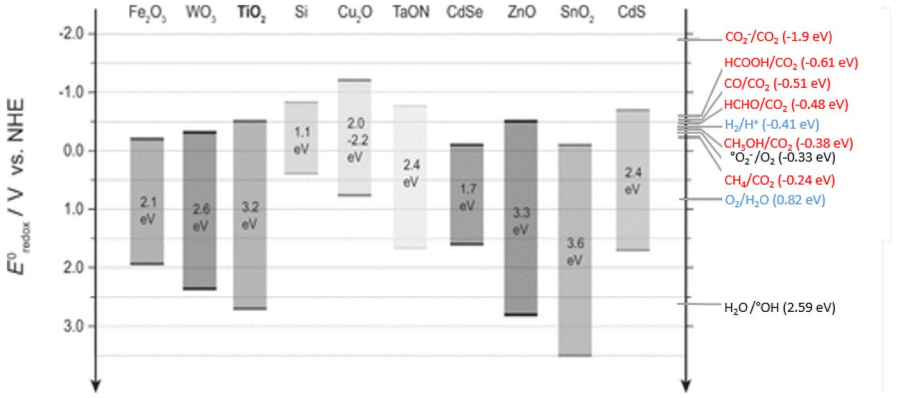

Fig. 9 Band gaps and VB/CB energy levels of common photocatalysts, shown with the relevant redox potentials for water splitting (blue) and CO_2 conversion (red) and ROS generation half reactions (black). Adapted with permission from [235]. Copyright 2013 John Wiley and Sons, Royal Society of Chemistry [237]; Permission conveyed through Copyright Clearance Center, Inc. and [238]

Other studies indicate that Janus metal-SC structures may be more optimal for H_2 production than the core–shell equivalent, due to strongly localized near-fields [148]. Note again that for efficient use of these near-fields, the absorption spectra of both metal and SC should overlap (see Sect. 3.1.1) [4]. Seh et al. synthesized non-centrosymmetric Janus Au-amorphous TiO_2 structures, with a HER activity of 56 mmol g^{-1} h^{-1} under Vis light illumination (irradiance not mentioned). This value was about twice the rate of the core–shell equivalent [148]. Lou et al. also found a fivefold higher H_2 production rate for Pt-edged Au triangular nanoprisms compared with Au triangular nanoprisms completely covered by Pt (0.167 µmol h^{-1} vs. 0.031 µmol h^{-1} under Vis–NIR illumination) [245]. On the other hand, a completely full shell surrounding a metal core is more beneficial for stability purposes, especially when working with harsher water sources such as wastewater or saline seawater [234, 246]. An interesting solution might be the Janus composite of (stable) metal@polymer core–shell particles and a chemostable SC such as TiO_2. Since the strength of the localized fields will be affected by the polymeric shell, accurate shell thickness control is of paramount importance. Hence, the LbL strategy of Asapu et al. (see Sect. 2.2.3) seems promising [21]. In addition, LbL-stabilized Ag and AuAg NPs already proved to be stable in saline media [21, 139].

Finally, as mentioned earlier, water splitting is also feasible with purely metallic photocatalysts. Often Pt is involved in these metal hybrids for its excellent electron sink and H_2 evolution capacity [247], which benefits from its low Fermi level, large work function, and special catalytic sites for H_2 formation. Compared with Pt, Au, Ag and Cu have much weaker metal-H bonding capacity due to the rather high occupancy of anti-bonding 1s hydrogen and d metal states [248]. On the other hand, Pt yields a weaker LSPR signal [249, 250]. Hence, Pt is regularly combined with plasmonic metals such as Au, both as alloys or core–shell structures [245]. Nonetheless, these metal hybrids are often combined with SCs to boost the H_2 generation. Hung et al. claimed the combination of SCs with core–shell Au@Pt to be superior

to an alloy approach due to a better charge separation and migration. They attributed this to an extra electric field caused by the descending Fermi level in the well-defined Au@Pt nanostructure. This facilitated the electron transport towards the reagent [247]. Bian et al. also noticed that their homogeneous AuPt alloys do not show a plasmon band in the Vis range [241]. A study involving MOFs, comparing Pt@MIL-125/Au and Pt/MIL-125/Au, also found that spatial separation between Au and Pt may be beneficial for e^-/h^+ separation. Upon illumination with Vis light, the former yielded H_2 production rates of 1.743 mmol g^{-1} h^{-1}, while the latter with Pt and Au touching at the surface could only achieve 0.161 mmol g^{-1} h^{-1} [251]. For more information about H_2 evolution composites consisting of bimetallic co-catalysts and SCs, the reader is referred to the recent review of Liu et al. [252]. Nowadays, there is also a push to substitute Pt for more abundant metals. Ding et al. therefore proposed the H_2 production potential of AuCu–$CaIn_2S$ [253]. Remarkably, they observed that the photocatalysts containing AuCu alloys outperformed the Au@Cu core–shell equivalents. They attributed the lower activity of the latter to more shielding of the Au and less efficient charge transport [253]. More recently, promising bimetallic CuCo photocatalysts were suggested by Zhang et al., since Co may simultaneously offer a modest H_2 storage property (0.42 wt%) [254].

3.2.2 CO_2 Conversion

Next to photocatalytic H_2 evolution, CO_2 conversion to CO, CH_4, and other valuable carbon compounds are also regarded as a promising route towards solar fuel production. However, due to the inertness of the linear CO_2 molecule, the one-electron reduction to the $CO_2^{-\circ}$ radical anion comes with a significant energy cost. The reduction potential of 1.9 V vs. V_{NHE} exceeds practically all SC CB levels [259]. Therefore, the use of a single SC is in theory excluded for this pathway. Nonetheless, already in the 1970s it was discovered that TiO_2 could catalyze the reduction of CO_2 to C_1 compounds such as formic acid, formaldehyde, methanol, and methane under UV illumination in the presence of water molecules (Eqs. 4–8) [260].

$$2H_2O + 4h^+_{VB} \rightarrow O_2 + 4H^+ \quad E^0_{redox} = -1.23V_{NHE} \tag{4}$$

$$CO_2 + 2H^+ + 2e^- \rightarrow HCOOH \quad E^0_{redox} = -0.61V_{NHE} \tag{5}$$

$$CO_2 + 4H^+ + 4e^- \rightarrow HCHO + H_2O \quad E^0_{redox} = -0.48V_{NHE} \tag{6}$$

$$CO_2 + 6H^+ + 6e^- \rightarrow CH_3OH + H_2O \quad E^0_{redox} = -0.48V_{NHE} \tag{7}$$

$$CO_2 + 8H^+ + 8e^- \rightarrow CH_4 + 2H_2O \quad E^0_{redox} = -0.24V_{NHE} \tag{8}$$

where E^0_{redox} is the standard redox potential.

It should be noted that although these overall proton-assisted conversions are thermodynamically feasible for common photocatalysts such as TiO_2 and CdS (see

Fig. 10), the real mechanisms are not fully elucidated. Nevertheless, it is shown that metallic plasmonic photocatalysts are able to facilitate the CO_2 radicalization rate determining step via the mechanisms described in Sect. 3.1.1. Note that the photothermal effect may also drive these reactions. Since this is not exclusively "photocatalysis,", the interested reader is referred to the recent review of Verma et al. [259]. Jain et al. showed the presence of hot electron transfer to radicalize CO_2 for PVP-coated Au NPs, though the activity was still moderate (< 1 NP^{-1} h^{-1}) [132]. This activity can be further improved by modifying the reaction medium (e.g. the use of ionic liquids to stabilize the transition state) [261]. Another interesting option is the further hybridization of the plasmonic photocatalyst. Hybrid composites of plasmonic Au [262, 263], Ag [86, 264], and Cu [94] (for Vis light absorption) and more active catalytic metals such as Pt [265], Pd [262], and Ni [266] are reported in the literature, mostly as metal cores with SC shells.

Hong et al. demonstrated the superiority of the Ag@TiO_2 core–shell configuration over conventional Ag deposited on TiO_2 (4.9 vs. 1.5 µmol CH_4 g^{-1} h^{-1} under AM (Air Mass) 1.5 simulated sunlight) [86]. Similar observations were made for Au@TiO_2 core–shell structures vs. Au deposited on TiO_2 [85]. Pougin et al. furthermore optimized the TiO_2 shell thickness for Au@TiO_2-Au. They revealed 20-nm shells as the most optimal for 20-nm Au core nanospheres, due to a better developed TiO_2 crystal structure (1.4 µmol CH_4 g^{-1} h^{-1} vs. 0.7 (11 nm) and 0.4 (8 nm) µmol CH_4 g^{-1} h^{-1} under UV–Vis illumination) [85]. On the other hand, the increased activity with increasing shell thickness is not a universal trend for all SCs and Au core sizes. Wei et al., for example, showed that for 3.5-nm Au nanosphere cores, the thinner CdS shells (maximal molar CdS-to-Au ratio of 1) were superior for CH_4 production in terms of activity (41 µmol g^{-1} h^{-1} under UV–Vis illumination) and selectivity (98.6%) [263]. Bera et al. further studied the optimal size of a spherical Au core in a Au@SiO_2/Pt/TiO_2 catalyst [265]. In a 4–26-nm diameter range, 18 nm appeared to yield the highest CH_4 production activity (2.98 µmol g^{-1} h^{-1} under

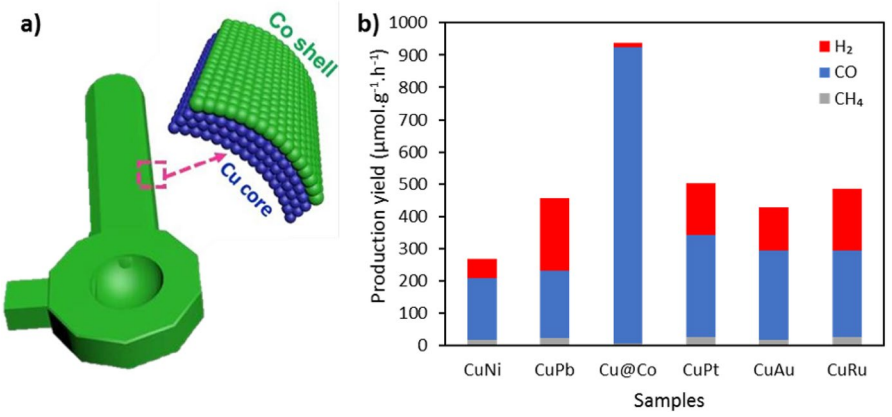

Fig. 10 **a** Dagger-axe-like Cu@Co core–shell photocatalyst, with **b** its production yields for CH_4 (grey), CO (blue), and H_2 (red) after UV–Vis illumination (150 mW cm^{-2}), compared with those for other bimetallic alloys. Adapted with permission from [94]. Copyright 2021 Elsevier

530 nm and 365 nm co-irradiation, for a SiO_2 shell of 8–10 nm) [265]. Next to CH_4, CO may be targeted as well (Eq. 9).

$$CO_2 + 2H^+ + 2e^- \rightarrow CO + H_2O \quad E^0{}_{redox} = -0.53V_{NHE} \tag{9}$$

where $E^0{}_{redox}$ is the standard redox potential.

Recently, dagger-axe-like Cu@Co core–shell photocatalysts were designed (Fig. 10a), yielding stable rates of 920 µmol CO g^{-1} h^{-1} with a CO selectivity of 98% under UV–Vis illumination (150 mW cm^{-2}). The activity exceeded the rates for CuCo (741 µmol CO g^{-1} h^{-1}) and other alloys (Cu@Co > CuCo > CuPt > CuAu > CuRu > CuPb > CuNi) (Fig. 10b). This was attributed to enhanced CO_2 adsorption and better charge separation and migration. Remarkably, considerable amounts of CH_4 and especially H_2 were formed for the other alloys (up to ~ 50% for CuPb) [94]. Both may be regarded as unwanted here. For instance, H_2 formation reduces the number of protons which are needed for the proton-assisted formation of CO (Eq. 9). Pt is both a good catalyst for H_2 evolution (see Sect. 3.2.1), but also for CO_2 conversion [248]. To ensure selectivity towards CH_4, Zhai et al. applied Cu_2O shells, leading to more than doubling of the CH_4 selectivity to 85%. In addition, alloying with Cu aiming at high-indexed facets may also improve CH_4 selectivity. Lang et al. revealed that the (730) facets of PtCu concave nanocubes loaded on C_3N_4 nanosheets had more low-coordinated active sites, compared with (100) facets. This increased the CO_2 adsorption and activation [267]. Note that the selectivity towards CO or CH_4 can also be adjusted by changing or adding a metal [194]. A good example of this is the study of Han et al. [269]. They demonstrated that their Au@Pd@MOF-74 photocatalyst with a selectivity of ~ 100% for CO, produced CH_4 with a selectivity of 84% after addition of Pt on the outer shell [269].

On the other hand, H_2 can be used as a reagent, instead of water, in the reverse water gas shift (rWGS) reaction in order to generate CO from CO_2 (Eq. 10).

$$CO_2 + H_2 \rightarrow CO + H_2O \tag{10}$$

Halas's group rationally designed Al@Cu_2O antenna-reactor NPs (see Sect. 2.2.1) [270]. These systems, based on sustainable, broadly absorbing Al, yielded external quantum efficiencies of 0.35%, exceeding hybrid Ag [264] and Au systems [270]. Furthermore, outstanding CO selectivity (> 99%) was achieved at low temperature and high light intensity (up to 10 W cm^{-2}), greatly exceeding the values attained by the thermally driven rWGS (50–97%) [270]. Finally, CH_4 can also be used as reductant for CO_2. This process is better known as dry reforming of methane (DRM) and produces syngas (Eq. 11).

$$CO_2 + CH_4 \rightarrow 2CO + 2H_2 \tag{11}$$

For years, this reaction has been performed at temperatures of 800–1000 °C [259]. Liu et al. opened up this photocatalytic application by observing DRM activity by plasmonic Au catalysts under Vis light irradiation and lower temperature (500 °C) [271]. Later, they also introduced real hybrid examples such as PdAu alloys [272]. Recently, Zhou et al. proposed bimetallic CuRu as plasmonic antenna–single-site reactor systems, able to operate at room temperature. Under 19.2 W cm^{-2}

white light illumination, these photocatalysts converted CH_4 with rates exceeding 200 µmol g^{-1} s^{-1}, producing syngas with an excellent selectivity (> 99%) and stability (50 h). Proper alloying is of paramount importance here, since the presence of single Ru atoms leads to less coking and less rWGS, and decreases the activation barriers [273]. The required high intensities of both rWGS and DRM are also a drawback of this process. They are about two orders of magnitude higher than for conventional CO_2 photoreductions with H_2O. In Table 2, the reported reaction conditions (reagents, intensities, etc.) are summarized, together with the achieved activity, selectivity, and stability for several recent CO_2 reduction studies. An accurate mutual comparison remains difficult here as well for the same reason as for water splitting.

3.2.3 Pollutant Degradation

Degradation of air- and water-based pollutants is one of the most widely studied subjects within photocatalysis. Air pollution abatement studies often focus on simple inorganic (e.g. NO_x and SO_x) or volatile organic compounds (VOCs) (e.g. formaldehyde). Water-based research, on the other hand, mostly deals with more complex compounds such as dyes, pharmaceuticals, and pesticides [9]. The mechanism for photocatalytic degradation of pollutants in air and water is driven by ROS. Species such as superoxide anion and hydroxyl radicals are generated by the redox reactions of oxygen and water with e^-_{CB} and h^+_{VB} (Eqs. 12, 13) [4, 238]. These ROS can oxidize pollutants due to their high redox potentials (Fig. 9).

$$O_{2g} + e^-_{CB} \rightarrow {}^{o} \quad O_2^-(E^0_{redox} = -0.33V_{NHE} \tag{12}$$

$$H_2O + h^+_{VB} \rightarrow {}^{o} \quad OH + H^+(E^0_{redox} = 2.59V_{NHE}) \tag{13}$$

3.2.3.1 Water Purification Dye degradation is the most widely studied application in photocatalytic water purification. However, a major point of attention in this regard, which is regrettably often overlooked, is that such compounds may themselves act as photosensitizers, possibly leading to confounding results [274]. Hence, careful setup and control experiments are required [9]. Alternatively, Vis-transparent molecules such as phenol or naphtol can be used. Mostly SCs modified with multi-metal core–shell [275–279] or alloys [280–282, 284–286] (Au, Ag, Cu, Pd, Co, Ni etc.) have been investigated. For the degradation of phenol, core–shell Au@Pd deposited on TiO_2 yielded 5.4 times faster phenol degradation under Vis light ($\lambda > 420$ nm) than the alloy on TiO_2 (3.8 µM min^{-1} vs. 0.7 µM min^{-1}). It was claimed that Pd at the surface was more favorable due to its stronger ability to generate charge carriers, relative to Au [280]. Furthermore, it is even suggested that for some SCs (such as narrow-band-gap SCs), Janus configurations may be more beneficial. For example, Janus Au-SnS_2 (2.1–2.4 eV) displays the highest apparent reaction rates (k_{app}) for the degradation of methyl orange under Vis light (0.240 min^{-1} vs. 0.072 min^{-1} for core–shell Au@SnS_2 and 0.060 min^{-1} for sole SnS_2 for suspensions containing 0.625 g L^{-1}). This can be

Table 2 Several recent CO_2 conversion studies using plasmonic hybrid nanostructures, given with their reaction conditions, activity, selectivity, and reaction time of which at least 90% of its mentioned activity is retained ($t_{>90\%}$)

Photocatalyst	Light (intensity)[a]	Reaction medium (temperature, pressure)[a]	Activity (species) (μmol g^{-1} h)	Selectivity (species) (%)	$t_{>90\%}$ (h)	References
Ag@TiO_2	Solar (NA[b])	CO_2 and H_2O vapor (0.5%) (25 °C)	4.9 (CH_4)	> 94 (CH_4)	3	[86]
Au@TiO_2 (20 nm)-Au	UV–Vis (NA)	1.5% CO_2 and 0.6% H_2O in ultrapure He (5 °C, 0.15 MPa)	~0.83 (CH_4) ~0.69 (CO) ~10 (H_2)	~8 (CH_4) ~7 (CO) ~85 (H_2)	6	[85]
Au@TiO_2 (20 nm)	UV–Vis (NA)	1.5% CO_2 and 0.6% H_2O in ultrapure He (5 °C, 0.15 MPa)	~0.30 (CH_4) ~0.32 (CO) ~10 (H_2)	~3 (CH_4) ~4 (CO) ~93 (H_2)	2	[85]
Inverse opal TiO_2-supported Au@CdS	UV–Vis (320–780 nm, 100 mW cm^{-2})	99.999% CO_2 passed through H_2O bubbler (25 °C, 0.1 MPa)	41.6 (CH_4)	98.6 (CH_4)	2	[263]
Pt/TiO_2/Au (18 nm)@SiO_2	365 nm + 530 nm (NA)	H_2O saturated CO_2 (0.1040 MPa)	3.0 (CH_4)	NA	2	[265]
Ag@Re_n-MOF	Vis (400–700 nm, NA)	Trimethylamine:acetonitrile (1:20) and CO_2 (0.1013 MPa)	~163[c] (CO)	NA	50	[264]
Hierarchical urchin-like yolk@ $TiO_{2-x}H_x$ shell decorated with core–shell Au@Pd	UV–Vis (NA)	99.9% CO_2 bubbled through H_2O (15 °C)	18 (CH_4)	94 (CH_4)	7	[262]
Dagger-axe-like Cu@Co	UV–Vis (150 mW cm^{-2})	H_2O:lactic acid (2:1) and CO_2 (RT[b], 0.1013 MPa)	920 (CO)	98 (CO)	12	[94]
CuCo alloy	UV–Vis (150 mW cm^{-2})	H_2O:lactic acid (2:1) and CO_2 (RT, 0.1013 MPa)	741 (CO)	90 (CO)	12	[94]
CuNi alloy	UV–Vis (150 mW cm^{-2})	H_2O:lactic acid (2:1) and CO_2 (RT, 0.1013 MPa)	~187 (CO)	~69 (CO)	12	[94]
CuPb alloy	UV–Vis (150 mW cm^{-2})	H_2O:lactic acid (2:1) and CO_2 (RT, 0.1013 MPa)	~243 (CO)	~53 (CO)	12	[94]

Table 2 (continued)

Photocatalyst	Light (intensity)[a]	Reaction medium (temperature, pressure)[a]	Activity (species) (μmol g^{-1} h)	Selectivity (species) (%)	$t_{>90\%}$ (h)	References
CuPt alloy	UV–Vis (150 mW cm^{-2})	H_2O:lactic acid (2:1) and CO_2 (RT, 0.1013 MPa)	~290 (CO)	~57 (CO)	12	[94]
CuAu alloy	UV–Vis (150 mW cm^{-2})	H_2O:lactic acid (2:1) and CO_2 (RT, 0.1013 MPa)	~280 (CO)	~65 (CO)	12	[94]
CuRu alloy	UV–Vis (150 mW cm^{-2})	H_2O:lactic acid (2:1) and CO_2 (RT, 0.1013 MPa)	~262 (CO)	~54 (CO)	12	[94]
Au@Pd@MOF-74	UV–Vis (NA)	800 ppm CO_2, sprayed H_2O in N_2	2.5 (CO)	~100 (CO)	5	[269]
Pt/Au@Pd@MOF-74	UV–Vis (NA)	800 ppm CO_2, sprayed H_2O in N_2	2.5 (CH_4) 0.5 (CO)	84 (CH_4) 16 (CO)	5	[269]
Al@Cu_2O	UV–Vis (400–850 nm, 10 W cm^{-2})	10 sccm CO_2:H_2 (1:1) (no external heating, ~ 155°C[d])	360 μmol $cm^{-2}h^{-1}$ (CO)	99.3 (CO)	0.28	[270]
NiAu/SiO_2	Green light (520 nm, 68.4 W cm^{-2})	CO_2:H_2:N_2 (1:4:1) (450 °C)	34% CO_2 conversion	77 (CH_4)	NA	[266]
AuCu/TiO_2	Solar (1 W cm^{-2})	CO_2 bubbled through water (RT-60 °C, 1.9 atm)	2200 (CH_4)	97 (CH_4)	6	[268]
PtCu concave nanocubes with (730) high-index facets/C_3N_4	UV–Vis (100 mW cm^{-2})	CO_2 (0.15 MPa)	7.47 (CH_4)	90.6 (CH_4)	4	[267]
$Pd_{90}Au_{10}/Al_2O_3$	Vis (0.21 W cm^{-2})	20 mL min^{-1} CO_2:CH_4 (1:1)	~32×10^3 (CH_4) ~48×10^3 (CO)	~100 (syngas)	3	[272]
$Cu_{19,9}Ru_{0,1}$	White light (19.2 W cm^{-2})	8 sccm CH_4, 8 sccm CO_2 (RT)	~0.78×10^6 (CH_4)	>99 (syngas)	>50	[273]

[a]If known

[b]NA = not available, RT = room temperature

[c]Based on Re weight

[d]Temperature because of high-intensity irradiation, no additional heating

explained by an increase in Vis light extinction, while the red shift experienced by core–shell NPs is so large (> 100 nm) that the absorption maximum reaches the NIR spectral region [287]. On the other hand, alloying may still yield superior results relative to combined deposition of separate monometallic plasmonic NPs. Zielińska-Jurek et al. found phenol degradation rates of 3.54 μM min^{-1} for $Au_{0.5}Ag_{1.5}$ on TiO_2 under Vis light illumination ($\lambda > 450$ nm) while comparable Au and Ag samples yielded significantly lower rates (0.35 and 1.26 μM min^{-1}, respectively). Hence, they underlined the necessity of contact between the metals for efficient charge separation [282]. Nevertheless, the authors also observed that the dominant Ag species is Ag_2O [282]. Working in an aqueous environment raises important stability issues regarding corrosion and dissolution [9]. The latter will be discussed more in detail in Sect. 3.2.4. To increase the stability, several solutions have emerged. For instance, embedment in Ag halide yielded stable AuAg@AgBr photocatalysts [288]. The material roughly retained its initial 2-naphtol degradation activity (100% degradation after 15 min of illumination with Vis light ($\lambda > 420$ nm), for a starting concentration of 10 μM and a catalyst loading of 1 g L^{-1}) after five consecutive reaction cycles. No signs of Ag^+ or Br^- leaching were detected with ion chromatography and inductively coupled plasma spectroscopy [288]. Another interesting option to stabilize the NPs can be found in the field of aerobic oxidation. Sugano et al. showed that oxidized Cu in AuCu alloys could be regenerated by Au, as confirmed by EPR spectroscopy. Requirements for this are an e^- donor (e.g. alcohols) and a sufficiently high Au content, e.g. $Au_{0.7}Cu_{0.3}$ [289].

Another challenge associated with photocatalytic water purification using suspended particles systems is catalyst recycling. As a solution, the introduction of magnetic shells has been proposed for facile post-recovery. Reduced graphene oxide (rGO) modified with Au@magnetic Ni lost less than 17% of its initial activity in the sunlight driven degradation of phenol after five consecutive cycles. In addition, this loss was mostly attributed to a loss of surface sites [276]. Similar results were obtained for Ag/AgBr@Fe_2O_3 for methyl orange degradation [290]. However, magnetic oxides tend to be unstable, especially in acidic waste waters [277]. Therefore, Su et al. developed triple-shelled Ag@Fe_3O_4@SiO_2@TiO_2 photocatalysts. The extra inert SiO_2 layer inhibited the e^-/h^+ transfer from TiO_2 to Fe_3O_4 and avoided strong Fabry–Perot oscillations [277]. Note furthermore that due to this interlayer the transfer of hot electrons is prevented (see Sect. 3.1), which is often considered the dominant plasmonic effect in plasmon-enhanced photocatalytic water purification [275, 291]. On the other hand, the near-field enhancement mechanism benefits from the higher refractive index of the iron oxide (2.42) [277]. Other solutions include the fixation of the catalyst onto membranes [292] or even water-floatable structures [293]. Recently, Kaur et al. successfully applied the latter concept by incorporating Cr-doped TiO_2 modified with plasmonic TiN@SiO_2 core–shell NPs on highly solar transparent and water permeable alginate networks. These floatable networks, mimicking natural Marimo algae, allowed a 3.3-fold enhanced methylene blue (MB) degradation activity under 1 sun solar light (k_{app} of 0.30 min^{-1} vs. 0.09 min^{-1} for the non-plasmonic equivalent, 2 g catalyst L^{-1}) [293].

Bathla et al. pointed out the superiority of core–shell nanostructures over alloys for multiple reasons, including an accelerated interfacial charge transfer and

synergistic adsorption and the photocatalytic effects of certain atomic groups at the surface [294]. Nonetheless, complete mineralization often remains difficult for plasmon-enhanced photocatalysts [9]. A final water pollutant class consists of inorganic ions (e.g. As, Cr species). By appropriately choosing the metal and SC (with sufficiently energetic CB), simultaneous oxidation of organic pollutants and reduction of inorganic contaminants is possible [277]. This concurrent oxidation is often necessary. The less toxic Cr(III) tends to quickly re-oxidize if the h^+ are not effectively scavenged [295]. Patnaik et al. observed an increased Cr(VI) removal after adding 20 mg L^{-1} phenol. The Cr(VI) conversion after 2 h of UV–Vis illumination for their alloyed AuPd on g-C_3N_4 photocatalysts (1 g L^{-1}) increased from 64 to 91.6% [285]. Rationally designed plasmonic hybrids could further circumvent this issue due to their good charge separation. Metal@SC Janus NPs, where the metal functions as an electron sink and the redox reactions take place at different locations, would thus be interesting in that regard. Unfortunately, actual plasmonic Janus NPs studies for Cr(VI) removal are still lacking to date.

Lastly, it is noteworthy that hybrid plasmonic NPs are also gradually being applied for other main classes of water pollutants such as persistent pesticides [281, 296], endocrine-disrupting chemicals [290], pharmaceuticals, or other contaminants of emerging concern (CECs) [292, 297]. Table 3 displays a summary of selected exemplary plasmonic hybrid studies on both CECs and less persistent compounds. A true comparison also remains difficult here due to the lack of standardization.

3.2.3.2 Air Purification Important reactions in the domain of air purification are the degradation of VOCs (e.g. benzene, formaldehyde), CO oxidation, and conversion of inorganic gaseous molecules such as NO_x and SO_x. The foremost majority of metal-modified SC-based air purification studies make use of binary or ternary composites of metal NPs deposited on the SC surface, with the aim of reducing charge carrier recombination. As mentioned above, the use of single plasmonic NPs in environmental remediation is not in the scope of the present overview, but is discussed thoroughly in the review of Wang et al. [9]. The rest of this subsection will again focus on studies involving more complex, hybrid materials.

A major difference with liquid pollutant research is that air purification studies more often make use of continuous flow systems dealing with low concentrations. This results in low residence times and underlines the importance of a large surface area [300]. Hence, in VOC removal studies, high-surface area substrates such as graphene oxide (GO), rGO, MOFs, and zeolites are modified with single plasmon NPs and SCs, forming binary or ternary heterostructures [301–303]. In the past decade, true plasmonic hybrids also entered the field, often in combination with sensing purposes [304, 305]. For example, Wang et al. developed Janus Au nanorod@ZnO@ZIF-8 formaldehyde detectors [304]. Because of the ZIF-8, these structures achieved a surface area up to 924 m^2 g^{-1}. They also noticed a continuous stream of nontoxic formic acid upon Vis light irradiation, pointing out its detection and removal potential. Au@SnO_2 core–shell configurations were shown to be promising for acetaldehyde detection and removal as well [305]. For the latter, Zeng et al. constructed 2-µm Ag NW@TiO_2 core–shell catalysts. These were able to degrade 72% of the initial 500 ppm acetaldehyde in a contact time of only 4.8 min under 20

Table 3 Several recent water pollution abatement studies using plasmonic hybrid nanostructures, given with their reaction conditions and apparent rate constant (k_{app})

Photocatalyst	Light (intensity)[a]	Reaction medium (temperature, pH)[a]	k_{app} [h^{-1}]	Ref
$Co_{1.7}Pd/BiVO_3$	Vis (≥400 nm, NA)	0.2 mM phenol; 0.8 mg catalyst mL^{-1} (RT)	50.2[b1]	[298]
AuPd/mesoporous silica modified g-C_3N_4	UV–Vis (NA)	10 mg $Cr^{VI}L^{-1}$; 20 mg phenol L^{-1}; 1 mg catalyst mL^{-1} (pH 5.7)	0.528 (Cr)[b2] 1.074 (phenol)[b2]	[285]
AuPd/rGO	Natural sunlight (NA)	0.5 mM phenol; 0.5 mg catalyst mL^{-1}(pH 6)	0.576[b2]	[299]
AuPd/Amberlyst® resin	Vis (400–700 nm, NA)	10 ppm parathion, 25 mg catalyst mL^{-1} (20 °C)	~1.14	[296]
AuPd/TiO_2 film	UV (365 nm, 0.4 mW cm^{-2})	10 mg malathion.L^{-1}	0.948[b1]	[281]
AuCu/TiO_2/reduced graphene oxide	UV–Vis (380 – 697 nm, NA)	0.5 mM 2-nitrophenol; 0.3 mg catalyst L^{-1} (pH 6.8)	~1.2[b2,c]	[286]
1.5 wt% $Au_{0.1}Ag_{0.9}/TiO_2$ on CA	Vis (>420 nm, NA)	5 mg tetracycline L^{-1}; 0.05 MPa transmembrane pressure (25 °C)	0.7656[b2]	[292]
Au@Ag/TNT	Simulated sunlight (100 mW cm^{-2})	8 mM MB; 0.33 mg catalyst mL^{-1}	1.746[b2]	[275]
Au@Ni/rGO	Natural sunlight (0.75–0.85 mW cm^{-2})	0.08 mM phenol; 1 mg catalyst mL^{-1} (pH 7)	0.4173[b2]	[276]
Au@Pd/TiO_2	UV–Vis (62 mW cm^{-2} for 310–380 nm range)	0.21 mM phenol; 5 mg catalyst mL^{-1}	~0.714[b2]	[280]
Ag/AgBr@Fe_2O_3	Vis (>420 nm, NA)	10 mg bisphenol A L^{-1}; 1 mg catalyst mL^{-1} (30 °C)	~0.35[b1]	[290]
TiN@SiO_2@Cr-TiO_2 embedded in Ca-alginate beads	Simulated sunlight (100 mW cm^{-2})	0.01 mM MB; 2 mg catalyst mL^{-1}	18[b2]	[293]
Au@SnS_2	Vis (400–780 nm, NA)	40 mg MO L^{-1}; 0.625 mg catalyst L^{-1} (RT)	4.32[b2]	[287]
Janus Au-SnS_2	Vis (400–780 nm, NA)	40 mg MO L^{-1}; 0.625 mg catalyst L^{-1} (RT)	14.4[b2]	[287]

[a]If known

[b1]Concentrations measured by high-pressure liquid chromatography (HPLC) or[b2] colorimetric means

[c]After normalization for prior adsorption phase

mW cm^{-2} 260 W fluorescent light irradiation. The photocatalysts remained stable for 15 weeks and greatly outperformed pristine TiO_2 (37%) [300]. Further boosting of metal@SC structures has been done by extra modification of the SC shell. Gao et al. incorporated Pd atoms in the ceria lattice of Ag@CeO_2 NPs, thereby increasing the oxygen dissociative adsorption capacity and the number of oxygen vacancies. Together with the LSPR effect and good charge separation efficiencies, these structures yielded toluene removal rates of ~ 50% under Vis light at 89 °C (500 ppm, 160 mW cm^{-2}, 0.1 g catalyst). This value was about ten times the activity for bare Ag@CeO_2 NPs at the same reaction temperature [306]. Also, active photocatalysts can be designed without crystalline SCs. The Ag@C systems of Sun et al. were found to be superior to N-doped TiO_2 for the degradation of acetaldehyde (89% vs. 31% under Vis light, 0.1 g catalyst) [307]. Alloys, finally, are less studied than their core–shell equivalents. Wysocka et al. studied different alloys (CuAg, AgPt, CuPt) on TiO_2 for the degradation of toluene under 460-nm light-emitting diode (LED) light. The synergistic effect of Pt was pointed out here, improving the interfacial charge transfer. Hence, higher toluene degradation rates were achieved (rate constants of 2.60 and 2.15 min^{-1} for AgPt- and CuPt-TiO_2, respectively, vs. 0.79 min^{-1} for CuAg-Pt) [308].

The photocatalytic degradation of VOCs such as toluene is generally not a selective process, and may yield a variety of by-products, from various oxidized benzene derivatives to smaller aldehydes [308]. Several of these may be toxic, although by rational design of the hybrid structure, such compounds may be eliminated. The addition of Pd on TiO_2 surfaces may for instance remove surface –OH groups. This promotes the activation of oxygen to °OH radicals. In the toluene degradation reaction, these directly attack the methyl group, avoiding the formation of toxic methylphenolic compounds [309]. Another issue is the formation of CO which may poison the catalysts, especially when Pt particles are involved. High electron densities favor strong binding of CO to the metal [310]. In electrocatalysis, single Pt atom PtCu alloys with a cationic nature are hence applied [311]. Also, plasmon-induced heating, leading to the decomposition of surface carbonates may be helpful, but these often require intensities on the order of W cm^2 [312]. Still, Li et al. managed to design efficient antenna-reactor complexes consisting of Ag@SiO_2/Pt core–shell/satellite configurations for the selective oxidation of CO. High quantum yields of 7–10% for Vis light were reported for intermediate size Ag antennas. Twenty-five-nanometer Ag cores proved to be the most optimal trade-off between near-field enhancement on the Pt surface, scattering and absorption by Ag [313].

An important inorganic pollutant is NO, leading to smog, acid rain, and health issues. For its removal, the use of non-noble plasmonic Bi has recently been investigated. This low-cost semimetal has a work function of 4.22–4.25 eV [314]. Therefore, it can effectively inject electrons in the CB of most SCs. To protect the relatively large Bi cores (100–200 nm), Chen et al. applied 5-nm amorphous Bi_2O_3 shells. These systems yielded a maximal NO removal efficiency of 26.4% using a Xe light source (400 ppb, 0.1 g catalyst) [315]. The use of amorphous layers, on the other hand, may also introduce recombination centers [316]. Thus, Zhang et al. transformed this shell into a crystalline $Bi_2O_2CO_3$ shell by a facile secondary hydrothermal treatment. The NO removal efficiency upon 28.5 mW cm^{-2} UV–Vis light

irradiation increased from 12.3% for Bi@Bi_2O_3 to 34.1% for Bi@$Bi_2O_2CO_3$ NPs due to the lower hot electron transfer resistance [316]. Similar activities are noticed for Bi shells, considering the amount of photocatalyst (0.2 g). Bi_4MoO_9@Bi systems attained 55.4% NO removal due to the LSPR effect of Bi and the oxygen vacancies (OVs) in the SC. Bi and the OVs also display a synergistic effect to prevent the formation of toxic NO_2 dimers (N_2O_4) (Eq. 14) [317].

$$2NO + O_2 \leftrightarrow N_2O_4 \tag{14}$$

The enhanced ROS formation from O_2 by the LSPR effect of Bi and the direct oxidation of NO by h^+, together with the reaction of O_2 with the OVs, avoids the formation of N_2O_4, as shown by in situ diffuse reflectance Fourier transform infrared spectroscopy. Finally, the bismuth oxides can also be used as substrates for Ag@AgCl NPs, showing again similar removal rates (~50% for 0.2 g catalyst) [318]. These values can be compared due to a similar setup. A broader comparison between studies can be found in Table 4. However, due to the frequent lacking of reported intensity data, a true mutual comparison is again hampered.

An interesting final example of air pollution abatement by plasmonic hybrids is the degradation of SF_6 by Mg@MgO core–shell catalysts [319]. SF_6 is a greenhouse gas with a global warming potential of 24,000 times that of CO_2. Plasmonic Mg@MgO can degrade this compound to both MgF_2 and $MgSO_4$. Fascinatingly, the final product is determined by the LSPR effect (Fig. 11a). For Mg with a diameter of 30 nm, LSPR is induced by highly energetic illumination (UV, > 3 eV). The generated free electrons are then tunneled to SF_6. This well-known electron scavenger dissociates subsequently in SF_5 and F radicals (Eq. 15)

$$SF_6 + e^- \rightarrow {}^oSF_5 + F^- \tag{15}$$

The former may undergo a cascade dissociation reaction, yielding S. F^- reacts at the Mg/MgO surface, forming MgF_2 and MgO_xF_y (Fig. 11b). For Mg nanostructures with a diameter of 50–100 nm, photons with a lower energy content of 1.5–2 eV are able to induce LSPR. Hence, SF_4 and SF_2 radicals are formed which can react with moisture and O- or OH-sites on MgO, leading to SO_2. The latter adsorbs on acidic Mg^{2+} sites producing $MgSO_3$. This compound is further oxidized to $MgSO_4$ (Fig. 11c). This wavelength dependence was verified by using different light sources for Mg nanostructures with different LSPR maxima, showing that for hybrids with LSPR at 4.7 eV under UV light (160–400 nm, 3.1–7.75 eV) MgF_2 was the dominant product. On the contrary, for structures with LSPR at 1.9 eV (652 nm) $MgSO_4$ was the main product under 1.95 eV (633 nm) laser irradiation (Fig. 11d). Finally, the Mg species could be regenerated in a few seconds using a hydrogen plasma afterglow process at room temperature [319].

Due to the ability of photocatalytic materials to degrade pollutants, coating them on walls is a facile means of simultaneously purifying the air and keeping the walls clean, in particular, in combination with the superhydrophilic properties of SCs such as TiO_2. Such surfaces can be called self-cleaning surfaces. The photocatalytic coating can be applied on ceramics and glass as well as fabrics. Verbruggen et al. investigated the use of TiO_2 modified with Au_xAg_{1-x} alloy NPs [59, 128, 139]. By applying

Table 4 Several recent air purification studies using plasmonic hybrid nanostructures, given with their reaction conditions and attained pollutant conversion (with the time needed to achieve these values)

Photocatalyst	Light (intensity) [a]	Reaction medium	Conversion [%] (time needed)	Ref
0.5 wt.% Ag NW@TiO_2	UV–Vis (20 mW cm^{-2})	500 ppm CH_3CHO; 20 mL min^{-1}, 0.1 g catalyst,	72[b1] (~ 120 min)	[300]
Ag@C	Vis (> 420 nm, NA)	100 ppm CH_3CHO; N_2; 0.1 g catalyst	89[b1] (65 min)	[307]
Au@SnO_2 on ceramic foam	UV (365 nm, NA)	500 ppm CH_3CHO	~ 100[b1] (~ 120 min)	[305]
Au@truncated wedge-shaped TiO_2	Vis (NA)	100 ppm CH_3CHO; air; 250 mL min^1; RH of 60%; 0.05 g catalyst; 25 °C	~ 91[b1] (210 min)	[321]
CuNi NWs-TiO_2	Vis (NA)	500 ppm CH_3CHO; 20 mL min^{-1}; total volume of 0.3 L; 0.1 g catalyst	56[b1] (~ 75 min)	[322]
Ag@CeO_2 with Pd incorporated in the shell lattice	Vis (400–800 nm, 160 mW cm^{-2})	500 ppm toluene; 20% O_2; N_2; 33.3 mL min^{-1}; 0.1 g catalyst; 89 °C	50[b1] (NA)	[306]
Ag@CeO_2	Vis (400–800 nm, 160 mW cm^{-2})	500 ppm toluene; 20% O_2; N_2; 33.3 mL min^{-1}; 0.1 g catalyst; 89 °C	< 5[b1] (NA)	[306]
Au/hedgehog-shaped TiO_2 microspheres@CuO	Vis (490–760 nm, NA)	0.3 vol% CO; 0.3 vol% O_2; He; 100 mL min^{-1}; 0.5 g catalyst	~ 80[b1] (NA)	[323]
Bi@amorphous Bi_2O_3	(300 W Xe light, no filter)	400 ppb NO; air; 3 L min^{-1}; total volume of 4.5 L; 0.1 g catalyst	26.4[b2] (~ 10 min)	[315]
Bi@crystalline $Bi_2O_2CO_3$	Vis (28.5 mW cm^2)	400 ppb NO; air; 3 L min^{-1}; total volume of 4.5 L; RH[c] of 25%; 0.1 g catalyst; 25 °C	34.1[b2] (~ 30 min)	[316]
Bi_4MoO_9@Bi	Vis (> 420 nm, NA)	550 ppb NO; air; RH[c] of 55%; 2.415 mL min^{-1}; total volume of 4.5 L; 0.2 g catalyst	55.4[b2] (NA)	[324]
Ag/AgCl on $La(OH)_3$	Vis (> 420 nm, 0.16 W cm^{-2})	550 ppb NO; air; 2.415 L min^{-1}; total volume of 4.5 L; 0.1 g catalyst	55% (~ 30 min)	[325]
Ag/AgCl on BiOCl/$Bi_{12}O_{17}Cl_2$	Vis (> 420 nm, NA)	500 ppb NO; air; RH[c] of 55%; 2.4 L min^{-1}; total volume of 4.5 L; 0.2 g catalyst	49.5[b2] (~ 30 min)	[318]

[a]If known

[b1]Concentrations measured by GC or [b2]Chemiluminescent NO_x analyzer

[c]RH = relative humidity

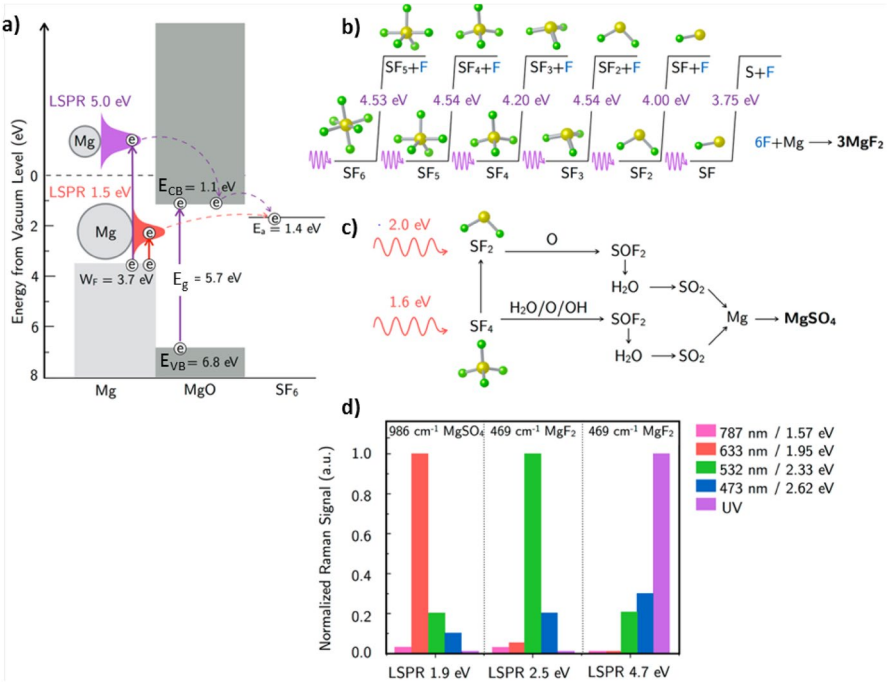

Fig. 11 **a** Energy band diagram of Mg@MgO core–shell NPs for the decomposition of SF_6. $W_F$is the work function of Mg and $E_g$is the electron affinity energy level of SF_6. Reaction scheme of the plasmon-catalyzed decomposition of SF_6 to **b** MgF_2 and **c** $MgSO_4$. **d** Raman signal for different Mg@MgO nanostructures with various LSPR maxima, i.e. at 1.9, 2.5, and 4.7 eV. Adapted with permission from [319]. Copyright (2020) American Chemical Society

a protective LbL polymer shell around the bimetallic NPs, the activity also remained the same after 1 month of ageing [139]. Another successful stabilization method is the full embedment of Au NPs within the TiO_2 film. Recently, Peeters et al. showed that these systems effectively lead to self-cleaning activity enhancement (+ 29% for 1 wt% of Au compared with pristine TiO_2 upon 1 sun AM1.5G illumination) [320].

3.2.4 Disinfection

Initially, hybrid plasmonic nanostructures were not introduced in the disinfection research field for their photocatalytic activity, but mainly in view of other properties. For instance, Au@drug complexes were studied extensively for their photothermal effect or for imaging purposes. Composites with Ag are more common due to the inherent antimicrobial activity of Ag, even in darkness [326, 327]. However, the photocatalytic property holds tremendous promise as well, especially towards antibiotic-resistant strains. The photocatalytically formed oxidative species may induce peroxidation of cell membrane phospholipids, direct DNA damage, and coenzyme A oxidation, which inhibit respiratory activity and result

in cell death [328]. For more in-depth explanations on photocatalytic antimicrobial mechanisms, we gladly refer to the excellent reviews of Markowska-Szczupak et al. [329] and Endo and Kowalska [328].

Ag@metal oxide core–shell hybrids are frequently studied in this context [330–333]. An overview of several recent studies can be found in Table 5. In order to distinguish between photocatalytic effects and the pure antimicrobial properties of metals, the activity both in the dark and upon illumination is given. Unfortunately, due to the lack of standardized experimental parameters, mutual comparison between different studies is again problematic. Inorganic hybrids do not suffer from enzymatic degradation and benefit from more light absorption relative to complexes with organic photosensitizers [333]. Very few disinfection studies deal with plasmonic multi-metal alloys (e.g. alloying Ag with Cu or Pt) [284, 327]. On the other hand, core–shell configurations have shown to be more stable in harsh oxidative environments [330]. Though the release of Ag^+ is considered beneficial for antibacterial purposes [284], it might be important that no (toxic) ions such as Ag^+ or metal ions from the SC leach into the treated water. Das et al. demonstrated with atomic absorption spectroscopy (AAS) for both their Ag@ZnO and Ag@SnO_2@ZnO photocatalysts that no detectable amounts of Ag^+, Zn^{2+}, or Sn^+[330–332]. In addition, they showed superior activity relative to the pure SCs. Ag@ZnO degraded *Vibrio cholera* bacteria 9–10 times better under natural sunlight than ZnO or TiO_2 [332]. Similar results were obtained for *Escherichia coli* [331]. Ag@SnO_2@ZnO was even capable of completely disinfecting 10^7 colony forming units (CFU) mL^{-1} of multidrug resistant *Bacillus* species in 3.5 h under natural sunlight (~ 79 mW cm^{-2} [330]. Here, H_2O_2 was revealed as the dominant oxidative species. However, other disinfection studies point out $O_2^{\circ-}$ as the major oxidant. Interestingly, the use of Ag@AgCl hybrids enables the use of reactive chlorine species (RCS), next to ROS. When AgCl absorbs light, Ag^+ is reduced, while Cl° is formed (Eq. 16) [333].

$$AgCl + h \cdot \nu \rightarrow Ag + Cl^{o} \tag{16}$$

where h is Planck's constant and ν is the frequency of the incoming light.

Recently, Thangudu et al. showed in vivo that the implementation of Ag@AgCl NCs as nanomedicine allowed complete re-epithelialization of subcutaneous abscesses in mice for both multidrug-resistant gram-positive and gram-negative bacteria (Fig. 12) [333]. Note that most disinfection studies deal with bacteria while other organisms such as fungi may also cause harm. The photocatalytic microbial inactivation efficiency is not the same for all microorganisms and seems to follow a pattern correlated with the cell complexity (easiest degradation of gram-negative bacteria > gram-positive bacteria > > fungi (yeast) > fungi (mold)). By using synergistic effects of a well-designed plasmonic hybrid, effective fungi destruction can also be achieved [334]. In 2019, Méndez-Medrano et al. modified TiO_2 with Ag@CuO core–shell nanostructures. Because of the combined effects of the Ag plasmon-enhanced ROS generation, the narrow band gap of CuO (1.7 eV), the penetration of the catalyst in the cell membrane and the presence of germicidal Ag^+ and Cu^+ ions, high antifungal activity was obtained.

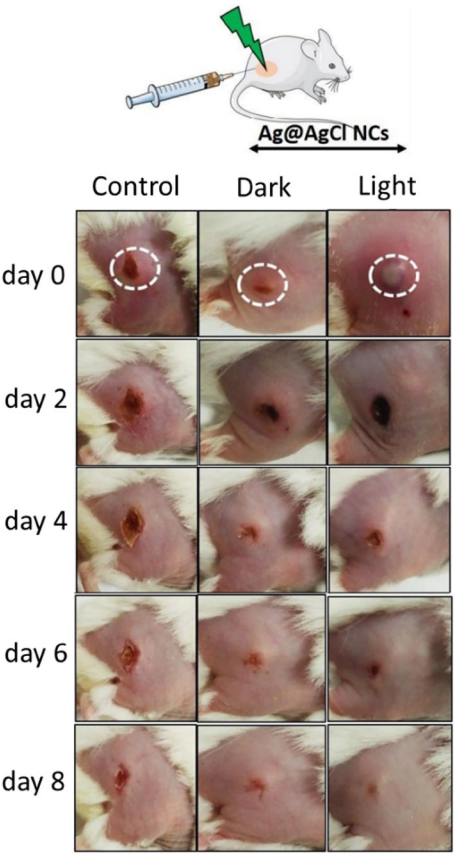

Fig. 12 Images of methicillin-resistant *Staphylococcus aureus* (MRSA) infected mice at different days. One hundred microliters of 1 mg mL^{-1} Ag@AgCl NCs was injected subcutaneously for both the "dark" and "light" experiment. For the latter, the infected region was irradiated with 532-nm laser light for 10 min (250 mW cm^{-2}). Republished with permission of Royal Society of Chemistry, from [333]; permission conveyed through Copyright Clearance Center, Inc

This included growth inhibition for *Aspergillus melleus* and *Penicillium chrysogenum,* but also significant inhibition of sporulation and mycotoxin- or sclerotia-containing droplets [334].

Finally, since wastewater disinfection often makes use of suspended particulate systems, significant catalyst loss may be encountered [330, 332]. Rationally designed core–shell structures consisting of a Ag/AgBr core and a magnetic Fe_2O_3 shell were therefore applied for disinfection purposes [290]. Plasmonic hybrids have also recently been incorporated in membrane matrices. The presence of the plasmonic photocatalysts mitigates membrane (bio)fouling. Li et al. designed cellulose acetate (CA) membranes modified with $Au_{0.1}Ag_{0.9}$-TiO_2 NRs, yielding *E. coli* degradation efficiencies of 98.5% after 30 min of Vis light irradiation ($\lambda > 420$ nm) [292].

$$\text{Bacteriostasis}(\%) = \frac{(\text{A} - \text{B})}{\text{A} \times 100\%} = 100\% - \text{Cellviability} \tag{17}$$

where *A* and *B* are the number of bacteria in control circumstances and in the experimental samples, respectively

Table 5 Several recent disinfection studies using plasmonic hybrid nanostructures, given with their reaction conditions and apparent rate constant both with and without illumination (k_{app} and $k_{app,\ dark,\ respectively}$)

Photocatalyst	Light (intensity)[a]	Reaction medium (temperature, pH)[a]	k_{app}[b] ($k_{app,\ dark}$) [h^{-1}]	References
AgCu-TiO_2	Vis (> 450 nm, NA)	*E. coli* (K12); 1.5×10^8 CFU mL^{-1}; 0.9% NaCl; 7.14 mg catalyst mL^{-1}	~ −1.6 (~ −1.3)	[327]
AgPt-TiO_2	Vis (> 450 nm, NA)	*E. coli* (K12); 1.5×10^8 CFU mL^{-1}; 0.9 NaCl; 7.14 mg catalyst mL^{-1}	~ −0.9 (~ −0.7)	[327]
AgPt-TiO_2	400 nm (0.63 mW cm^{-2})	*P. chrysogenum;* 9.6×10^3 CFU cm^{-2}; 2.4 mg cm^{-2}	−0.66 (−0.56)	[308]
CuAg-TiO_2	400 nm (0.63 mW cm^{-2})	*P. chrysogenum;* 9.6×10^3 CFU cm^{-2}; 2.4 mg cm^{-2}	−0.66 (−0.45)	[308]
AgCu-β-$NaYF_4$:Yb^{3+}, Tm^{3+}@TiO_2	NIR (> 800 nm)	*S. aureus*; 1×10^9 CFU mL^{-1}; 1.67 mg catalyst mL^{-1}	−0.245 (~ 0)	[284]
Ag@SnO_2@ZnO	Natural sunlight (~ 79 mW cm^{-2})	*Bacillus* sp.; 1×10^{-7} CFU mL^{-1}; 0.9% NaCl; 0.5 mg catalyst mL^{-1} (35 °C, pH 6.8)	~ −1.90 (~ 0.01)	[330]
Ag@ZnO	Natural sunlight (NA)	*E. coli*; 5×10^6 CFU mL^{-1}; 0.9% NaCl; 2 mg L^{-1} (35 °C)	~ −4.64 (~ 0.03)	[331]
Ag@ZnO	Natural sunlight (NA)	*S. aureus*; 5×10^6 CFU mL^{-1}; 0.9% NaCl; 3 mg L^{-1} (35 °C)	~ −2.45 (~ 0.20)	[331]
Ag@ZnO	Natural sunlight (NA)	*V. cholera*; 4×10^5 CFU mL^{-1}; 0.5 mg catalyst L^{-1} (35–65 °C)	−2.1 (NA) (35 °C) −7.74 (NA) (65 °C)	[332]
Ag@AgCl NCs	532 nm (250 mW cm^{-2})	MRSA; ~ 1×10^8 CFU mL^{-1}; 0.01 mg catalyst mL^{-1}	~ −1.8[c] (~ 0.1[c])	[333]
Ag@AgCl NCs	532 nm (250 mW cm^{-2})	*E. coli*; 0.01 mg catalyst mL^{-1}	~ −8.5[c] (−7.2[c])	[333]
Ag core in lipid shell layer with incorporated tris(bipyridine)-ruthenium(II)	430 nm (9.76 mW cm^{-2})	*Arthrobacter* sp.; 10^8 bacteria and 10^{10} NPs (1:100) (RT)	−7.03 (~ 0)	[335]
Ag core in lipid shell layer with incorporated tris(bipyridine)-ruthenium(II)	430 nm (9.76 mW cm^{-2})	*E. coli*.; 10^8 bacteria and 10^{10} NPs (1:100) (RT)	−3.93 (~ 0)	[335]
Ag@Cu_2O	Vis (400–700 nm, NA)	*S. aureus*; 1×10^7 CFU mL^{-1}; 0.0568 mg mL^{-1}	−0.14[c] (NA)	[336]
Ag@Cu_2O	Vis (400–700 nm, NA)	*E. coli*; 1×10^7 CFU mL^{-1}; 0.0568 mg mL^{-1}	−0.17[c] (~ −0.03[c])	[336]
$Au_{0.1}Ag_{0.9}$-TiO_2 NRs—CA	Vis (> 420 nm, NA)	*E. coli*; $1\times10^{6-7}$ CFU mL^{-1}	~ −3.7 (−0.59)	[292]

[a]If known

[b]k_{app} Follows the Chick–Watson disinfection model and is determined by the slope of $\log(N/N_0)$ in function of the time where N and N_0 are the actual and initial CFU, respectively. CFUs were counted by conventional colony-counting methods

[c]Calculated from cell viability/bacteriostasis data, derived from the following equation (Eq. 17) [336]:

4 Conclusion and Outlook

Despite significant photocatalytic activity enhancements that have been obtained by myriad well-considered hybrid material combinations, we feel that the efficiencies achieved thus far still leave ample room for improvement. Additional optimization may be achieved by further rational design of such plasmonic hybrid NPs. For instance, Halas's group is investigating core–shell [270] or single-atom alloy [273] plasmonic antenna-reactor systems, in efforts to optimize the activity, selectivity, and stability. Nevertheless, the combination of core–shell and Janus NPs that could possibly yield effective photocatalytic antenna-reactor systems remains relatively unexplored to date. Conversely, less complex rational design may also yield significant improvements. For example, based on a thorough understanding of the dominant underlying plasmon-mediated mechanism(s), better matching of the structure to the mechanism could enhance the overall performance. Hot-spot engineering by adjusting the spacing layers in core–shell configurations seems promising in that regard [5], especially since sub-nanometer control of both insulating and conductive shell layers has been proven to be practically feasible using facile and versatile techniques [21, 84]. It should be noted furthermore that a fundamental theoretical understanding of these processes remains crucial. Utilizing theoretical tools such as DFT and finite-difference time-domain (FDTD) simulations is key to identifying the loopholes and obtaining the most efficient structure and materials. For example, simulations have pointed out the potential of plasmonic atomic clusters. However, the application of such clusters is still underexplored due to the lack of experimental validation. This remains difficult, since these clusters tend to aggregate, complicating further hybridization into even more advanced materials. Small changes in the number of atoms may already yield significant changes in kinetics and thermodynamics [185–187], pointing out the importance of an accurate synthesis method. Solving this, an extra research line may be developed.

While the fabrication of hybrid plasmonic nanomaterials enables many opportunities, the progressive degree of hybrid complexity may not hamper the eventual scale-up of the catalyst synthesis. Hence, research towards simplifying protocols is still very advantageous for the scientific community. One example is the improvement shown by Asapu et al. for the LbL stabilization strategy, leading to faster and cheaper synthesis of metal@polymer NPs [21, 84]. Generally, to further improve synthesis methods, we also feel there is still underexplored potential in using microreactor-based techniques.

Given that sunlight is free, the incorporation of more solar-active metals with activity ranging from UV up to NIR light represents a key line of research. An interesting example provided in that sense was the four-times nanogapped Au–Ag core with a CdS shell, yielding such a broad absorption band [113]. However, noble metals and CdS are not sustainable. Hence, it is more promising to use relatively nontoxic, abundant Al whose LSPR can be tuned between ~ 250 and 650 nm [111]. Also, other more sustainable plasmonic materials such as Cu, Bi, and Mg deserve extra attention. It is even claimed by several pioneers in the

plasmonics field that Al and Mg will be at the center of studies in the near future [28, 111]. Nonetheless, special care should then be taken with respect to long-term stability. Core–shell configurations with protective shells might provide a solution to that end. More stable nanostructures would also allow their introduction in more harsh reaction environments. It would for instance enable to make the shift from photocatalytic H_2 production from (scarce) fresh water to abundant seawater or wastewater as sustainable technology [234]. Considering their activity, the use of core–shell NPs also seems more promising than their alloy counterparts due to the straightforward charge separation between light-absorbing plasmonic cores and reactive shells. However, interesting results are also reported in the field of Janus configurations and deserve further exploration.

Finally, to elucidate the most promising materials, we strongly advise the use of more standardized photocatalytic activity measurements. In order to compare among different studies, at a minimum, the spectral output of the light source, and especially the absolute irradiance incident on the sample, should be documented in each report. Following the proposed research opportunities, significant progress still lies ahead.

Acknowledgements F.D. and H.P. gratefully acknowledge the Research Foundation-Flanders (FWO) for funding through an Aspirant doctoral fellowship (Grant numbers FN700300002 and FN702100002).

Declarations

Conflict of interest On behalf of all authors, Sammy W. Verbruggen states that there is no conflict of interest.

References

1. Artioli G, Angelini I, Polla A (2008) Crystals and phase transitions in protohistoric glass materials. Phase Trans 81:233–252. https://doi.org/10.1080/01411590701514409
2. Bobin O, Schvoerer M, Ney C et al (2003) The role of copper and silver in the colouration of metallic luster decorations (Tunisia, 9th century; Mesopotamia, 10th century; Sicily, 16th century): a first approach. Color Res Appl 28:352–359. https://doi.org/10.1002/col.10183
3. Freestone I, Meeks N, Sax M, Higgitt C (2007) The Lycurgus cup—a Roman nanotechnology. Gold Bull 40:270–277. https://doi.org/10.1007/BF03215599
4. Verbruggen SW (2015) TiO_2 photocatalysis for the degradation of pollutants in gas phase: from morphological design to plasmonic enhancement. J Photochem Photobiol C Photochem Rev 24:64–82. https://doi.org/10.1016/j.jphotochemrev.2015.07.001
5. Linic S, Christopher P, Ingram DB (2011) Plasmonic-metal nanostructures for efficient conversion of solar to chemical energy. Nat Mater 10:911–921
6. Atwater HA, Polman A (2010) Plasmonics for improved photovoltaic devices. Nat Mater 9:205
7. Anker JN, Hall WP, Lyandres O et al (2009) Biosensing with plasmonic nanosensors. Nanoscience and technology. Co-Published with Macmillan Publishers Ltd, UK, pp 308–319
8. Barbillon G (2020) Latest novelties on plasmonic and non-plasmonic nanomaterials for SERS sensing. Nanomater 10:25
9. Wang D, Pillai SC, Ho S-H et al (2018) Plasmonic-based nanomaterials for environmental remediation. Appl Catal B Environ 237:721–741. https://doi.org/10.1016/j.apcatb.2018.05.094
10. Statista (2021) Annual global CO2 emissions from 2000 to 2019. https://www.statista.com/statistics/276629/global-co2-emissions/. Accessed 21 Sep 2021

11. Fuel Cells and Hydrogen Joint Undertaking (FCH) (2019) Hydrogen roadmap Europe—a sustainable pathway for the European energy transition
12. Sharma G, Kumar A, Sharma S et al (2019) Novel development of nanoparticles to bimetallic nanoparticles and their composites: a review. J King Saud Univ Sci 31:257–269. https://doi.org/10.1016/j.jksus.2017.06.012
13. Major KJ, De C, Obare SO (2009) Recent advances in the synthesis of plasmonic bimetallic nanoparticles. Plasmonics 4:61–78. https://doi.org/10.1007/s11468-008-9077-8
14. Kavitha R, Kumar SG (2020) Review on bimetallic-deposited TiO_2: preparation methods, charge carrier transfer pathways and photocatalytic applications. Chem Pap 74:717–756. https://doi.org/10.1007/s11696-019-00995-4
15. Sytwu K, Vadai M, Dionne JA (2019) Bimetallic nanostructures: combining plasmonic and catalytic metals for photocatalysis. Adv Phys X 4:1619480. https://doi.org/10.1080/23746149.2019.1619480
16. Srinoi P, Chen Y-T, Vittur V et al (2018) Bimetallic nanoparticles: enhanced magnetic and optical properties for emerging biological applications. Appl Sci 8:25
17. Chen T, Rodionov VO (2016) Controllable catalysis with nanoparticles: bimetallic alloy systems and surface adsorbates. ACS Catal 6:4025–4033. https://doi.org/10.1021/acscatal.6b00714
18. Ahn J, Kim J, Qin D (2020) Orthogonal deposition of Au on different facets of Ag cuboctahedra for the fabrication of nanoboxes with complementary surfaces. Nanoscale 12:372–379. https://doi.org/10.1039/C9NR08420G
19. Gloag L, Benedetti TM, Cheong S et al (2018) Three-dimensional branched and faceted gold-ruthenium nanoparticles: using nanostructure to improve stability in oxygen evolution electrocatalysis. Angew Chem Int Ed 57:10241–10245. https://doi.org/10.1002/anie.201806300
20. Zhang Q, Kusada K, Wu D et al (2018) Selective control of fcc and hcp crystal structures in Au–Ru solid-solution alloy nanoparticles. Nat Commun 9:510. https://doi.org/10.1038/s41467-018-02933-6
21. Asapu R, Claes N, Bals S et al (2017) Silver-polymer core-shell nanoparticles for ultrastable plasmon-enhanced photocatalysis. Appl Catal B Environ 200:31–38. https://doi.org/10.1016/j.apcatb.2016.06.062
22. Ni Y, Kan C, He L et al (2019) Alloyed Au-Ag nanorods with desired plasmonic properties and stability in harsh environments. Photon Res 7:558–565. https://doi.org/10.1364/PRJ.7.000558
23. Blommaerts N, Vanrompay H, Nuti S et al (2019) Unraveling structural information of turkevich synthesized plasmonic gold-silver bimetallic nanoparticles. Small 15:1902791. https://doi.org/10.1002/smll.201902791
24. Davey WP (1925) Precision measurements of the lattice constants of twelve common metals. Phys Rev 25:753–761. https://doi.org/10.1103/PhysRev.25.753
25. Combettes S, Lam J, Benzo P et al (2020) How interface properties control the equilibrium shape of core–shell Fe–Au and Fe–Ag nanoparticles. Nanoscale 12:18079–18090. https://doi.org/10.1039/D0NR04425C
26. Lohse SE, Burrows ND, Scarabelli L et al (2014) Anisotropic noble metal nanocrystal growth: the role of halides. Chem Mater 26:34–43. https://doi.org/10.1021/cm402384j
27. Jacobson CR, Solti D, Renard D et al (2020) Shining light on aluminum nanoparticle synthesis. Acc Chem Res 53:2020–2030. https://doi.org/10.1021/acs.accounts.0c00419
28. Ringe E (2020) Shapes, plasmonic properties, and reactivity of magnesium nanoparticles. J Phys Chem C 124:15665–15679. https://doi.org/10.1021/acs.jpcc.0c03871
29. Thota S, Wang Y, Zhao J (2018) Colloidal Au–Cu alloy nanoparticles: synthesis, optical properties and applications. Mater Chem Front 2:1074–1089. https://doi.org/10.1039/C7QM00538E
30. Zhang J, Yu Y, Zhang B (2020) Synthesis and characterization of size controlled alloy nanoparticles. Phys Sci Rev. https://doi.org/10.1515/psr-2018-0046
31. Zhao H, Qi W, Zhou X et al (2018) Composition-controlled synthesis of platinum and palladium nanoalloys as highly active electrocatalysts for methanol oxidation. Chin J Catal 39:342–349. https://doi.org/10.1016/S1872-2067(18)63020-7
32. Leteba GM, Lang CI (2013) Synthesis of bimetallic platinum nanoparticles for biosensors. Sensors 13:25
33. Gu J, Lan G, Jiang Y et al (2015) Shaped Pt-Ni nanocrystals with an ultrathin Pt-enriched shell derived from one-pot hydrothermal synthesis as active electrocatalysts for oxygen reduction. Nano Res 8:1480–1496. https://doi.org/10.1007/s12274-014-0632-7

34. Xia Y, Gilroy KD, Peng H-C, Xia X (2017) Seed-mediated growth of colloidal metal nanocrystals. Angew Chem Int Ed 56:60–95. https://doi.org/10.1002/anie.201604731
35. Emam HE (2019) Arabic gum as bio-synthesizer for Ag–Au bimetallic nanocomposite using seed-mediated growth technique and its biological efficacy. J Polym Environ 27:210–223. https://doi.org/10.1007/s10924-018-1331-3
36. Dong P, Wu Y, Guo W, Di J (2013) Plasmonic biosensor based on triangular Au/Ag and Au/Ag/Au core/shell nanoprisms onto indium tin oxide glass. Plasmonics 8:1577–1583. https://doi.org/10.1007/s11468-013-9574-2
37. Sutter E, Zhang B, Sutter P (2020) DNA-mediated three-dimensional assembly of hollow Au–Ag alloy nanocages as plasmonic crystals. ACS Appl Nano Mater 3:8068–8074. https://doi.org/10.1021/acsanm.0c01528
38. Yue X, Hou J, Zhao H et al (2020) Au–Ag alloy nanoparticles with tunable cavity for plasmon-enhanced photocatalytic H2 evolution. J Energy Chem 49:1–7. https://doi.org/10.1016/j.jechem.2020.01.005
39. Sui N, Yue R, Wang Y et al (2019) Boosting methanol oxidation reaction with Au@AgPt yolk-shell nanoparticles. J Alloys Compd 790:792–798. https://doi.org/10.1016/j.jallcom.2019.03.196
40. Kamat GA, Yan C, Osowiecki WT et al (2020) Self-limiting shell formation in Cu@Ag core-shell nanocrystals during galvanic replacement. J Phys Chem Lett 11:5318–5323. https://doi.org/10.1021/acs.jpclett.0c01551
41. Reboul J, Li ZY, Yuan J et al (2021) Synthesis of small Ni-core–Au-shell catalytic nanoparticles on TiO_2 by galvanic replacement reaction. Nanosc Adv 3:823–835. https://doi.org/10.1039/D0NA00617C
42. Wang Z, Ai B, Wang Y et al (2019) Hierarchical control of plasmonic nanochemistry in microreactor. ACS Appl Mater Interfaces 11:35429–35437. https://doi.org/10.1021/acsami.9b10917
43. Sebastian V, Smith CD, Jensen KF (2016) Shape-controlled continuous synthesis of metal nanostructures. Nanoscale 8:7534–7543. https://doi.org/10.1039/C5NR08531D
44. Chen P-C, Liu G, Zhou Y et al (2015) Tip-directed synthesis of multimetallic nanoparticles. J Am Chem Soc 137:9167–9173. https://doi.org/10.1021/jacs.5b05139
45. Neumeister A, Jakobi J, Rehbock C et al (2014) Monophasic ligand-free alloy nanoparticle synthesis determinants during pulsed laser ablation of bulk alloy and consolidated microparticles in water. Phys Chem Chem Phys 16:23671–23678. https://doi.org/10.1039/C4CP03316G
46. Prymak O, Jakobi J, Rehbock C et al (2018) Crystallographic characterization of laser-generated, polymer-stabilized 4 nm silver-gold alloyed nanoparticles. Mater Chem Phys 207:442–450. https://doi.org/10.1016/j.matchemphys.2017.12.080
47. Vegard L (1921) Die Konstitution der Mischkristalle und die Raumfüllung der Atome. Z Phys 5:17–26. https://doi.org/10.1007/BF01349680
48. Petkov V, Shastri S, Shan S et al (2013) Resolving atomic ordering differences in group 11 nanosized metals and binary alloy catalysts by resonant high-energy X-ray diffraction and computer simulations. J Phys Chem C 117:22131–22141. https://doi.org/10.1021/jp408017v
49. Bozzolo G, Garcés JE, Derry GN (2007) Atomistic modeling of segregation and bulk ordering in Ag–Au alloys. Surf Sci 601:2038–2046. https://doi.org/10.1016/j.susc.2007.02.035
50. Nguyen CM, Frias Batista LM, John MG et al (2021) Mechanism of gold-silver alloy nanoparticle formation by laser coreduction of gold and silver ions in solution. J Phys Chem B 125:907–917. https://doi.org/10.1021/acs.jpcb.0c10096
51. Zhang D, Gökce B, Barcikowski S (2017) Laser synthesis and processing of colloids: fundamentals and applications. Chem Rev 117:3990–4103. https://doi.org/10.1021/acs.chemrev.6b00468
52. Liao W, Lan S, Gao L et al (2017) Nanocrystalline high-entropy alloy (CoCrFeNiAl0.3) thin-film coating by magnetron sputtering. Thin Solid Films 638:383–388. https://doi.org/10.1016/j.tsf.2017.08.006
53. Li B, Huang L, Zhou M et al (2014) Preparation and spectral analysis of gold nanoparticles using magnetron sputtering and thermal annealing. J Wuhan Univ Technol Sci Ed 29:651–655. https://doi.org/10.1007/s11595-014-0973-9
54. Atef N, Emara SS, Eissa DS et al (2021) Well-dispersed Au nanoparticles prepared via magnetron sputtering on TiO_2 nanotubes with unprecedentedly high activity for water splitting. Electrochem Sci Adv 1:e2000004. https://doi.org/10.1002/elsa.202000004
55. Sun L, Yuan G, Gao L et al (2021) Chemical vapour deposition. Nat Rev Methods Prim 1:5. https://doi.org/10.1038/s43586-020-00005-y

56. Harvey E, Ghantasala M (2006) In: Hannink RHJ, Hill AJBT-NC of M (eds) 12—Nanofabrication. Woodhead Publishing, pp 303–330
57. Bakrania SD, Rathore GK, Wooldridge MS (2009) An investigation of the thermal decomposition of gold acetate. J Therm Anal Calorim 95:117–122. https://doi.org/10.1007/s10973-008-9173-1
58. Hirayama Y, Takagi K (2019) Evaluation of compositional homogeneity of Fe-Co alloy nanoparticles prepared by thermal plasma synthesis. J Alloys Compd 792:594–598. https://doi.org/10.1016/j.jallcom.2019.04.083
59. Verbruggen SW, Keulemans M, Goris B et al (2016) Plasmonic 'rainbow' photocatalyst with broadband solar light response for environmental applications. Appl Catal B Environ 188:147–153. https://doi.org/10.1016/j.apcatb.2016.02.002
60. Samal AK, Polavarapu L, Rodal-Cedeira S et al (2013) Size tunable Au@Ag core-shell nanoparticles: synthesis and surface-enhanced Raman scattering properties. Langmuir 29:15076–15082. https://doi.org/10.1021/la403707j
61. Boltersdorf J, Leff AC, Forcherio GT, Baker DR (2021) Plasmonic Au–Pd bimetallic nanocatalysts for hot-carrier-enhanced photocatalytic and electrochemical ethanol oxidation. Cryst 11:25
62. Etchegoin PG, Le Ru EC, Meyer M (2006) An analytic model for the optical properties of gold. J Chem Phys 125:164705. https://doi.org/10.1063/1.2360270
63. Balamurugan B, Maruyama T (2005) Evidence of an enhanced interband absorption in Au nanoparticles: size-dependent electronic structure and optical properties. Appl Phys Lett 87:143105. https://doi.org/10.1063/1.2077834
64. Kolwas K, Derkachova A (2020) Impact of the interband transitions in gold and silver on the dynamics of propagating and localized surface plasmons. Nanomater 10:25
65. Borah R, Verbruggen SW (2020) Silver-gold bimetallic alloy versus core-shell nanoparticles: implications for plasmonic enhancement and photothermal applications. J Phys Chem C 124:12081–12094. https://doi.org/10.1021/acs.jpcc.0c02630
66. Ponzellini P, Giovannini G, Cattarin S et al (2019) Metallic nanoporous aluminum-magnesium alloy for UV-enhanced spectroscopy. J Phys Chem C 123:20287–20296. https://doi.org/10.1021/acs.jpcc.9b04230
67. Pujari A, Thomas T (2021) Aluminium nanoparticles alloyed with other earth-abundant plasmonic metals for light trapping in thin-film a-Si solar cells. Sustain Mater Technol 28:e00250. https://doi.org/10.1016/j.susmat.2021.e00250
68. Kim D, Resasco J, Yu Y et al (2014) Synergistic geometric and electronic effects for electrochemical reduction of carbon dioxide using gold–copper bimetallic nanoparticles. Nat Commun 5:4948. https://doi.org/10.1038/ncomms5948
69. Liu Y, Walker ARH (2010) Monodisperse gold-copper bimetallic nanocubes: facile one-step synthesis with controllable size and composition. Angew Chemie Int Ed 49:6781–6785. https://doi.org/10.1002/anie.201001931
70. Henkel A, Jakab A, Brunklaus G, Sönnichsen C (2009) Tuning plasmonic properties by alloying copper into gold nanorods. J Phys Chem C 113:2200–2204. https://doi.org/10.1021/jp810433e
71. De Marchi S, Núñez-Sánchez S, Bodelón G et al (2020) Pd nanoparticles as a plasmonic material: synthesis, optical properties and applications. Nanoscale 12:23424–23443. https://doi.org/10.1039/D0NR06270G
72. Sugawa K, Tahara H, Yamashita A et al (2015) Refractive index susceptibility of the plasmonic palladium nanoparticle: potential as the third plasmonic sensing material. ACS Nano 9:1895–1904. https://doi.org/10.1021/nn506800a
73. Cortie MB, McDonagh AM (2011) Synthesis and optical properties of hybrid and alloy plasmonic nanoparticles. Chem Rev 111:3713–3735. https://doi.org/10.1021/cr1002529
74. Peng Z, Yang H (2008) Ag–Pt alloy nanoparticles with the compositions in the miscibility gap. J Solid State Chem 181:1546–1551. https://doi.org/10.1016/j.jssc.2008.03.013
75. Zhu X, Guo Q, Sun Y et al (2019) Optimising surface d charge of AuPd nanoalloy catalysts for enhanced catalytic activity. Nat Commun 10:1428. https://doi.org/10.1038/s41467-019-09421-5
76. Valenti M, Venugopal A, Tordera D et al (2017) Hot carrier generation and extraction of plasmonic alloy nanoparticles. ACS Photonics 4:1146–1152. https://doi.org/10.1021/acsphotonics.6b01048
77. Kadkhodazadeh S, Nugroho FAA, Langhammer C et al (2019) Optical property-composition correlation in noble metal alloy nanoparticles studied with eeLS. ACS Photon 6:779–786. https://doi.org/10.1021/acsphotonics.8b01791

78. Lee C, Park Y, Park JY (2019) Hot electrons generated by intraband and interband transition detected using a plasmonic Cu/TiO_2 nanodiode. RSC Adv 9:18371–18376. https://doi.org/10.1039/C9RA02601K
79. Keast VJ, Barnett RL, Cortie MB (2014) First principles calculations of the optical and plasmonic response of Au alloys and intermetallic compounds. J Phys Condens Matter 26:305501. https://doi.org/10.1088/0953-8984/26/30/305501
80. Rossi TP, Erhart P, Kuisma M (2020) Hot-carrier generation in plasmonic nanoparticles: the importance of atomic structure. ACS Nano 14:9963–9971. https://doi.org/10.1021/acsnano.0c03004
81. Ma J, Zhang X, Gao S (2021) Tunable electron and hole injection channels at plasmonic Al– TiO_2 interfaces. Nanoscale 13:14073–14080. https://doi.org/10.1039/D1NR03697A
82. Huang H, Zhang L, Lv Z et al (2016) Unraveling surface plasmon decay in core-shell nanostructures toward broadband light-driven catalytic organic synthesis. J Am Chem Soc 138:6822–6828. https://doi.org/10.1021/jacs.6b02532
83. van der Hoeven JES, Jelic J, Olthof LA et al (2021) Unlocking synergy in bimetallic catalysts by core–shell design. Nat Mater. https://doi.org/10.1038/s41563-021-00996-3
84. Asapu R, Claes N, Ciocarlan R-G et al (2019) Electron transfer and near-field mechanisms in plasmonic gold-nanoparticle-modified TiO_2 photocatalytic systems. ACS Appl Nano Mater 2:4067–4074. https://doi.org/10.1021/acsanm.9b00485
85. Pougin A, Dodekatos G, Dilla M et al (2018) Au@ TiO_2 core-shell composites for the photocatalytic reduction of CO2. Chem A Eur J 24:12416–12425. https://doi.org/10.1002/chem.201801796
86. Hong D, Lyu L-M, Koga K et al (2019) Plasmonic Ag@ TiO_2 core-shell nanoparticles for enhanced CO2 photoconversion to CH4. ACS Sustain Chem Eng 7:18955–18964. https://doi.org/10.1021/acssuschemeng.9b04345
87. Mondal I, Gonuguntla S, Pal U (2019) Photoinduced fabrication of Cu/TiO_2 core-shell heterostructures derived from Cu-MOF for solar hydrogen generation: the size of the Cu nanoparticle matters. J Phys Chem C 123:26073–26081. https://doi.org/10.1021/acs.jpcc.9b07171
88. Prodan E, Radloff C, Halas NJ, Nordlander P (2003) A hybridization model for the plasmon response of complex nanostructures. Science (80–) 302:419–422. https://doi.org/10.1126/science.1089171
89. Kamimura S, Yamashita S, Abe S et al (2017) Effect of core@shell (Au@Ag) nanostructure on surface plasmon-induced photocatalytic activity under visible light irradiation. Appl Catal B Environ 211:11–17. https://doi.org/10.1016/j.apcatb.2017.04.028
90. Wang Y, Zhang Q, Wang Y et al (2021) Ultrastable plasmonic Cu-based core-shell nanoparticles. Chem Mater 33:695–705. https://doi.org/10.1021/acs.chemmater.0c04059
91. Joplin A, Hosseini Jebeli SA, Sung E et al (2017) Correlated absorption and scattering spectroscopy of individual platinum-decorated gold nanorods reveals strong excitation enhancement in the nonplasmonic metal. ACS Nano 11:12346–12357. https://doi.org/10.1021/acsnano.7b06239
92. Song HM, Moosa BA, Khashab NM (2012) Water-dispersable hybrid Au–Pd nanoparticles as catalysts in ethanol oxidation, aqueous phase Suzuki-Miyaura and Heck reactions. J Mater Chem 22:15953–15959. https://doi.org/10.1039/C2JM32702C
93. Wang F, Li C, Chen H et al (2013) Plasmonic harvesting of light energy for Suzuki coupling reactions. J Am Chem Soc 135:5588–5601. https://doi.org/10.1021/ja310501y
94. Lai H, Xiao W, Wang Y et al (2021) Plasmon-induced carrier separation boosts high-selective photocatalytic CO2 reduction on dagger-axe-like Cu@Co core–shell bimetal. Chem Eng J 417:129295. https://doi.org/10.1016/j.cej.2021.129295
95. Kuo C-S, Lyu L-M, Sia R-F et al (2020) Ultrathin octahedral cupt nanocages obtained by facet transformation from rhombic dodecahedral core-shell nanocrystals. ACS Sustain Chem Eng 8:10544–10553. https://doi.org/10.1021/acssuschemeng.0c03256
96. Tsai C-H, Chen S-Y, Song J-M et al (2015) Effect of Ag templates on the formation of Au-Ag hollow/core-shell nanostructures. Nanosc Res Lett 10:438. https://doi.org/10.1186/s11671-015-1141-7
97. Yang Y, Liu J, Fu Z-W, Qin D (2014) Galvanic replacement-free deposition of Au on Ag for core-shell nanocubes with enhanced chemical stability and SERS activity. J Am Chem Soc 136:8153–8156. https://doi.org/10.1021/ja502472x
98. Mendoza C, Désert A, Chateau D et al (2020) Au nanobipyramids@mSiO2 core–shell nanoparticles for plasmon-enhanced singlet oxygen photooxygenations in segmented flow microreactors. Nanoscale Adv 2:5280–5287. https://doi.org/10.1039/D0NA00533A

99. Mostafa AM, Mwafy EA, Awwad NS, Ibrahium HA (2021) Au@Ag core/shell nanoparticles prepared by laser-assisted method for optical limiting applications. J Mater Sci Mater Electron 32:14728–14739. https://doi.org/10.1007/s10854-021-06028-9
100. Cha SK, Mun JH, Chang T et al (2015) Au–Ag core-shell nanoparticle array by block copolymer lithography for synergistic broadband plasmonic properties. ACS Nano 9:5536–5543. https://doi.org/10.1021/acsnano.5b01641
101. Forcherio GT, Baker DR, Boltersdorf J et al (2018) Targeted deposition of platinum onto gold nanorods by plasmonic hot electrons. J Phys Chem C 122:28901–28909. https://doi.org/10.1021/acs.jpcc.8b07868
102. van der Hoeven JES, Deng T-S, Albrecht W et al (2021) Structural control over bimetallic core-shell nanorods for surface-enhanced raman spectroscopy. ACS Omega 6:7034–7046. https://doi.org/10.1021/acsomega.0c06321
103. Spitaleri L, Nicotra G, Zimbone M et al (2019) Fast and efficient sun light photocatalytic activity of Au_ZnO core-shell nanoparticles prepared by a one-pot synthesis. ACS Omega 4:15061–15066. https://doi.org/10.1021/acsomega.9b01850
104. Huang J, He Y, Wang L et al (2017) Bifunctional Au@TiO_2 core–shell nanoparticle films for clean water generation by photocatalysis and solar evaporation. Energy Convers Manag 132:452–459. https://doi.org/10.1016/j.enconman.2016.11.053
105. Hartman T, Weckhuysen BM (2018) Thermally stable TiO_2- and SiO_2-shell-isolated au nanoparticles for in situ plasmon-enhanced raman spectroscopy of hydrogenation catalysts. Chem A Eur J 24:3733–3741. https://doi.org/10.1002/chem.201704370
106. Kamarudheen R, Kumari G, Baldi A (2020) Plasmon-driven synthesis of individual metal@semiconductor core@shell nanoparticles. Nat Commun 11:3957. https://doi.org/10.1038/s41467-020-17789-y
107. Eom H, Jung J-Y, Shin Y et al (2014) Strong localized surface plasmon resonance effects of Ag/TiO_2 core–shell nanowire arrays in UV and visible light for photocatalytic activity. Nanoscale 6:226–234. https://doi.org/10.1039/C3NR04388F
108. Seong S, Park I-S, Jung YC et al (2019) Synthesis of Ag-ZnO core-shell nanoparticles with enhanced photocatalytic activity through atomic layer deposition. Mater Des 177:107831. https://doi.org/10.1016/j.matdes.2019.107831
109. Liz-Marzán LM, Giersig M, Mulvaney P (1996) Synthesis of nanosized gold−silica core−shell particles. Langmuir 12:4329–4335. https://doi.org/10.1021/la9601871
110. Huang MH, Rej S, Chiu C-Y (2015) Facet-dependent optical properties revealed through investigation of polyhedral Au–Cu2O and bimetallic core-shell nanocrystals. Small 11:2716–2726. https://doi.org/10.1002/smll.201403542
111. Knight MW, King NS, Liu L et al (2014) Aluminum for plasmonics. ACS Nano 8:834–840. https://doi.org/10.1021/nn405495q
112. Ma X, Zhao K, Tang H et al (2014) New insight into the role of gold nanoparticles in Au@CdS core-shell nanostructures for hydrogen evolution. Small 10:4664–4670. https://doi.org/10.1002/smll.201401494
113. Ma L, Chen Y-L, Yang D-J et al (2020) Multi-interfacial plasmon coupling in multigap (Au/AgAu)@CdS core–shell hybrids for efficient photocatalytic hydrogen generation. Nanoscale 12:4383–4392. https://doi.org/10.1039/C9NR09696E
114. Lee C, Shin K, Lee YJ et al (2018) Effects of shell thickness on Ag-Cu2O core-shell nanoparticles with bumpy structures for enhancing photocatalytic activity and stability. Catal Today 303:313–319. https://doi.org/10.1016/j.cattod.2017.08.016
115. Bai X, Zong R, Li C et al (2014) Enhancement of visible photocatalytic activity via Ag@C3N4 core–shell plasmonic composite. Appl Catal B Environ 147:82–91. https://doi.org/10.1016/j.apcatb.2013.08.007
116. Ning X, Lu G (2020) Photocorrosion inhibition of CdS-based catalysts for photocatalytic overall water splitting. Nanoscale 12:1213–1223. https://doi.org/10.1039/C9NR09183A
117. Monga A, Bathla A, Pal B (2017) A Cu-Au bimetallic co-catalysis for the improved photocatalytic activity of TiO_2 under visible light radiation. Sol Energy 155:1403–1410. https://doi.org/10.1016/j.solener.2017.07.084
118. Li A, Zhu W, Li C et al (2019) Rational design of yolk–shell nanostructures for photocatalysis. Chem Soc Rev 48:1874–1907. https://doi.org/10.1039/C8CS00711J

119. Sun H, He Q, Zeng S et al (2017) Controllable growth of Au@TiO_2 yolk–shell nanoparticles and their geometry parameter effects on photocatalytic activity. New J Chem 41:7244–7252. https://doi.org/10.1039/C7NJ01491K
120. Wang Y, Yang C, Chen A et al (2019) Influence of yolk-shell Au@TiO_2 structure induced photocatalytic activity towards gaseous pollutant degradation under visible light. Appl Catal B Environ 251:57–65. https://doi.org/10.1016/j.apcatb.2019.03.056
121. Yang H, Li M, Li S et al (2020) A critical structured TiO_2 with enhanced photocatalytic activity during the formation of yolk-shell structured TiO_2. J Mater Sci Mater Electron 31:2–9. https://doi.org/10.1007/s10854-018-9986-z
122. Zhao B, Guo X, Zhao W et al (2017) Facile synthesis of yolk–shell Ni@void@SnO2(Ni3Sn2) ternary composites via galvanic replacement/Kirkendall effect and their enhanced microwave absorption properties. Nano Res 10:331–343. https://doi.org/10.1007/s12274-016-1295-3
123. Li A, Zhang P, Chang X et al (2015) Gold nanorod@TiO_2 yolk-shell nanostructures for visible-light-driven photocatalytic oxidation of benzyl alcohol. Small 11:1892–1899. https://doi.org/10.1002/smll.201403058
124. Wang W, Efrima S, Regev O (1998) Directing oleate stabilized nanosized silver colloids into organic phases. Langmuir 14:602–610. https://doi.org/10.1021/la9710177
125. Tzhayik O, Sawant P, Efrima S et al (2002) Xanthate capping of silver, copper, and gold colloids. Langmuir 18:3364–3369. https://doi.org/10.1021/la015653n
126. Heinz H, Pramanik C, Heinz O et al (2017) Nanoparticle decoration with surfactants: molecular interactions, assembly, and applications. Surf Sci Rep 72:1–58. https://doi.org/10.1016/j.surfrep.2017.02.001
127. Turkevich J, Stevenson PC, Hillier J (1951) a Study of the nucleation and growth processes I N the synthesis of. Discuss Faraday Soc. https://doi.org/10.1039/DF9511100055
128. Verbruggen SW, Keulemans M, Filippousi M et al (2014) Plasmonic gold–silver alloy on TiO_2 photocatalysts with tunable visible light activity. Appl Catal B Environ 156–157:116–121. https://doi.org/10.1016/j.apcatb.2014.03.027
129. Cao M, Liu Q, Chen M et al (2017) Dispersing hydrophilic nanoparticles in nonaqueous solvents with superior long-term stability. RSC Adv 7:25535–25541. https://doi.org/10.1039/C7RA03472E
130. Xing S, Tan LH, Yang M et al (2009) Highly controlled core/shell structures: tunable conductive polymer shells on gold nanoparticles and nanochains. J Mater Chem 19:3286–3291. https://doi.org/10.1039/B900993K
131. Chen J-Y, Wu H-C, Chiu Y-C, Chen W-C (2014) Plasmon-enhanced polymer photovoltaic device performance using different patterned Ag/PVP electrospun nanofibers. Adv Energy Mater 4:1301665. https://doi.org/10.1002/aenm.201301665
132. Yu S, Wilson AJ, Heo J, Jain PK (2018) Plasmonic control of multi-electron transfer and C-C coupling in visible-light-driven CO2 reduction on Au nanoparticles. Nano Lett 18:2189–2194. https://doi.org/10.1021/acs.nanolett.7b05410
133. Kvítek L, Panáček A, Soukupová J et al (2008) Effect of surfactants and polymers on stability and antibacterial activity of silver nanoparticles (NPs). J Phys Chem C 112:5825–5834. https://doi.org/10.1021/jp711616v
134. Lisunova M, Mahmoud M, Holland N et al (2012) The unusual fluorescence intensity enhancement of poly(p-phenyleneethynylene) polymer separated from the silver nanocube surface by H-bonded LbL shells. J Mater Chem 22:16745–16753. https://doi.org/10.1039/C2JM32450D
135. Schneider G, Decher G (2004) From functional core/shell nanoparticles prepared via layer-by-layer deposition to empty nanospheres. Nano Lett 4:1833–1839. https://doi.org/10.1021/nl0490826
136. Schneider G, Decher G (2008) Functional core/shell nanoparticles via layer-by-layer assembly. investigation of the experimental parameters for controlling particle aggregation and for enhancing dispersion stability. Langmuir 24:1778–1789. https://doi.org/10.1021/la7021837
137. Claes N, Asapu R, Blommaerts N et al (2018) Characterization of silver-polymer core–shell nanoparticles using electron microscopy. Nanoscale 10:9186–9191. https://doi.org/10.1039/C7NR09517A
138. Yu X, Lei DY, Amin F et al (2013) Distance control in-between plasmonic nanoparticles via biological and polymeric spacers. Nano Today 8:480–493. https://doi.org/10.1016/j.nantod.2013.09.001
139. Dingenen F, Blommaerts N, Van Hal M et al (2021) Layer-by-layer-stabilized plasmonic gold-silver nanoparticles on TiO_2: towards stable solar active photocatalysts. Nanomater 11:25

140. Liang L, Lam SH, Ma L et al (2020) (Gold nanorod core)/(poly(3,4-ethylene-dioxythiophene) shell) nanostructures and their monolayer arrays for plasmonic switching. Nanoscale 12:20684–20692. https://doi.org/10.1039/D0NR05502F
141. Yang K, Li Y, Huang K et al (2014) Promoted effect of PANI on the preferential oxidation of CO in the presence of H2 over Au/ TiO_2 under visible light irradiation. Int J Hydrogen Energy 39:18312–18325. https://doi.org/10.1016/j.ijhydene.2014.09.053
142. Jeon J-W, Ledin PA, Geldmeier JA et al (2016) Electrically controlled plasmonic behavior of gold nanocube@polyaniline nanostructures: transparent plasmonic aggregates. Chem Mater 28:2868–2881. https://doi.org/10.1021/acs.chemmater.6b00882
143. Wang X, Shen Y, Xie A, Chen S (2013) One-step synthesis of Ag@PANI nanocomposites and their application to detection of mercury. Mater Chem Phys 140:487–492. https://doi.org/10.1016/j.matchemphys.2013.03.058
144. Jiang N, Zhuo X, Wang J (2018) Active plasmonics: principles, structures, and applications. Chem Rev 118:3054–3099. https://doi.org/10.1021/acs.chemrev.7b00252
145. Lu W, Jiang N, Wang J (2017) Active electrochemical plasmonic switching on polyaniline-coated gold nanocrystals. Adv Mater 29:1604862. https://doi.org/10.1002/adma.201604862
146. Magnozzi M, Brasse Y, König TAF et al (2020) Plasmonics of Au/polymer core/shell nanocomposites for thermoresponsive hybrid metasurfaces. ACS Appl Nano Mater 3:1674–1682. https://doi.org/10.1021/acsanm.9b02403
147. Pastoriza-Santos I, Kinnear C, Pérez-Juste J et al (2018) Plasmonic polymer nanocomposites. Nat Rev Mater 3:375–391. https://doi.org/10.1038/s41578-018-0050-7
148. Seh ZW, Liu S, Low M et al (2012) Janus Au-TiO_2 photocatalysts with strong localization of plasmonic near-fields for efficient visible-light hydrogen generation. Adv Mater 24:2310–2314. https://doi.org/10.1002/adma.201104241
149. Tong F, Lou Z, Liang X et al (2020) Plasmon-induced dehydrogenation of formic acid on Pd-dotted Ag@Au hexagonal nanoplates and single-particle study. Appl Catal B Environ 277:119226. https://doi.org/10.1016/j.apcatb.2020.119226
150. Liu L, Dao TD, Kodiyath R et al (2014) Plasmonic janus-composite photocatalyst comprising Au and C-TiO_2 for enhanced aerobic oxidation over a broad visible-light range. Adv Funct Mater 24:7754–7762. https://doi.org/10.1002/adfm.201402088
151. Wen L, Xu R, Cui C et al (2018) Template-guided programmable janus heteronanostructure arrays for efficient plasmonic photocatalysis. Nano Lett 18:4914–4921. https://doi.org/10.1021/acs.nanolett.8b01675
152. Robatjazi H, Lou M, Clark BD et al (2020) Site-selective nanoreactor deposition on photocatalytic Al nanocubes. Nano Lett 20:4550–4557. https://doi.org/10.1021/acs.nanolett.0c01405
153. Zhang H, Lam SH, Guo Y et al (2021) Selective deposition of catalytic metals on plasmonic Au nanocups for room-light-active photooxidation of o-phenylenediamine. ACS Appl Mater Interfaces. https://doi.org/10.1021/acsami.1c03806
154. Albrecht W, Bladt E, Vanrompay H et al (2019) Thermal stability of gold/palladium octopods studied in situ in 3D: understanding design rules for thermally stable metal nanoparticles. ACS Nano 13:6522–6530. https://doi.org/10.1021/acsnano.9b00108
155. Ben-Shahar Y, Banin U (2016) Hybrid semiconductor-metal nanorods as photocatalysts. Top Curr Chem 374:54. https://doi.org/10.1007/s41061-016-0052-0
156. Lee SW, Hong JW, Lee H et al (2018) The surface plasmon-induced hot carrier effect on the catalytic activity of CO oxidation on a Cu2O/hexoctahedral Au inverse catalyst. Nanoscale 10:10835–10843. https://doi.org/10.1039/C8NR00555A
157. Liu L, Yang H, Ren X et al (2015) Au–ZnO hybrid nanoparticles exhibiting strong charge-transfer-induced SERS for recyclable SERS-active substrates. Nanoscale 7:5147–5151. https://doi.org/10.1039/C5NR00491H
158. Daware K, Kasture M, Kalubarme R et al (2019) Detection of toxic metal ions Pb2+ in water using SiO2@Au core-shell nanostructures: a simple technique for water quality monitoring. Chem Phys Lett 732:136635. https://doi.org/10.1016/j.cplett.2019.136635
159. Reguera J, Flora T, Winckelmans N et al (2020) Self-assembly of Janus Au:Fe3O4 branched nanoparticles. From organized clusters to stimuli-responsive nanogel suprastructures. Nanosc Adv 2:2525–2530. https://doi.org/10.1039/D0NA00102C
160. Yang L, Yan Z, Yang L et al (2020) Photothermal conversion of SiO2@Au nanoparticles mediated by surface morphology of gold cluster layer. RSC Adv 10:33119–33128. https://doi.org/10.1039/D0RA06278B

161. Li W, Guo Y, Zhang P (2010) General strategy to prepare TiO_2-core gold-shell nanoparticles as SERS-Tags. J Phys Chem C 114:7263–7268. https://doi.org/10.1021/jp908160m
162. Elmoula MA, Panaitescu E, Phan M et al (2009) Controlled attachment of gold nanoparticles on ordered titania nanotube arrays. J Mater Chem 19:4483–4487. https://doi.org/10.1039/B903197A
163. Gurbatov SO, Modin E, Puzikov V et al (2021) Black Au-decorated TiO_2 produced via laser ablation in liquid. ACS Appl Mater Interfaces 13:6522–6531. https://doi.org/10.1021/acsami.0c20463
164. Tang KY, Chen JX, Legaspi EDR et al (2021) Gold-decorated TiO_2 nanofibrous hybrid for improved solar-driven photocatalytic pollutant degradation. Chemosphere 265:129114. https://doi.org/10.1016/j.chemosphere.2020.129114
165. Liu T, Li Y (2016) Plasmonic solar desalination. Nat Photon 10:361–362. https://doi.org/10.1038/nphoton.2016.97
166. Dhiman M, Maity A, Das A et al (2019) Plasmonic colloidosomes of black gold for solar energy harvesting and hotspots directed catalysis for CO2 to fuel conversion. Chem Sci 10:6594–6603. https://doi.org/10.1039/C9SC02369K
167. Efremova MV, Nalench YA, Myrovali E et al (2018) Size-selected Fe3O4-Au hybrid nanoparticles for improved magnetism-based theranostics. Beilstein J Nanotechnol 9:2684–2699. https://doi.org/10.3762/bjnano.9.251
168. Zhou L, Zhang H, Bao H et al (2018) Decoration of Au nanoparticles on MoS2 nanospheres: from janus to core/shell structure. J Phys Chem C 122:8628–8636. https://doi.org/10.1021/acs.jpcc.8b01216
169. Chen P, Hu J, Yin M et al (2021) MoS2 nanoflowers decorated with Au nanoparticles for visible-light-enhanced gas sensing. ACS Appl Nano Mater. https://doi.org/10.1021/acsanm.1c00847
170. Ponnuvelu DV, Dhakshinamoorthy J, Prasad AK et al (2020) Geometrically controlled Au-decorated ZnO heterojunction nanostructures for NO2 detection. ACS Appl Nano Mater 3:5898–5909. https://doi.org/10.1021/acsanm.0c01053
171. Kim J-H, Mirzaei A, Kim HW, Kim SS (2019) Realization of Au-decorated WS2 nanosheets as low power-consumption and selective gas sensors. Sens Actuators B Chem 296:126659. https://doi.org/10.1016/j.snb.2019.126659
172. Dunklin JR, Lafargue P, Higgins TM et al (2018) Monolayer-enriched production of Au-decorated WS2 nanosheets via defect engineering. MRS Adv 3:2435–2440. https://doi.org/10.1557/adv.2018.350
173. Ahmad MZ, Sadek AZ, Yaacob MH et al (2013) Optical characterisation of nanostructured Au/WO3 thin films for sensing hydrogen at low concentrations. Sens Actuators B Chem 179:125–130. https://doi.org/10.1016/j.snb.2012.09.102
174. KarthickRaj AG, Murugan C, Pandikumar A (2021) Efficient photoelectrochemical reduction of carbon dioxide into alcohols assisted by photoanode driven water oxidation with gold nanoparticles decorated titania nanotubes. J CO2 Util 52:101684. https://doi.org/10.1016/j.jcou.2021.101684
175. Gao Z, Ye H, Tang D et al (2017) Platinum-decorated gold nanoparticles with dual functionalities for ultrasensitive colorimetric in vitro diagnostics. Nano Lett 17:5572–5579. https://doi.org/10.1021/acs.nanolett.7b02385
176. Noel K, Wang X (2019) Pt-decorated Au nanoparticles: highly active catalyst for formic acid oxidation. ECS Trans 16:639–645. https://doi.org/10.1149/1.2981899
177. Zhao Z, Heck KN, Limpornpipat P et al (2019) Hydrogen-generating behavior of Pd-decorated gold nanoparticles via formic acid decomposition. Catal Today 330:24–31. https://doi.org/10.1016/j.cattod.2018.06.044
178. Kang Y, Ye X, Chen J et al (2013) Engineering catalytic contacts and thermal stability: gold/iron oxide binary nanocrystal superlattices for CO oxidation. J Am Chem Soc 135:1499–1505. https://doi.org/10.1021/ja310427u
179. Shibuta M, Yamamoto K, Ohta T et al (2021) Confined hot electron relaxation at the molecular heterointerface of the size-selected plasmonic noble metal nanocluster and layered C60. ACS Nano 15:1199–1209. https://doi.org/10.1021/acsnano.0c08248
180. Liao TW, Verbruggen SW, Claes N et al (2018) TiO_2 films modified with au nanoclusters as self-cleaning surfaces under visible light. Nanomaterials 8:1–9. https://doi.org/10.3390/nano8010030
181. Attia Y, Samer M (2017) Metal clusters: new era of hydrogen production. Renew Sustain Energy Rev 79:878–892. https://doi.org/10.1016/j.rser.2017.05.113
182. Zheng J, Zhang C, Dickson RM (2004) Highly fluorescent, water-soluble, size-tunable gold quantum dots. Phys Rev Lett 93:77402. https://doi.org/10.1103/PhysRevLett.93.077402
183. Fitzgerald JM, Narang P, Craster RV et al (2016) Quantum plasmonics. Proc IEEE 104:2307–2322

184. Bozhevolnyi SI, Khurgin JB (2017) The case for quantum plasmonics. Nat Photon 11:398–400. https://doi.org/10.1038/nphoton.2017.103
185. Van Dao D, Cipriano LA, Di Liberto G et al (2021) Plasmonic Au nanoclusters dispersed in nitrogen-doped graphene as a robust photocatalyst for light-to-hydrogen conversion. J Mater Chem A 9:22810–22819. https://doi.org/10.1039/D1TA05445G
186. Wieghold S, Nienhaus L, Knoller FL et al (2017) Plasmonic support-mediated activation of 1 nm platinum clusters for catalysis. Phys Chem Chem Phys 19:30570–30577. https://doi.org/10.1039/C7CP04882C
187. Joo SH, Park JY, Renzas JR et al (2010) Size effect of ruthenium nanoparticles in catalytic carbon monoxide oxidation. Nano Lett 10:2709–2713. https://doi.org/10.1021/nl101700j
188. Rong H, Ji S, Zhang J et al (2020) Synthetic strategies of supported atomic clusters for heterogeneous catalysis. Nat Commun 11:5884. https://doi.org/10.1038/s41467-020-19571-6
189. Palmer RE, Cai R, Vernieres J (2018) Synthesis without solvents: the cluster (nanoparticle) beam route to catalysts and sensors. Acc Chem Res 51:2296–2304. https://doi.org/10.1021/acs.accounts.8b00287
190. Zhang J, Li Z, Zheng K, Li G (2018) Synthesis and characterization of size-controlled atomically precise gold clusters. Phys Sci Rev. https://doi.org/10.1515/psr-2017-0083
191. Li J, Ye W, Chen C (2019) Chapter-5 Removal of toxic/radioactive metal ions by metal-organic framework-based materials. In: Chen CBTIS (ed) Emerging natural and tailored nanomaterials for radioactive waste treatment and environmental remediation. Elsevier, New York, pp 217–279
192. Hamoud HI, Douma F, Lafjah M et al (2022) Size-dependent photocatalytic activity of silver nanoparticles embedded in ZX-Bi zeolite supports. ACS Appl Nano Mater 5:3866–3877. https://doi.org/10.1021/acsanm.1c04484
193. Liao Y, Li J, Thomas A (2017) General route to high surface area covalent organic frameworks and their metal oxide composites as magnetically recoverable adsorbents and for energy storage. ACS Macro Lett 6:1444–1450. https://doi.org/10.1021/acsmacrolett.7b00849
194. Blommaerts N, Hoeven N, Arenas Esteban D et al (2021) Tuning the turnover frequency and selectivity of photocatalytic CO2 reduction to CO and methane using platinum and palladium nanoparticles on Ti-Beta zeolites. Chem Eng J 410:128234. https://doi.org/10.1016/j.cej.2020.128234
195. El-Roz M, Telegeiev I, Mordvinova NE et al (2018) Uniform generation of sub-nanometer silver clusters in zeolite cages exhibiting high photocatalytic activity under visible light. ACS Appl Mater Interfaces 10:28702–28708. https://doi.org/10.1021/acsami.8b09634
196. Robatjazi H, Weinberg D, Swearer DF et al (2019) Metal-organic frameworks tailor the properties of aluminum nanocrystals. Sci Adv 5:eaav5340. https://doi.org/10.1126/sciadv.aav5340
197. Shevchenko EV, Talapin DV, Kotov NA et al (2006) Structural diversity in binary nanoparticle superlattices. Nature 439:55–59. https://doi.org/10.1038/nature04414
198. Ye X, Chen J, Diroll BT, Murray CB (2013) Tunable plasmonic coupling in self-assembled binary nanocrystal superlattices studied by correlated optical microspectrophotometry and electron microscopy. Nano Lett 13:1291–1297. https://doi.org/10.1021/nl400052w
199. Swearer DF, Zhao H, Zhou L et al (2016) Heterometallic antenna–reactor complexes for photocatalysis. Proc Natl Acad Sci 113:8916–8920. https://doi.org/10.1073/pnas.1609769113
200. Ciracì C, Hill RT, Mock JJ et al (2012) Probing the ultimate limits of plasmonic enhancement. Science (80–) 337:1072–1074. https://doi.org/10.1126/science.1224823
201. Ma X-C, Dai Y, Yu L, Huang B-B (2016) Energy transfer in plasmonic photocatalytic composites. Light Sci Appl 5:e16017. https://doi.org/10.1038/lsa.2016.17
202. Linsebigler AL, Lu GQ, Yates JT (1995) Photocatalysis on Tio2 surfaces—principles, mechanisms, and selected results. Chem Rev 95:735–758
203. Mubeen S, Lee J, Singh N et al (2013) An autonomous photosynthetic device in which all charge carriers derive from surface plasmons. Nat Nanotechnol 8:247–251. https://doi.org/10.1038/nnano.2013.18
204. Brown LV, Zhao K, King N et al (2013) Surface-enhanced infrared absorption using individual cross antennas tailored to chemical moieties. J Am Chem Soc 135:3688–3695. https://doi.org/10.1021/ja312694g
205. Chen X-J, Cabello G, Wu D-Y, Tian Z-Q (2014) Surface-enhanced Raman spectroscopy toward application in plasmonic photocatalysis on metal nanostructures. J Photochem Photobiol C Photochem Rev 21:54–80. https://doi.org/10.1016/j.jphotochemrev.2014.10.003
206. Burda C, Chen X, Narayanan R, El-Sayed MA (2005) Chemistry and properties of nanocrystals of different shapes. Chem Rev 105:1025–1102. https://doi.org/10.1021/cr030063a

207. Hodak JH, Martini I, Hartland GV (1998) Spectroscopy and dynamics of nanometer-sized noble metal particles. J Phys Chem B 102:6958–6967. https://doi.org/10.1021/jp9809787
208. Lehmann J, Merschdorf M, Pfeiffer W et al (2000) Surface plasmon dynamics in silver nanoparticles studied by femtosecond time-resolved photoemission. Phys Rev Lett 85:2921–2924. https://doi.org/10.1103/PhysRevLett.85.2921
209. Kale MJ, Avanesian T, Christopher P (2014) Direct photocatalysis by plasmonic nanostructures. ACS Catal 4:116–128. https://doi.org/10.1021/cs400993w
210. Kim C, Suh BL, Yun H et al (2017) Surface plasmon aided ethanol dehydrogenation using Ag–Ni binary nanoparticles. ACS Catal 7:2294–2302. https://doi.org/10.1021/acscatal.7b00411
211. Petek H (2012) Photoexcitation of adsorbates on metal surfaces: one-step or three-step. J Chem Phys 137:091704. https://doi.org/10.1063/1.4746801
212. Mukherjee S, Libisch F, Large N et al (2013) Hot electrons do the impossible: plasmon-induced dissociation of H2 on Au. Nano Lett 13:240–247. https://doi.org/10.1021/nl303940z
213. Boerigter C, Campana R, Morabito M, Linic S (2016) Evidence and implications of direct charge excitation as the dominant mechanism in plasmon-mediated photocatalysis. Nat Commun 7:10545. https://doi.org/10.1038/ncomms10545
214. Zhao H, Zheng X, Feng X, Li Y (2018) CO 2 reduction by plasmonic au nanoparticle-decorated TiO 2 photocatalyst with an ultrathin Al_2O_3 interlayer. J Phys Chem C 122:18949–18956. https://doi.org/10.1021/acs.jpcc.8b04239
215. Gomes Silva C, Juárez R, Marino T et al (2011) Influence of excitation wavelength (UV or visible light) on the photocatalytic activity of titania containing gold nanoparticles for the generation of hydrogen or oxygen from water. J Am Chem Soc 133:595–602. https://doi.org/10.1021/ja1086358
216. Torimoto T, Horibe H, Kameyama T et al (2011) Plasmon-enhanced photocatalytic activity of cadmium sulfide nanoparticle immobilized on silica-coated gold particles. J Phys Chem Lett 2:2057–2062. https://doi.org/10.1021/jz2009049
217. Tu W, Zhou Y, Li H et al (2015) Au@TiO 2 yolk–shell hollow spheres for plasmon-induced photocatalytic reduction of CO 2 to solar fuel via a local electromagnetic field. Nanoscale 7:14232–14236. https://doi.org/10.1039/C5NR02943K
218. Hirakawa T, Kamat PV (2005) Charge separation and catalytic activity of Ag@TiO_2 core-shell composite clusters under UV-irradiation. J Am Chem Soc 127:3928–3934. https://doi.org/10.1021/ja042925a
219. Clavero C (2014) Plasmon-induced hot-electron generation at nanoparticle/metal-oxide interfaces for photovoltaic and photocatalytic devices. Nat Photon 8:95–103. https://doi.org/10.1038/nphoton.2013.238
220. Subramanian V, Wolf EE, Kamat PV (2004) Catalysis with TiO_2/gold nanocomposites. Effect of metal particle size on the Fermi level equilibration. J Am Chem Soc 126:4943–4950
221. Li J, Cushing SK, Meng F et al (2015) Plasmon-induced resonance energy transfer for solar energy conversion. Nat Photon 9:601–607. https://doi.org/10.1038/nphoton.2015.142
222. Ingram DB, Christopher P, Bauer JL, Linic S (2011) Predictive model for the design of plasmonic metal/semiconductor composite photocatalysts. Acs Catal 1:1441–1447
223. Borah R, Verbruggen SW (2019) Coupled plasmon modes in 2D gold nanoparticle clusters and their effect on local temperature control. J Phys Chem C. https://doi.org/10.1021/acs.jpcc.9b09048
224. Yu S, Wilson AJ, Kumari G et al (2017) Opportunities and challenges of solar-energy-driven carbon dioxide to fuel conversion with plasmonic catalysts. ACS Energy Lett 2:2058–2070. https://doi.org/10.1021/acsenergylett.7b00640
225. Kreibig U, Vollmer M (1995) Optical properties of metal clusters. Springer, Berlin
226. Baffou G, Quidant R, Girard C (2010) Thermoplasmonics modeling: a Green's function approach. Phys Rev B 82:165424. https://doi.org/10.1103/PhysRevB.82.165424
227. Baffou G, Berto P, Bermúdez Ureña E et al (2013) Photoinduced heating of nanoparticle arrays. ACS Nano 7:6478–6488. https://doi.org/10.1021/nn401924n
228. Ni G, Miljkovic N, Ghasemi H et al (2015) Volumetric solar heating of nanofluids for direct vapor generation. Nano Energy 17:290–301. https://doi.org/10.1016/j.nanoen.2015.08.021
229. Priebe JB, Karnahl M, Junge H et al (2013) Water reduction with visible light: synergy between optical transitions and electron transfer in Au-TiO(2) catalysts visualized by in situ EPR spectroscopy. Angew Chem Int Ed Engl 52:11420–11424. https://doi.org/10.1002/anie.201306504
230. Caretti I, Keulemans M, Verbruggen SW et al (2015) Light-induced processes in plasmonic Gold/TiO_2 photocatalysts studied by electron paramagnetic resonance. Top Catal 58:776–782. https://doi.org/10.1007/s11244-015-0419-4

231. Awazu K, Fujimaki M, Rockstuhl C et al (2008) A plasmonic photocatalyst consisting of sliver nanoparticles embedded in titanium dioxide. J Am Chem Soc 130:1676–1680
232. Sun S, Rasskazov IL, Carney PS et al (2020) Critical role of shell in enhanced fluorescence of metal-dielectric core–shell nanoparticles. J Phys Chem C 124:13365–13373. https://doi.org/10.1021/acs.jpcc.0c03415
233. Asapu R, Ciocarlan R-G, Claes N et al (2017) Plasmonic near-field localization of silver core-shell nanoparticle assemblies via wet chemistry nanogap engineering. ACS Appl Mater Interfaces 9:41577–41585. https://doi.org/10.1021/acsami.7b13965
234. Dingenen F, Verbruggen SW (2021) Tapping hydrogen fuel from the ocean: a review on photocatalytic, photoelectrochemical and electrolytic splitting of seawater. Renew Sustain Energy Rev 142:110866. https://doi.org/10.1016/j.rser.2021.110866
235. Habisreutinger SN, Schmidt-Mende L, Stolarczyk JK (2013) Photocatalytic reduction of CO2 on TiO_2 and other semiconductors. Angew Chem Int Ed 52:7372–7408. https://doi.org/10.1002/anie.201207199
236. Yang J-L, He Y-L, Ren H et al (2021) Boosting photocatalytic hydrogen evolution reaction using dual plasmonic antennas. ACS Catal 11:5047–5053. https://doi.org/10.1021/acscatal.1c00795
237. Tran PD, Wong LH, Barber J, Loo JSC (2012) Recent advances in hybrid photocatalysts for solar fuel production. Energy Environ Sci 5:5902–5918. https://doi.org/10.1039/C2EE02849B
238. Koppenol WH, Stanbury DM, Bounds PL (2010) Electrode potentials of partially reduced oxygen species, from dioxygen to water. Free Radic Biol Med 49:317–322. https://doi.org/10.1016/j.freeradbiomed.2010.04.011
239. Ha E, Lee LYS, Man H-W et al (2015) Morphology-controlled synthesis of Au/Cu2FeSnS4 core-shell nanostructures for plasmon-enhanced photocatalytic hydrogen generation. ACS Appl Mater Interfaces 7:9072–9077. https://doi.org/10.1021/acsami.5b00715
240. Bhunia K, Chandra M, Khilari S, Pradhan D (2019) Bimetallic PtAu alloy nanoparticles-integrated g-C3N4 hybrid as an efficient photocatalyst for water-to-hydrogen conversion. ACS Appl Mater Interfaces 11:478–488. https://doi.org/10.1021/acsami.8b12183
241. Bian H, Nguyen NT, Yoo J et al (2018) Forming a highly active, homogeneously Alloyed AuPt Co-catalyst decoration on TiO_2 nanotubes directly during anodic growth. ACS Appl Mater Interfaces 10:18220–18226. https://doi.org/10.1021/acsami.8b03713
242. Rahul TK, Mohan M, Sandhyarani N (2018) Enhanced solar hydrogen evolution over in situ gold-platinum bimetallic nanoparticle-loaded Ti3+ self-doped titania photocatalysts. ACS Sustain Chem Eng 6:3049–3059. https://doi.org/10.1021/acssuschemeng.7b02898
243. Gesesse GD, Wang C, Chang BK et al (2020) A soft-chemistry assisted strong metal–support interaction on a designed plasmonic core–shell photocatalyst for enhanced photocatalytic hydrogen production. Nanoscale 12:7011–7023. https://doi.org/10.1039/C9NR09891G
244. Ngaw CK, Xu Q, Tan TTY et al (2014) A strategy for in-situ synthesis of well-defined core–shell Au@TiO_2 hollow spheres for enhanced photocatalytic hydrogen evolution. Chem Eng J 257:112–121. https://doi.org/10.1016/j.cej.2014.07.059
245. Lou Z, Fujitsuka M, Majima T (2016) Pt–Au triangular nanoprisms with strong dipole plasmon resonance for hydrogen generation studied by single-particle spectroscopy. ACS Nano 10:6299–6305. https://doi.org/10.1021/acsnano.6b02494
246. Gao M, Connor PKN, Ho GW (2016) Plasmonic photothermic directed broadband sunlight harnessing for seawater catalysis and desalination. Energy Environ Sci 9:3151–3160. https://doi.org/10.1039/C6EE00971A
247. Hung S-F, Yu Y-C, Suen N-T et al (2016) The synergistic effect of a well-defined Au@Pt core–shell nanostructure toward photocatalytic hydrogen generation: interface engineering to improve the Schottky barrier and hydrogen-evolved kinetics. Chem Commun 52:1567–1570. https://doi.org/10.1039/C5CC08547K
248. Nasrallah H, Douma F, Hamoud HI, El-Roz M (2021). In: Nguyen V-H, Vo D-VN, Nanda SBT-NP (eds) Chapter 5—metal nanoparticles in photocatalysis: advances and challenges. Elsevier, New York, pp 119–143
249. Pandit S, Kunwar S, Pandey P, Lee J (2019) Improved LSPR properties of Ag–Pt and Pt nanoparticles: a systematic study on various configurations and compositions of NPs via the solid-state dewetting of Ag–Pt bilayers. Metals 9:25
250. Sui M, Kunwar S, Pandey P, Lee J (2019) Strongly confined localized surface plasmon resonance (LSPR) bands of Pt, AgPt, AgAuPt nanoparticles. Sci Rep 9:16582. https://doi.org/10.1038/s41598-019-53292-1

251. Xiao J-D, Han L, Luo J et al (2018) Integration of plasmonic effects and schottky junctions into metal-organic framework composites: steering charge flow for enhanced visible-light photocatalysis. Angew Chem Int Ed 57:1103–1107. https://doi.org/10.1002/anie.201711725
252. Liu Y, Sun Z, Hu YH (2021) Bimetallic cocatalysts for photocatalytic hydrogen production from water. Chem Eng J 409:128250. https://doi.org/10.1016/j.cej.2020.128250
253. Ding J, Li X, Chen L et al (2018) Photocatalytic hydrogen production over plasmonic AuCu/CaIn2S4 composites with different AuCu atomic arrangements. Appl Catal B Environ 224:322–329. https://doi.org/10.1016/j.apcatb.2017.10.045
254. Zhang P, Zeng G, Song T et al (2019) Design of plasmonic CuCo bimetal as a nonsemiconductor photocatalyst for synchronized hydrogen evolution and storage. Appl Catal B Environ 242:389–396. https://doi.org/10.1016/j.apcatb.2018.10.020
255. Naya S, Kume T, Akashi R et al (2018) Red-light-driven water splitting by Au(Core)–CdS(Shell) half-cut nanoegg with heteroepitaxial junction. J Am Chem Soc 140:1251–1254. https://doi.org/10.1021/jacs.7b12972
256. Wu B, Liu D, Mubeen S et al (2016) Anisotropic growth of TiO_2 onto gold nanorods for plasmon-enhanced hydrogen production from water reduction. J Am Chem Soc 138:1114–1117. https://doi.org/10.1021/jacs.5b11341
257. Zheng Z, Tachikawa T, Majima T (2014) Single-particle study of Pt-modified au nanorods for plasmon-enhanced hydrogen generation in visible to near-infrared region. J Am Chem Soc 136:6870–6873. https://doi.org/10.1021/ja502704n
258. Han C, Wu L, Ge L et al (2015) AuPd bimetallic nanoparticles decorated graphitic carbon nitride for highly efficient reduction of water to H2 under visible light irradiation. Carbon N Y 92:31–40. https://doi.org/10.1016/j.carbon.2015.02.070
259. Verma R, Belgamwar R, Polshettiwar V (2021) Plasmonic photocatalysis for CO2 conversion to chemicals and fuels. ACS Mater Lett 3:574–598. https://doi.org/10.1021/acsmaterialslett.1c00081
260. Inoue T, Fujishima A, Konishi S, Honda K (1979) Photoelectrocatalytic reduction of carbon dioxide in aqueous suspensions of semiconductor powders. Nature 277:637–638. https://doi.org/10.1038/277637a0
261. Yu S, Jain PK (2019) Plasmonic photosynthesis of C1–C3 hydrocarbons from carbon dioxide assisted by an ionic liquid. Nat Commun 10:2022. https://doi.org/10.1038/s41467-019-10084-5
262. Ziarati A, Badiei A, Luque R et al (2020) Visible light CO2 reduction to CH4 using hierarchical Yolk@shell TiO_2–xHx modified with plasmonic Au–Pd nanoparticles. ACS Sustain Chem Eng 8:3689–3696. https://doi.org/10.1021/acssuschemeng.9b06751
263. Wei Y, Jiao J, Zhao Z et al (2015) Fabrication of inverse opal TiO_2-supported Au@CdS core–shell nanoparticles for efficient photocatalytic CO2 conversion. Appl Catal B Environ 179:422–432. https://doi.org/10.1016/j.apcatb.2015.05.041
264. Choi KM, Kim D, Rungtaweevoranit B et al (2017) Plasmon-enhanced photocatalytic CO2 conversion within metal-organic frameworks under visible light. J Am Chem Soc 139:356–362. https://doi.org/10.1021/jacs.6b11027
265. Bera S, Lee JE, Rawal SB, Lee WI (2016) Size-dependent plasmonic effects of Au and Au@SiO2 nanoparticles in photocatalytic CO2 conversion reaction of Pt/TiO_2. Appl Catal B Environ 199:55–63. https://doi.org/10.1016/j.apcatb.2016.06.025
266. Stanley JNG, García-García I, Perfrement T et al (2019) Plasmonic effects on CO2 reduction over bimetallic Ni-Au catalysts. Chem Eng Sci 194:94–104. https://doi.org/10.1016/j.ces.2018.04.003
267. Lang Q, Yang Y, Zhu Y et al (2017) High-index facet engineering of PtCu cocatalysts for superior photocatalytic reduction of CO2 to CH4. J Mater Chem A 5:6686–6694. https://doi.org/10.1039/C7TA00737J
268. Neaţu Ş, Maciá-Agulló JA, Concepción P, Garcia H (2014) Gold-copper nanoalloys supported on TiO_2 as photocatalysts for CO2 reduction by water. J Am Chem Soc 136:15969–15976. https://doi.org/10.1021/ja506433k
269. Han Y, Xu H, Su Y et al (2019) Noble metal (Pt, Au@Pd) nanoparticles supported on metal organic framework (MOF-74) nanoshuttles as high-selectivity CO2 conversion catalysts. J Catal 370:70–78. https://doi.org/10.1016/j.jcat.2018.12.005
270. Robatjazi H, Zhao H, Swearer DF et al (2017) Plasmon-induced selective carbon dioxide conversion on earth-abundant aluminum-cuprous oxide antenna-reactor nanoparticles. Nat Commun 8:27. https://doi.org/10.1038/s41467-017-00055-z

271. Liu H, Meng X, Dao TD et al (2015) Conversion of carbon dioxide by methane reforming under visible-light irradiation: surface-plasmon-mediated nonpolar molecule activation. Angew Chem 127:11707–11711. https://doi.org/10.1002/ange.201504933
272. Liu H, Li M, Dao TD et al (2016) Design of PdAu alloy plasmonic nanoparticles for improved catalytic performance in CO2 reduction with visible light irradiation. Nano Energy 26:398–404. https://doi.org/10.1016/j.nanoen.2016.05.045
273. Zhou L, Martirez JMP, Finzel J et al (2020) Light-driven methane dry reforming with single atomic site antenna-reactor plasmonic photocatalysts. Nat Energy 5:61–70. https://doi.org/10.1038/s41560-019-0517-9
274. Yan X, Ohno T, Nishijima K et al (2006) Is methylene blue an appropriate substrate for a photocatalytic activity test? A study with visible-light responsive titania. Chem Phys Lett 429:606–610. https://doi.org/10.1016/j.cplett.2006.08.081
275. Misra M, Singh N, Gupta RK (2017) Enhanced visible-light-driven photocatalytic activity of Au@Ag core–shell bimetallic nanoparticles immobilized on electrospun TiO_2 nanofibers for degradation of organic compounds. Catal Sci Technol 7:570–580. https://doi.org/10.1039/C6CY02085B
276. Darabdhara G, Das MR (2019) Dual responsive magnetic Au@Ni nanostructures loaded reduced graphene oxide sheets for colorimetric detection and photocatalytic degradation of toxic phenolic compounds. J Hazard Mater 368:365–377. https://doi.org/10.1016/j.jhazmat.2019.01.010
277. Su J, Zhang Y, Xu S et al (2014) Highly efficient and recyclable triple-shelled Ag@Fe3O4@SiO2@TiO_2 photocatalysts for degradation of organic pollutants and reduction of hexavalent chromium ions. Nanoscale 6:5181–5192. https://doi.org/10.1039/C4NR00534A
278. Tanaka A, Hashimoto K, Kominami H (2011) Gold and copper nanoparticles supported on cerium(IV) oxide—a photocatalyst mineralizing organic acids under red light irradiation. ChemCatChem 3:1619–1623. https://doi.org/10.1002/cctc.201100158
279. Tanaka A, Fuku K, Nishi T et al (2013) Functionalization of Au/TiO_2 plasmonic photocatalysts with Pd by formation of a core-shell structure for effective dechlorination of chlorobenzene under irradiation of visible light. J Phys Chem C 117:16983–16989. https://doi.org/10.1021/jp403855p
280. Cybula A, Priebe JB, Pohl M-M et al (2014) The effect of calcination temperature on structure and photocatalytic properties of Au/Pd nanoparticles supported on TiO_2. Appl Catal B Environ 152–153:202–211. https://doi.org/10.1016/j.apcatb.2014.01.042
281. Yu H, Wang X, Sun H, Huo M (2010) Photocatalytic degradation of malathion in aqueous solution using an Au–Pd–TiO_2 nanotube film. J Hazard Mater 184:753–758. https://doi.org/10.1016/j.jhazmat.2010.08.103
282. Zielińska-Jurek A, Kowalska E, Sobczak JW et al (2011) Preparation and characterization of monometallic (Au) and bimetallic (Ag/Au) modified-titania photocatalysts activated by visible light. Appl Catal B Environ 101:504–514. https://doi.org/10.1016/j.apcatb.2010.10.022
283. Jiang T, Jia C, Zhang L et al (2015) Gold and gold–palladium alloy nanoparticles on heterostructured TiO_2 nanobelts as plasmonic photocatalysts for benzyl alcohol oxidation. Nanoscale 7:209–217. https://doi.org/10.1039/C4NR05905K
284. Zhang Y, Wang L, Kong X et al (2018) Novel Ag-Cu bimetallic alloy decorated near-infrared responsive three-dimensional rod-like architectures for efficient photocatalytic water purification. J Colloid Interface Sci 522:29–39. https://doi.org/10.1016/j.jcis.2018.02.005
285. Patnaik S, Sahoo DP, Parida KM (2020) Bimetallic co-effect of Au-Pd alloyed nanoparticles on mesoporous silica modified g-C3N4 for single and simultaneous photocatalytic oxidation of phenol and reduction of hexavalent chromium. J Colloid Interface Sci 560:519–535. https://doi.org/10.1016/j.jcis.2019.09.041
286. Wen H, Long Y, Han W et al (2018) Preparation of a novel bimetallic AuCu-P25-rGO ternary nanocomposite with enhanced photocatalytic degradation performance. Appl Catal A Gen 549:237–244. https://doi.org/10.1016/j.apcata.2017.09.028
287. Fu R, Li L, Li X et al (2021) Photogenerated carrier separation and localized surface plasmon resonance in SnS2@AuNPs Janus heterostructures for enhanced visible light catalysis. Mater Chem Phys 267:124702. https://doi.org/10.1016/j.matchemphys.2021.124702
288. Naya S, Tada H (2020) Au–Ag alloy nanoparticle-incorporated AgBr plasmonic photocatalyst. Sci Rep 10:19972. https://doi.org/10.1038/s41598-020-77062-6
289. Sugano Y, Shiraishi Y, Tsukamoto D et al (2013) Supported Au–Cu bimetallic alloy nanoparticles: an aerobic oxidation catalyst with regenerable activity by visible-light irradiation. Angew Chem Int Ed 52:5295–5299. https://doi.org/10.1002/anie.201301669

290. Huang S, Xu Y, Chen Z et al (2015) A core–shell structured magnetic Ag/AgBr@Fe_2O_3 composite with enhanced photocatalytic activity for organic pollutant degradation and antibacterium. RSC Adv 5:71035–71045. https://doi.org/10.1039/C5RA13403J
291. Zhou N, Polavarapu L, Gao N et al (2013) TiO_2 coated Au/Ag nanorods with enhanced photocatalytic activity under visible light irradiation. Nanoscale 5:4236–4241. https://doi.org/10.1039/C3NR00517H
292. Li W, Li B, Meng M et al (2019) Bimetallic Au/Ag decorated TiO_2 nanocomposite membrane for enhanced photocatalytic degradation of tetracycline and bactericidal efficiency. Appl Surf Sci 487:1008–1017. https://doi.org/10.1016/j.apsusc.2019.05.162
293. Kaur M, Shinde SL, Ishii S et al (2020) Marimo-bead-supported core-shell nanocomposites of titanium nitride and chromium-doped titanium dioxide as a highly efficient water-floatable green photocatalyst. ACS Appl Mater Interfaces 12:31327–31339. https://doi.org/10.1021/acsami.0c03781
294. Bathla A, Younis SA, Pal B, Kim K-H (2021) Recent progress in bimetallic nanostructure impregnated metal-organic framework for photodegradation of organic pollutants. Appl Mater Today 24:101105. https://doi.org/10.1016/j.apmt.2021.101105
295. Testa JJ, Grela MA, Litter MI (2004) Heterogeneous photocatalytic reduction of chromium(VI) over TiO_2 particles in the presence of oxalate: involvement of Cr(V) species. Environ Sci Technol 38:1589–1594. https://doi.org/10.1021/es0346532
296. Mohammadi P, Sheibani H (2019) Evaluation, of the bimetallic photocatalytic performance of Resin–Au–Pd nanocomposite for degradation of parathion pesticide under visible light. Polyhedron 170:132–137. https://doi.org/10.1016/j.poly.2019.05.030
297. Chen Q, Xin Y, Zhu X (2015) Au-Pd nanoparticles-decorated TiO_2 nanobelts for photocatalytic degradation of antibiotic levofloxacin in aqueous solution. Electrochim Acta 186:34–42. https://doi.org/10.1016/j.electacta.2015.10.095
298. Zhang K, Liu Y, Deng J et al (2018) Co–Pd/$BiVO_4$: high-performance photocatalysts for the degradation of phenol under visible light irradiation. Appl Catal B Environ 224:350–359. https://doi.org/10.1016/j.apcatb.2017.10.044
299. Darabdhara G, Boruah PK, Borthakur P et al (2016) Reduced graphene oxide nanosheets decorated with Au–Pd bimetallic alloy nanoparticles towards efficient photocatalytic degradation of phenolic compounds in water. Nanoscale 8:8276–8287. https://doi.org/10.1039/C6NR00231E
300. Zeng Q, Xie X, Wang X et al (2018) Enhanced photocatalytic performance of Ag@TiO_2 for the gaseous acetaldehyde photodegradation under fluorescent lamp. Chem Eng J 341:83–92. https://doi.org/10.1016/j.cej.2018.02.015
301. Wang Z, Yan S, Sun Y et al (2017) Bi metal sphere/graphene oxide nanohybrids with enhanced direct plasmonic photocatalysis. Appl Catal B Environ 214:148–157. https://doi.org/10.1016/j.apcatb.2017.05.040
302. Wang W, Zhang D, Sun P et al (2021) High efficiency photocatalytic degradation of indoor formaldehyde by Ag/g-C_3N_4/TiO_2 composite catalyst with ZSM-5 as the carrier. Microporous Mesoporous Mater 322:111134. https://doi.org/10.1016/j.micromeso.2021.111134
303. Haldorai Y, Kim B-K, Jo Y-L, Shim J-J (2014) Ag@graphene oxide nanocomposite as an efficient visible-light plasmonic photocatalyst for the degradation of organic pollutants: a facile green synthetic approach. Mater Chem Phys 143:1452–1461. https://doi.org/10.1016/j.matchemphys.2013.11.065
304. Wang D, Li Z, Zhou J et al (2017) Simultaneous detection and removal of formaldehyde at room temperature: Janus Au@ZnO@ZIF-8 nanoparticles. Nano-Micro Lett 10:4. https://doi.org/10.1007/s40820-017-0158-0
305. Tripathy SK, Mishra A, Jha SK et al (2013) Synthesis of thermally stable monodispersed Au@SnO_2 core–shell structure nanoparticles by a sonochemical technique for detection and degradation of acetaldehyde. Anal Methods 5:1456–1462. https://doi.org/10.1039/C3AY26549H
306. Gao J, Si Z, Xu Y et al (2019) Pd–Ag@CeO_2 catalyst of core-shell structure for low temperature oxidation of toluene under visible light irradiation. J Phys Chem C 123:1761–1769. https://doi.org/10.1021/acs.jpcc.8b09060
307. Sun S, Wang W, Zhang L et al (2009) Ag@C core/shell nanocomposite as a highly efficient plasmonic photocatalyst. Catal Commun 11:290–293. https://doi.org/10.1016/j.catcom.2009.09.026
308. Wysocka I, Markowska-Szczupak A, Szweda P et al (2019) Gas-phase removal of indoor volatile organic compounds and airborne microorganisms over mono- and bimetal-modified (Pt, Cu, Ag) titanium(IV) oxide nanocomposites. Indoor Air 29:979–992. https://doi.org/10.1111/ina.12595

309. Wu Q, Ye J, Qiao W et al (2021) Inhibit the formation of toxic methylphenolic by-products in photo-decomposition of formaldehyde–toluene/xylene mixtures by Pd cocatalyst on TiO_2. Appl Catal B Environ 291:120118. https://doi.org/10.1016/j.apcatb.2021.120118
310. Yang K, Huang K, He Z et al (2014) Promoted effect of PANI as electron transfer promoter on CO oxidation over Au/TiO_2. Appl Catal B Environ 158–159:250–257. https://doi.org/10.1016/j.apcatb.2014.04.028
311. Liu J, Lucci FR, Yang M et al (2016) Tackling CO poisoning with single-atom alloy catalysts. J Am Chem Soc 138:6396–6399. https://doi.org/10.1021/jacs.6b03339
312. Novello P, Varanasi CV, Liu J (2019) Effects of light on catalytic activities and lifetime of plasmonic Au catalysts in the CO oxidation reaction. ACS Catal 9:578–586. https://doi.org/10.1021/acscatal.8b03166
313. Li K, Hogan NJ, Kale MJ et al (2017) Balancing near-field enhancement, absorption, and scattering for effective antenna-reactor plasmonic photocatalysis. Nano Lett 17:3710–3717. https://doi.org/10.1021/acs.nanolett.7b00992
314. Jupnik H (1941) Photoelectric properties of bismuth. Phys Rev 60:884–889. https://doi.org/10.1103/PhysRev.60.884
315. Chen M, Li Y, Wang Z et al (2017) Controllable synthesis of core-shell Bi@amorphous Bi_2O_3 nanospheres with tunable optical and photocatalytic activity for NO removal. Ind Eng Chem Res 56:10251–10258. https://doi.org/10.1021/acs.iecr.7b02497
316. Zhang P, Rao Y, Huang Y et al (2021) Transformation of amorphous Bi_2O_3 to crystal $Bi_2O_2CO_3$ on Bi nanospheres surface for photocatalytic NOx oxidation: intensified hot-electron transfer and reactive oxygen species generation. Chem Eng J 420:129814. https://doi.org/10.1016/j.cej.2021.129814
317. Li F, Dong B, Feng S (2019) Bi shell-BiOI core microspheres modified TiO_2 nanotube arrays photoanode: improved effect of Bi shell on photoelectrochemical hydrogen evolution in seawater. Int J Hydrogen Energy 44:29986–29999. https://doi.org/10.1016/j.ijhydene.2019.09.210
318. Zhang W, Dong X, Liang Y et al (2018) Ag/AgCl nanoparticles assembled on BiOCl/$Bi_{12}O_{17}C_{l2}$ nanosheets: enhanced plasmonic visible light photocatalysis and in situ DRIFTS investigation. Appl Surf Sci 455:236–243. https://doi.org/10.1016/j.apsusc.2018.05.171
319. Gutiérrez Y, Giangregorio MM, Palumbo F et al (2020) Sustainable and tunable Mg/MgO Plasmon-catalytic platform for the grand challenge of SF6 environmental remediation. Nano Lett 20:3352–3360. https://doi.org/10.1021/acs.nanolett.0c00244
320. Peeters H, Keulemans M, Nuyts G et al (2020) Plasmonic gold-embedded TiO_2 thin films as photocatalytic self-cleaning coatings. Appl Catal B Environ 267:118654. https://doi.org/10.1016/j.apcatb.2020.118654
321. Wu X-F, Song H-Y, Yoon J-M et al (2009) Synthesis of core−shell Au@TiO_2 nanoparticles with truncated wedge-shaped morphology and their photocatalytic properties. Langmuir 25:6438–6447. https://doi.org/10.1021/la900035a
322. Zhu S, Xie X, Chen S-C et al (2017) Cu-Ni nanowire-based TiO_2 hybrid for the dynamic photodegradation of acetaldehyde gas pollutant under visible light. Appl Surf Sci 408:117–124. https://doi.org/10.1016/j.apsusc.2017.02.217
323. Yang K, Huang K, Lin L et al (2015) Superior preferential oxidation of carbon monoxide in hydrogen-rich stream under visible light irradiation over gold loaded hedgehog-shaped titanium dioxide nanospheres: identification of copper oxide decoration as an efficient promoterSuperior preferenti. J Power Sources 284:194–205. https://doi.org/10.1016/j.jpowsour.2015.03.003
324. He W, Sun Y, Jiang G et al (2018) Defective Bi_4MoO_9/Bi metal core/shell heterostructure: enhanced visible light photocatalysis and reaction mechanism. Appl Catal B Environ 239:619–627. https://doi.org/10.1016/j.apcatb.2018.08.064
325. Xiao X, Zhang W, Yu J et al (2016) Mechanistic understanding of ternary Ag/AgCl@La(OH)3 nanorods as novel visible light plasmonic photocatalysts. Catal Sci Technol 6:5003–5010. https://doi.org/10.1039/C6CY00262E
326. Ding X, Zhang L, Gao Y (2017) Insights into electrolyte effects on photoactivities of dye-sensitized photoelectrochemical cells for water splitting. J Energy Chem 26:476–480. https://doi.org/10.1016/j.jechem.2016.11.022
327. Wysocka I, Kowalska E, Ryl J et al (2019) Morphology, photocatalytic and antimicrobial properties of TiO_2 modified with mono- and bimetallic copper, platinum and silver nanoparticles. Nanomater 9:25

328. Endo-Kimura M, Kowalska E (2020) Plasmonic photocatalysts for microbiological applications. Catal 10:25
329. Markowska-Szczupak A, Ulfig K, Morawski AW (2011) The application of titanium dioxide for deactivation of bioparticulates: an overview. Catal Today 169:249–257. https://doi.org/10.1016/j.cattod.2010.11.055
330. Das S, Misra AJ, HabeebRahman AP et al (2019) Ag@SnO_2@ZnO core-shell nanocomposites assisted solar-photocatalysis downregulates multidrug resistance in *Bacillus* sp.: a catalytic approach to impede antibiotic resistance. Appl Catal B Environ 259:118065. https://doi.org/10.1016/j.apcatb.2019.118065
331. Das S, Ranjana N, Misra AJ et al (2017) Disinfection of the water borne pathogens *Escherichia coli* and *Staphylococcus aureus* by solar photocatalysis using sonochemically synthesized reusable Ag@ZnO core-shell nanoparticles. Int J Environ Res Public Health 14:25
332. Das S, Sinha S, Suar M et al (2015) Solar-photocatalytic disinfection of *Vibrio cholerae* by using Ag@ZnO core–shell structure nanocomposites. J Photochem Photobiol B Biol 142:68–76. https://doi.org/10.1016/j.jphotobiol.2014.10.021
333. Thangudu S, Kulkarni SS, Vankayala R et al (2020) Photosensitized reactive chlorine species-mediated therapeutic destruction of drug-resistant bacteria using plasmonic core–shell Ag@AgCl nanocubes as an external nanomedicine. Nanoscale 12:12970–12984. https://doi.org/10.1039/D0NR01300E
334. Méndez-Medrano MG, Kowalska E, Endo-Kimura M et al (2019) Inhibition of fungal growth using modified TiO_2 with core@Shell structure of Ag@CuO clusters. ACS Appl Bio Mater 2:5626–5633. https://doi.org/10.1021/acsabm.9b00707
335. An X, Naowarojna N, Liu P, Reinhard BM (2020) Hybrid plasmonic photoreactors as visible light-mediated bactericides. ACS Appl Mater Interfaces 12:106–116. https://doi.org/10.1021/acsami.9b14834
336. Feng H, Wang W, Wang W et al (2021) Charge transfer channels of silver @ cuprous oxide heterostructure core-shell nanoparticles strengthen high photocatalytic antibacterial activity. J Colloid Interface Sci 601:531–543. https://doi.org/10.1016/j.jcis.2021.05.113

Publisher's Note Springer Nature remains neutral with regard to jurisdictional claims in published maps and institutional affiliations.

Authors and Affiliations

Rajeshreddy Ninakanti[1,2] · Fons Dingenen[1,2] · Rituraj Borah[1,2] · Hannelore Peeters[1,2] · Sammy W. Verbruggen[1,2]

✉ Sammy W. Verbruggen
sammy.verbruggen@uantwerpen.be

[1] Sustainable Energy, Air and Water Technology (DuEL), Department of Bioscience Engineering, University of Antwerp, Groenenborgerlaan 171, 2020 Antwerp, Belgium

[2] NANOlab Center of Excellence, University of Antwerp, Groenenborgerlaan 171, 2020 Antwerp, Belgium